TIME–FREQUENCY COMPONENT ANALYZER

A DISSERTATION

SUBMITTED TO THE DEPARTMENT OF ELECTRICAL AND ELECTRONICS ENGINEERING

AND THE INSTITUTE OF ENGINEERING AND SCIENCES

OF BILKENT UNIVERSITY

IN PARTIAL FULFILLMENT OF THE REQUIREMENTS

FOR THE DEGREE OF

DOCTOR OF PHILOSOPHY

By

Ahmet Kemal Özdemir

September 2003

I certify that I have read this thesis and that in my opinion it is fully adequate, in scope and in quality, as a thesis for the degree of Doctor of Philosophy.

Assoc. Prof. Dr. Orhan Arıkan (Supervisor)

I certify that I have read this thesis and that in my opinion it is fully adequate, in scope and in quality, as a thesis for the degree of Doctor of Philosophy.

Prof. Dr. Erol Sezer

I certify that I have read this thesis and that in my opinion it is fully adequate, in scope and in quality, as a thesis for the degree of Doctor of Philosophy.

Prof. Dr. Enis Çetin

I certify that I have read this thesis and that in my opinion it is fully adequate, in scope and in quality, as a thesis for the degree of Doctor of Philosophy.

Assoc. Prof. Dr. Mustafa Pınar

I certify that I have read this thesis and that in my opinion it is fully adequate, in scope and in quality, as a thesis for the degree of Doctor of Philosophy.

Prof. Dr. A. Salim Kayhan

Approved for the Institute of Engineering and Sciences:

Prof. Dr. Mehmet Baray
Director of Institute of Engineering and Sciences

ABSTRACT

TIME–FREQUENCY COMPONENT ANALYZER

Ahmet Kemal Özdemir
Ph.D. in Department of Electrical and Electronics Engineering
Supervisor: Assoc. Prof. Dr. Orhan Arıkan
September 2003

In this thesis, a new algorithm, *time–frequency component analyzer* (TFCA), is proposed to analyze composite signals, whose components have compact time–frequency supports. Examples of this type of signals include biological, acoustic, seismic, speech, radar and sonar signals. By conducting its time–frequency analysis in an adaptively chosen warped fractional domain the method provides time–frequency distributions which are as sharp as the Wigner distribution, while suppressing the undesirable interference terms present in the Wigner distribution. Being almost fully automated, TFCA does not require any a priori information on the analyzed signal. By making use of recently developed fast Wigner slice computation algorithm, directionally smoothed Wigner distribution algorithm and fractional domain incision algorithm in the warped fractional domain, the method provides an overall time-frequency representation of the composite signals. It also provides time–frequency representations corresponding to the individual signal components constituting the composite signal. Since, TFCA based analysis enables the extraction of the identified components from the composite signals, it allows detailed post processing of the extracted signal components and their corresponding time–frequency distributions, as well.

Keywords: time–frequency distributions, time–frequency analysis, component analysis, fractional domain warping, fractional Fourier transformation, Wigner distribution, ambiguity function.

ÖZET

ZAMAN–FREKANS BİLEŞEN ÇÖZÜMLEYİCİSİ

Ahmet Kemal Özdemir
Elektrik ve Elektronik Mühendisliği Doktora
Tez Yöneticisi: Doç. Dr. Orhan Arıkan
Eylül 2002

Bu tezde, bileşenleri zaman–frekans düzleminde sık bir dayanağa sahip olan çok bileşenli sinyalleri analiz etmek amacıyla *zaman–frekans bileşen çözümleyicisi* (ZFBÇ) adı verilen yeni bir algoritma öneriliyor. Bu tip sinyallere örnek olarak biyolojik, akustik, sismik, ses, radar ve sonar sinyalleri gösterilebilir. Önerilen yöntem zaman–frekans analizini, incelenen sinyale uyumlu bir biçimde seçilen büzülmüş kesirli Fourier alanında gerçekleştirerek, Wigner dağılımı kadar keskin bir dağılım sunarken, Wigner dağılımında var olan ancak istenmeyen çapraz terim gürültüsünü de oldukça bastırır. Neredeyse tamamen otomatik bir şekilde çalışan yeni yöntem, analiz edilen sinyal ile ilgili her hangi bir ön bilgiye ihtiyaç duymaz. Yakın zamanda geliştirilen, hızlı Wigner dilimi hesaplama algoritması, yönsel Wigner dağılımı yumuşatma algoritması ve kesirli bölge kesme algoritmasını büzülmüş kesirli Fourier alanında kullanan ZFBÇ, incelenen çok bileşenli işaretin oldukça iyi bir zaman–frekans dağılımını verir. ZFBÇ aynı zamanda çok bileşenli işaretin her bir bileşenine ait zaman–frekans dağılımını da ayrı ayrı hesaplar. ZFBÇ'ye dayalı analiz, incelenen çok bileşenli işarete ait bileşenleri ayrı ayrı özütlediği için, kestirilen bileşenler veya bunlara ait zaman–frekans dağılımları üzerinde arzu edilen art işlemlerin gerçekleştirilmesine de olanak sağlar.

Anahtar Kelimeler: zaman–frekans dağılımları, zaman–frekans analizi, bileşen analizi, kesirli bölge büzme işlemi, kesirli Fourier dönüşümü, Wigner dağılımı, belirsizlik işlevi.

ACKNOWLEDGMENTS

I would like to thank Assoc. Prof. Dr. Orhan Arıkan for his supervision, special guidance, suggestions, and encouragement through the development of this thesis.

Special thanks to Prof. Dr. Erol Sezer, Prof. Dr. Enis Çetin, Assoc. Prof. Dr. Mustafa Pınar, and Prof. Dr. Salim Kayhan for reading and commenting on the thesis.

I wish to thank Curtis Condon, Ken White, and Al Feng of the Beckman Institute of the University of Illinois for the bat data and for permission to use it in this thesis.

It is a pleasure to express my special thanks to my family for their constant support, patience and sincere love.

Finally, I would like to express my thanks to all of my friends.

Contents

List of Figures

List of Abbreviations

TFCA	time–frequency component analyzer
ERP	event-related potentials
TFD	time–frequency distribution
WD	Wigner distribution
t–f	time–frequency
AF	Ambiguity function
FT	Fourier transform
ORGK	optimal radially Gaussian kernel
FM	frequency modulated
FrFT	fractional Fourier transformation
FAC	fast ambiguity–slice computation
FWC	fast Wigner–slice computation
FDI	fractional domain incision
RWT	Radon–Wigner transform
FFT	fast Fourier transform
RAFT	Radon–ambiguity function transform
STFT	short–time Fourier transform
PWD	pseudo Wigner distribution
SPWD	smoothed pseudo Wigner distribution
EEG	electroencephalogram
ERP	event related potential

Chapter 1

Introduction

Time–frequency distributions (TFDs) are two dimensional functions which designate the energy content of signals in the time–frequency (t–f) plane [6], [7]. Composite signals whose components have compact time-frequency supports form an important application area for time-frequency signal analysis. Examples cover a wide range of applications including biological [8], [9], acoustic [10], [11], seismic [12], [13], speech [14], [15], radar [16–18] and sonar [16], [19] signals. Much of the research in time–frequency signal processing has been devoted to design of new TFDs. The performance of a TFD is regarded as good if it can offer an *accurate* description of the signal's energy content in the time–frequency plane with *negligible spurious* terms.

Among the distributions developed so far the Wigner distribution (WD) has attracted much of the attention because of its nice theoretical properties [2], [6], [20], [21]. The WD $W_x(t,f)$ of a signal $x(t)$ is defined by the following integral[1]

$$W_x(t,f) \triangleq \int x(t+t'/2)x^*(t-t'/2)e^{-j2\pi ft'}\,\mathrm{d}t' \quad . \tag{1.1}$$

WD is regarded as a time–frequency distribution since it possesses many important and desirable mathematical properties expected from a distribution. Notably, it is always real and integration of the WD across the time axis gives the signal's spectrum and integration of the WD across the frequency axis gives the signal's instantaneous energy [6],[7]. For a component with convex time–frequency support, the WD gives very high *auto–term* concentration. It is

[1] All integrals are from $-\infty$ to $+\infty$ unless otherwise stated.

even argued that more concentration than in the Wigner distribution would be undesirable for this type of signals [22].

Although, WD possesses mathematically pleasing properties, its bilinear form gives rise to spurious structures in the time–frequency plane which are called as *cross–term interference* [6], [7]. Cross–terms appear as a result of both the interaction among different signal components in a multi–component signal and interaction of signal components by themselves. These cross–terms usually interfere with the auto–components and decrease the interpretability of the Wigner distribution.

The geometry of the cross–terms in the Wigner distribution has been extensively analyzed [23]. Even for mono–component signals, there will be cross–term interference if the signal has a non–convex time–frequency support. Thus cross–terms of the WD are classified under two categories. The cross–terms which appear due to the interaction of different signal components (i.e., auto–components) in a multi–component signal are called as *outer* interference (cross) terms and the cross–terms which appear due to the interaction of a single signal component with itself as *inner* interference (cross) terms [23].

The analysis on cross–terms has revealed that, the cross terms might have a peak value as high as twice that of the auto–components, they lie at mid–time and mid–frequency of the auto–components, they are highly oscillatory and the frequency of oscillations increases with the increasing distance in time and frequency [23]. Based on these observations it has been suggested that some sort of smoothing of the Wigner distribution is necessary to suppress the cross–term interference. In a unified framework, the distributions obtained by smoothing the WD are studied under the name of Cohen's bilinear class of time–frequency distributions [6]. In this class, the time–frequency distributions of a signal $x(t)$ are given by

$$TF_x(t,f) \;=\; \iint \kappa(\nu,\tau) A_x(\nu,\tau) e^{-\jmath 2\pi(\nu t+\tau f)}\,\mathrm{d}\nu\,\mathrm{d}\tau \quad , \tag{1.2}$$

where $\kappa(\nu,\tau)$ is called as the kernel of the transformation [6], [24] and $A_x(\nu,\tau)$ is the (symmetric) ambiguity function (AF) which is defined as the 2–D inverse Fourier transform (FT) of the WD:

$$A_x(\nu,\tau) \;\triangleq\; \iint W_x(t,f) e^{\jmath 2\pi(\nu t+\tau f)}\,\mathrm{d}t\,\mathrm{d}f \tag{1.3a}$$

$$\;=\; \int x(t+\tau/2) x^*(t-\tau/2) e^{\jmath 2\pi\nu t}\,\mathrm{d}t \quad . \tag{1.3b}$$

Besides time–frequency analysis, AF has found important application areas in radar and sonar signal processing as well [25–27]. Traditionally, the low-pass smoothing kernel $\kappa(\nu,\tau)$ is designed with the objective of passing the auto–terms which are centered at the origin of the AF plane and suppressing the cross–terms which are located away from the origin. The properties of the resultant time–frequency distribution are closely related to the properties of the chosen kernel [6]. This type of time–frequency distributions with *fixed kernels* such as Page [28], Mergenau and Hill [29], Rihaczek [30], Choi and Williams [31], Papandreou and Boudreaux–Bartels [32] can perform well only for a limited class of signals whose auto–terms in the AF plane are located inside the pass–band region of the kernel $\kappa(\nu,\tau)$. For other signals they offer a trade–off between good cross–term suppression and high auto–term concentration.

To overcome the shortcomings of the TFDs with fixed–kernels, it has been proposed that kernel $\kappa(\nu,\tau)$ should be chosen as signal dependent [33–38]. For instance in well known Optimal Radially Gaussian Kernel (ORGK) [35] design, $\kappa(\nu,\tau)$ is chosen from the family of kernels with Gaussian radial slices

$$\kappa^p(r,\theta) = \exp\left(-\frac{r^2}{2\sigma^2(\theta)}\right) \quad , \tag{1.4}$$

where $r = \sqrt{\tau^2+\nu^2}$, $\theta = \mathrm{atan2}(\tau,\nu)$ and $\kappa^p(r,\theta) \equiv \kappa(r\cos\theta, r\sin\theta)$ is the polar representation of the kernel. In [35], the spread $\sigma^2(\theta)$ is computed by solving the optimization problem

$$\max_{\kappa} \int_0^{2\pi}\int_0^{\infty} |A_x^p(r,\theta)\ \kappa^p(r,\theta)|^2\ r\,\mathrm{d}r\,\mathrm{d}\theta \quad , \tag{1.5}$$

subject to

$$\frac{1}{4\pi^2}\int_0^{2\pi}\int_0^{\infty} |\kappa^p(r,\theta)|^2\ r\,\mathrm{d}r\,\mathrm{d}\theta = \frac{1}{4\pi^2}\int_0^{2\pi} \sigma^2(\theta)\,\mathrm{d}\theta \le \alpha \quad , \quad \alpha \ge 0 \quad . \tag{1.6}$$

Here, $A_x^p(r,\theta) \equiv A_x(r\cos\theta, r\sin\theta)$ is the polar representation of the AF. As discussed in [35], by (1.5) ORGK tries to adjust the pass–band of the low–pass kernel to cover the auto–terms, while by (1.6) it limits the volume of the kernel to α to keep cross–terms, which are located away from the origin, out of the pass-band region of the kernel.

By adapting the pass–band of the kernel based on the location of the auto–terms in the AF domain, signal–dependent TFDs usually offer better cross–term suppression and higher resolution than the TFDs with fixed kernels. However, as discussed in [39], design of a single kernel for the entire signal may lead to some compromises when analyzing multi–component

signals. The adaptation of the kernel at each time to achieve optimal local performance usually provides better TFDs at the expense of significantly increased computational complexity [39]. Nevertheless, the design of a single kernel at each time instant may lead to similar compromises as in ORGK when there are signal components that overlap in time.

There exists another class of time–frequency distributions, which is based on the expansion of a signal on a redundant set of waveforms (also called as atoms) chosen from a dictionary. In the work of Mallat and Zhang the dictionary consists of translated and scaled Gaussian atoms which have compact time–frequency support [40]. After linear expansion of the signal onto atoms in the dictionary, the TFD of the original signal is computed as the weighted sum of the WDs of the atoms used in the signal expansion. Extension of this approach to chirplets is given in [41] and to windowed exponential frequency modulated (FM) functions is given in [42]. Although, these techniques offer a cross–term free distribution, their performance is satisfactory only when the components of the analyzed signal resemble the atoms constituting the dictionary. Otherwise, as illustrated in [43], a blotchy representation is obtained. On the other hand if too many atoms are used in the expansion so that a large class of signals resemble to the atoms in the dictionary, the computational burden of the suboptimal matching pursuits algorithm utilized by these techniques become overwhelming.

On the other hand, some of the researchers investigated different paths to enhance the sharpness and resolution of Cohen's bilinear class of TFDs by using image processing techniques. For instance, in their original work Kodera *et. al.* suggested displacement of the value of the spectrogram at the point (t, f) to a different point (t', f') in the time–frequency plane [44], [45]. Much later, this idea is coined as reassignment method and extended to other bilinear TFDs [46]. When implemented as in [44–46] moving the value of a distribution to a new location away from where its computed increases the readability. On the other hand this may lead to an over localized t–f distribution which may not be desired in all applications. For instance, the reassigned t–f distribution of a sinusoidal signal at frequency f_s approaches to an impulse in the t–f plane around the frequency f_s [46]. Therefore, the reassigned distribution tends to get away from a valid distribution and violates the uncertainty principle. Hence, unlike the WD, the frequency marginal of the reassigned distribution does not give the energy of spectrum of the time–limited sinusoid. Although this suits to applications where identification of the instantaneous frequency law is prime importance, some caution is required

in applications where the *accurate* description of the signal's energy content in t–f plane is desired. Another drawback of this method is that relocation of energy at different t–f points to the same location amplifies the amplitudes of stronger components in the t–f plane much more than the weaker components. Hence reassignment method decreases the relative strength of the weaker components.

In this thesis, we present a new algorithm, to analyze and extract the components of a composite signal whose components have compact time-frequency supports [8–19]. The developed algorithm is called as the Time–Frequency Component Analyzer: TFCA [5], [47–52]. When the signal component has a convex time–frequency support, TFCA just provides its corresponding Wigner distribution. Otherwise, by using a fractional domain[2] warping technique, it provides a high resolution distribution with negligible inner and outer interference terms. Although TFCA produces a signal dependent TFD as in [33–39], it doesn't lead to a compromise between accurate representation of distinct signal components, since TFCA doesn't design a global kernel for the entire signal. In one aspect, TFCA is similar to the techniques which aim to analyze the signal into its components and then compute the TFDs of the individual components as in [40–42]. However, in TFCA signal components are estimated by analyzing the time–frequency distribution of the signal, therefore the disadvantages associated with using a pre–determined and limited set of admissible components are avoided. As it will be illustrated on simulation examples, the TFCA can provide high resolution analysis of signal components which may have non–convex and non–parametric time–frequency supports. By conducting its analysis based on a novel warped fractional Fourier transformation, the obtained high resolution time–frequency distribution does not belong to Cohen's class. Furthermore, as a distinctive feature, TFCA extracts the individual signal components from the analyzed composite signal as well.

In the development of TFCA, very important theoretical results are obtained which are partially presented in [47–52]. In the remaining chapters of this thesis both the theoretical and the practical issues concerning the TFCA are presented in a gradually increasing order of complexity. Following a short chapter about the preliminaries on time–frequency analysis, the main results are presented in four chapters. In the following, a more detailed description of these chapters are given.

[2]Fractional domain is also called fractional Fourier transform domain [53].

In Chapter 3, we present novel theoretical results regarding the slices of the ambiguity function and the Wigner distribution. Although there exist fast algorithms in the literature for digital computation of the AF and the WD samples on Cartesian grids [1], [2], [54], these algorithms lose their efficiency when only a few slices of the AF and the WD are required. Since the fast computation of the arbitrarily located slices of these functions is of prime importance for the efficiency of TFCA, a considerable amount of time is invested in this chapter to develop novel theoretical results concerning the AF and WD slices. First, closed form expressions are derived for the Radon transformations of the cross–Wigner distribution and the cross–ambiguity function by using the fractional Fourier transformation (FrFT). Based on these novel formulations for the projections of the Wigner distribution and the ambiguity function and by using the well known 2–D Fourier transformation relationship between the ambiguity and Wigner domains, closed form expressions are obtained for the slices of the ambiguity function and the Wigner distribution on arbitrary line segments in the time-frequency and lag–Doppler plane respectively. By discretizing the obtained analytical expressions, the fast ambiguity–slice computation (FAC) and the fast Wigner–slice computation (FWC) algorithms are developed for computation of uniformly spaced samples of the ambiguity function and the Wigner distribution located on arbitrary line segments. The complexity of these algorithms is only $O(N \log N)$ flops[3] for a signal with N samples duration. With repeated use of these algorithms, it is possible to obtain samples of the WD and AF on non–Cartesian grids such as rotated Cartesian grids or polar grids which are the natural sampling grids for chirp–like signals.

In Chapter 4, we extend the fast algorithms developed in Chapter 3 to obtain a simplified version of the TFCA which is tailored for chirp–like signals buried in severe outer cross–term interference. To obtain a very high resolution time–frequency description for this type of signals, we develop a novel and efficient algorithm for directionally filtering the slices of the Wigner distribution based on the efficiency of the FWC algorithm presented in Chapter 3 [51]. The main advantage of the new algorithm is its ability to suppress outer interference terms on chirp–like auto–components with convex time–frequency supports without any detrimental effect to the auto–components. For a signal with N samples, the computational complexity of the algorithm is $O(N \log N)$ flops for each filtered slice of the Wigner distribution.

[3]Complex multiplication and addition.

The simplified version of the TFCA algorithm presented in Chapter 4, provides very good results for signals with convex time–frequency supports. However, the inner interference terms of components with non–convex time–frequency supports could only be partially suppressed. In Chapter 5, we alleviate this problem by presenting a more advanced form of the TFCA algorithm which includes a novel fractional domain warping technique as one of its main ingredients. With the incorporation of the warping technique, the high performance of the TFCA on chirp–like components with convex time–frequency supports is extended to mono–component signals with non–convex time–frequency supports. This more advanced form of the TFCA algorithm provides very good time–frequency descriptions by suppressing not only the outer interference terms but also the inner interference terms in the Wigner distribution. When digitally implemented, the complexity of the algorithm is only $O(N \log N)$ flops for each computed slice of the distribution for a signal with N samples duration.

In the Chapter 6, the final form of the TFCA is given as an iterative signal adaptive time–frequency distribution, which can handle both mono and multi–component signals with convex or non–convex supports in time frequency plane. This form of the TFCA is almost fully automated. First of all, by utilizing an image segmentation algorithm [3], the warping parameters are automatically computed without user interaction. Secondly, by making use of an efficient time–frequency domain incision technique components of the composite signal are extracted. Although, various approaches based on time–frequency processing techniques have been investigated in the literature [55–61], in this thesis, results based on the fractional domain incision (FDI) algorithm [52], [56] are presented. Since the FDI algorithm operates on the time–domain signal, it provides reliable estimates for each component of a composite signal in $O(N \log N)$ flops, when the composite signal has a duration of N samples. Then, the time–frequency representation of the extracted signal component is computed by using the techniques presented in Chapters 3-5. After the estimate of the component is subtracted from the composite signal the same analysis is conducted on the residual signal. At the end, the time–frequency representations of individual auto–terms are summed to obtain the TFCA of the composite signal. Based on a set of synthetic and real data simulations, it is shown that the proposed iterative algorithm provides highly accurate representation of multi–component signals.

Finally, remarks and conclusions are provided in Chapter 7.

Chapter 2

Preliminaries on Time–frequency Analysis

2.1 Wigner Distribution and the Ambiguity Function

Discrete time–frequency analysis is the primary investigation tool in the synthesis, characterization and filtering of time–varying signals. Among the alternative time–frequency analysis algorithms, those belonging to the Cohen's class are the most commonly utilized ones. In this class, the time–frequency distributions of a signal $x(t)$ are given by[1]:

$$TF_x(t,f) \;=\; \iiint \kappa(\nu,\tau)x(u+\tau/2)x^*(u-\tau/2)e^{\jmath 2\pi(\nu u-\nu t-\tau f)}\,\mathrm{d}u\,\mathrm{d}\nu\,\mathrm{d}\tau \;\;, \tag{2.1}$$

where the function $\kappa(\nu,\tau)$ is called the kernel [6],[24]. Recent research on the time–frequency signal analysis has revealed that signal dependent choice of the kernel helps in localization of the time–frequency components of the signals [33–39], [62]. By choosing $\kappa(\nu,\tau) = 1$, the most commonly used member of the Cohen's class, the Wigner distribution, is obtained:

$$W_x(t,f) \triangleq \int x(t+t'/2)x^*(t-t'/2)e^{-\jmath 2\pi f t'}\,\mathrm{d}t' \;\;. \tag{2.2}$$

Because of its nice energy localization properties, the WD has found important application areas. The definition (2.2) has been generalized to define the cross–Wigner distribution of two

[1] All integrals are from $-\infty$ to $+\infty$ unless otherwise stated.

signals $x(t)$ and $y(t)$ as:

$$W_{xy}(t,f) \triangleq \int x(t+t'/2)y^*(t-t'/2)e^{-\jmath 2\pi f t'}\,\mathrm{d}t' \ . \tag{2.3}$$

The properties of the cross–Wigner distribution has been investigated in detail [2], [63]. Note that, $W_{xx}(t,f) \equiv W_x(t,f)$ holds.

The 2–D inverse Fourier transform of the WD is called the (symmetric) ambiguity function which has found important application areas in time–frequency and radar signal processing:

$$A_x(\nu,\tau) \triangleq \iint W_x(t,f)e^{\jmath 2\pi(\nu t+\tau f)}\,\mathrm{d}t\,\mathrm{d}f \tag{2.4a}$$

$$= \int x(t+\tau/2)x^*(t-\tau/2)e^{\jmath 2\pi\nu t}\,\mathrm{d}t \ . \tag{2.4b}$$

Similar to the cross–Wigner distribution, the cross–ambiguity function of two signals $x(t)$ and $y(t)$ is defined as

$$A_{xy}(\nu,\tau) \triangleq \int x(t+\tau/2)y^*(t-\tau/2)e^{\jmath 2\pi\nu t}\,\mathrm{d}t \ . \tag{2.5}$$

As in (2.4a), the cross–ambiguity function is related to the cross–Wigner distribution through the 2–D inverse Fourier transformation:

$$A_{xy}(\nu,\tau) = \iint W_{xy}(t,f)e^{\jmath 2\pi(\nu t+\tau f)}\,\mathrm{d}t\,\mathrm{d}f \ . \tag{2.6}$$

2.2 The Fractional Fourier Transformation

The a^{th} order, $a \in \Re$, $0 < |a| < 2$, fractional Fourier transform of a function $x(t)$ is defined as [64]:

$$x_a(t) \equiv \{\mathcal{F}^a\, x\}(t) \triangleq \int K_a(t,t')x(t')\,\mathrm{d}t' \ , \tag{2.7}$$

where the kernel of the transformation $K_a(t,t')$ is

$$K_a(t,t') = A_\phi \exp\left[j\pi(t^2\cot\phi - 2tt'\csc\phi + t'^2\cot\phi)\right] \ , \tag{2.8}$$

$$A_\phi = \frac{\exp(-j\pi\,\mathrm{sgn}(\sin\phi)/4 + j\phi/2)}{|\sin\phi|^{1/2}} \ , \tag{2.9}$$

$$\phi = \frac{a\pi}{2} \ . \tag{2.10}$$

The transformation kernel is the complex exponential $e^{-\jmath 2\pi tt'}$ for $a = 1$, and it approaches to $\delta(t)$ for $a = 0$, and to $\delta(t+t')$ for $a = \pm 2$. Thus, it follows that 1^{st} order FrFT is the

ordinary Fourier transform and 0^{th} order FrFT is the function itself. The definition of the FrFT is easily extended to outside the interval $[-2,\ 2]$, by noting that $\mathcal{F}^{4k}$ is the identity operator for any integer k and FrFT is additive in index, i.e., $\mathcal{F}^{a_1}\mathcal{F}^{a_2} = \mathcal{F}^{a_1+a_2}$. The other interesting and useful properties of the FrFT can be found in [65].

Chapter 3

Fast Computation of the Ambiguity Function and the Wigner Distribution on Arbitrary Line Segments

3.1 Introduction

Time–frequency signal processing is one of the fundamental research areas in signal processing. Wigner distribution plays a central role in the theory and practice of time–frequency signal processing [2],[6],[7],[63],[66–71]. Likewise, the ambiguity function, which is the 2–D Fourier transform of the Wigner distribution, plays a central role in time–frequency signal analysis [62],[72],[73], radar and sonar signal processing [25–27],[74].

The TFCA presented in this thesis requires efficient computation of the WD samples on arbitrary line segments. For a signal of duration N samples, the existing algorithms require $O(N^2 \log N)$ flops for each line segment [1],[2],[54] in Wigner and ambiguity planes. In this chapter, we develop fast computational algorithms for both the WD and the AF. Due to lack of theoretical results in the literature, in the following sections we invest a great amount of time to develop a solid theoretical basis for the proposed algorithms.

In this chapter, first we derive closed form expressions for the Radon transformations of the cross–Wigner distribution and the cross–ambiguity function by using the fractional

Fourier transformation. Although the expression for cross–Wigner projection, which first appeared in [50] and then in [75], is a straightforward extension of a similar property for the auto Wigner distribution [76], the simple closed form expressions presented in [49], [50] for the auto and cross ambiguity function projections are quite novel with deep theoretical and practical implications. Then, based on the well known 2–D Fourier transformation relationship between the ambiguity and Wigner domains, novel closed form expressions are obtained for the slices of both the WD and the AF. By using discretization of the obtained analytical expressions, fast Wigner–slice and the fast ambiguity–slice computation algorithms are proposed to compute uniformly spaced samples of the WD and the AF located on arbitrary line segments. With repeated use of these algorithms, it is possible to obtain samples of the WD and AF on non–Cartesian grids, such as rotated Cartesian grids and the polar grids which are the natural sampling grids of chirp like signals. Apart from its use in this thesis, the ability of obtaining WD and AF samples over rotated Cartesian grids and polar grids is potentially very useful in various important application areas including time–frequency domain kernel design, multi–component signal analysis, time–frequency domain signal detection and particle location analysis in Fresnel holograms [33], [34], [36], [39], [77–79].

The organization of this chapter is in accordance with the dual nature of the ambiguity function and Wigner distribution. In Section 3.2, by using the Radon–Wigner transformation, analytical expressions are derived for the slices of the auto ambiguity functions. Then, by discretizing the obtained analytical expressions, efficient algorithms are presented for the computation of slices of the ambiguity function. In Section 3.3, we follow a similar development leading to novel closed form expressions for the Radon–ambiguity function, and present efficient algorithms for the computation of slices of the Wigner distribution. In Section 3.4, both the analytical and computational results are extended to the *cross* AF and WD. In Section 3.5, we provide results of simulated applications of the proposed algorithms. Finally, the chapter is concluded in Section 3.6.

3.2 Fast Computation of the Ambiguity Function on Arbitrary Line Segments

In this section, an efficient algorithm to compute the ambiguity function on uniformly spaced samples along an arbitrary line segment is provided. For the sake of simplicity, a gradual method of presentation is used where we first consider obtaining uniformly spaced samples of the AF on a line segment centered at the origin. Then, we extend this approach to obtain samples on a line segment positioned radially. Finally, we consider the case of an arbitrary line segment. The presentation of the proposed approach will be as follows: first the well known projection–slice relationship between the WD and the AF domains will be given. Then, the projections in the WD domain will be related to the fractional Fourier transformation of the signals involved. Finally, the obtained continuous–time relationship will be discretized to allow the use of a fast fractional Fourier transformation algorithm.

3.2.1 The Radon–Wigner Transform

The Radon–Wigner transform (RWT) or Radon transformation of the Wigner distribution has been introduced for the analysis and classification of multi–component chirp signals in noise. Several authors investigated RWT and some of its applications in multi–component signal analysis, time–varying filtering and adaptive kernel design [77], [80–83]. The RWT of a function $x(t)$ is defined as the Radon transform of its WD. Using the geometry in Fig. 3.1, RWT can be written as

$$\mathcal{R}DN\ [W_x](r,\phi) = \int W_x(r\cos\phi - s\sin\phi, r\sin\phi + s\cos\phi)\,\mathrm{d}s\ \ , \tag{3.1}$$

where (r,ϕ) are the transform domain variables in polar format. With this definition, the RWT can be viewed as the family of the projections $\{\mathcal{R}DN\ [W_x](r,\phi),\ \ 0 \le \phi < \pi\}$. The projection–slice theorem [84] establishes an important link between the projections of the WD and the slices of the AF: the 1–D inverse Fourier transform of the projection $\mathcal{R}DN\ [W_x](r,\phi)$ with respect to the radial variable r is the radial slice of the ambiguity function at the angle ϕ

$$\int \mathcal{R}DN\ [W_x](r,\phi)e^{j2\pi r\lambda}\,\mathrm{d}r \ = \ A_x(\lambda\cos\phi, \lambda\sin\phi) \tag{3.2a}$$

$$= \ A_x^p(\lambda,\phi)\ \ , \tag{3.2b}$$

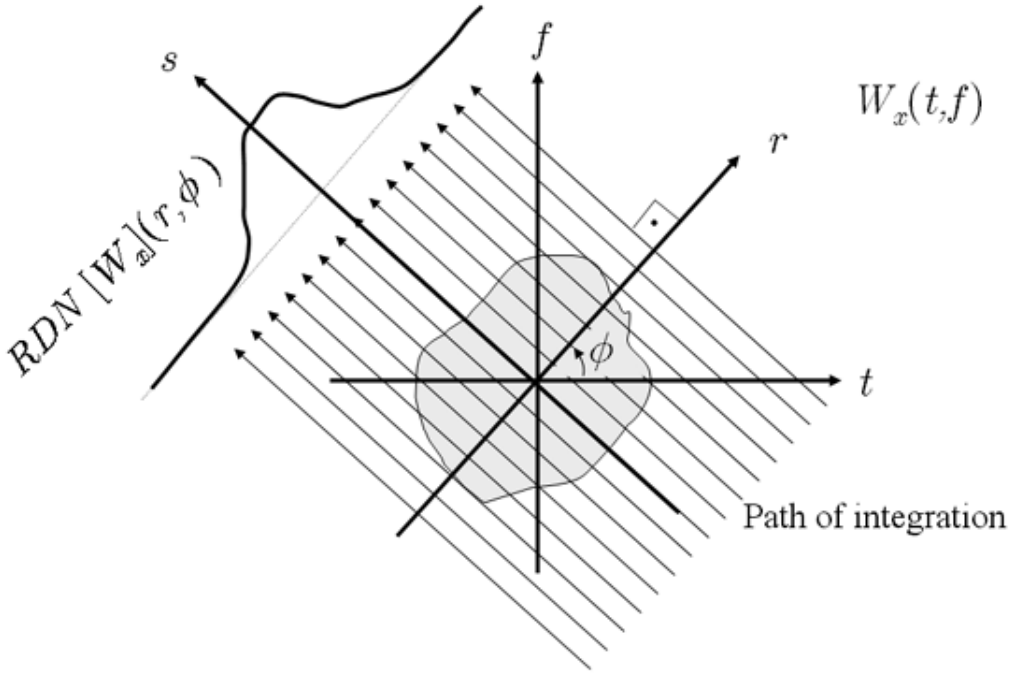

Figure 3.1: Radon transform geometry for the RWT.

where $A_x^p(\lambda,\phi) \triangleq A_x(\lambda\cos\phi, \lambda\sin\phi)$ is the polar representation of the AF. Therefore, once we have the projection $\mathcal{RDN}\,[W_x](r,\phi)$, we can use the fast Fourier transform (FFT) algorithm to efficiently approximate the samples on the radial slice of the AF. However, to have a practically useful algorithm, we have to obtain the RWT efficiently as well. Fortunately, as it has been shown in [76], the radial slices of the RWT, $\mathcal{RDN}\,[W_x](r,\phi)$, can be computed directly from the time signal $x(t)$ by using the fractional Fourier transformation:

$$\mathcal{RDN}\,[W_x](r,\phi) = |\{\mathcal{F}^a\ x\}(r)|^2 \equiv |x_a(r)|^2 \quad , \quad \text{for } a = \frac{2\phi}{\pi} \quad , \tag{3.3}$$

where $\mathcal{RDN}\,[W_x](r,\phi)$ is the ϕ–Radon projection of the WD given by (3.1), and $x_a(r)$ is the a^{th}–order FrFT of the signal as given in Section 2.2. Combining (3.2) and (3.3), we obtain the following relation between the AF and the FrFT of a signal:

$$A_x^p(\lambda,\phi) = \int |x_a(r)|^2 e^{\jmath 2\pi r\lambda}\,\mathrm{d}r \ . \tag{3.4}$$

Thus, the ordinary one–dimensional inverse Fourier transform of the magnitude squared a^{th} order FrFT of a signal is equal to the radial slice of its ambiguity function that makes an angle of $a\pi/2$ with respect to the ν–axis in the $\nu-\tau$ plane.

3.2.2 Efficient Computation Of the Ambiguity Function Samples Along Radial Slices of the Ambiguity Plane

In this section, we provide the details of a fast algorithm for computing radial samples of the ambiguity function. As it will be shown in detail, for an input sequence of length N, it is possible to compute the samples of AF on an arbitrary line segment centered at the origin in $O(N \log N)$ flops. We start with the approximation of the integral in (3.4) with its uniform Riemann summation. For an equally valid approximation at all angles ϕ, in the rest of this chapter, we assume that prior to obtain its samples, $x(t)$ is scaled so that its Wigner domain support is approximately confined into a circle with radius $\Delta_x/2$ centered at the origin. In other words, any a^{th} order FrFT of $x(t)$, including the signal itself and its ordinary Fourier transform, has negligible energy outside the symmetric interval $[-\Delta_x/2,\ \Delta_x/2]$. For a signal $x(t)$ with approximate time and frequency supports of Δ_t and Δ_f respectively, the required scaling is $x(t/s)$ where $s = \sqrt{\Delta_f/\Delta_t}$ [85].

After the scaling, the double–sided bandwidth of $|x_a(r)|^2$ is $2\Delta_x$. Therefore its inverse FT given in (3.4) can be approximated in terms of its uniformly obtained samples at a rate $2\Delta_x$ using the following discrete–time inverse Fourier transform relation[1]:

$$A_x^p(\lambda,\phi) = \frac{1}{2\Delta_x} \sum_{n=-N}^{N-1} |x_a[n]|^2 e^{\jmath \frac{\pi\lambda n}{\Delta_x}} \qquad , \qquad -\Delta_x \le \lambda < \Delta_x \ , \tag{3.5}$$

where N is an arbitrary integer that is greater than Δ_x^2, which is the time–bandwidth product of $x_a(r)$ and $x_a[n] \triangleq x_a(n/2\Delta_x)$ is the n^{th} sample of the FrFT $x_a(r)$. To obtain $2N$ equally–spaced radial samples of $A_x^p(\lambda,\phi)$, we substitute $\lambda = k\Delta_x/N$ in the above equation:

$$A_x^p(\frac{k}{N}\Delta_x,\phi) = \frac{1}{2\Delta_x} \sum_{n=-N}^{N-1} |x_a[n]|^2 e^{\jmath \frac{2\pi kn}{2N}} \qquad , \qquad -N \le k \le N-1 \ . \tag{3.6}$$

After the discretization, the obtained form lends itself for an efficient digital computation since the required samples of the FrFT, $x_a(n/2\Delta_x),\ -N \le n \le N-1$, can be computed using the recently developed fast computation algorithm [85] in $O(N \log N)$ flops. The summation in (3.6) can be recast into a $2N$ point discrete Fourier transformation which can be computed

[1]From this observation we deduce the following fact: If the WD of $x(t)$ is confined into a circle with radius $\Delta_x/2$ in the Wigner plane, then its AF is confined into a circle with radius Δ_x in the ambiguity plane.

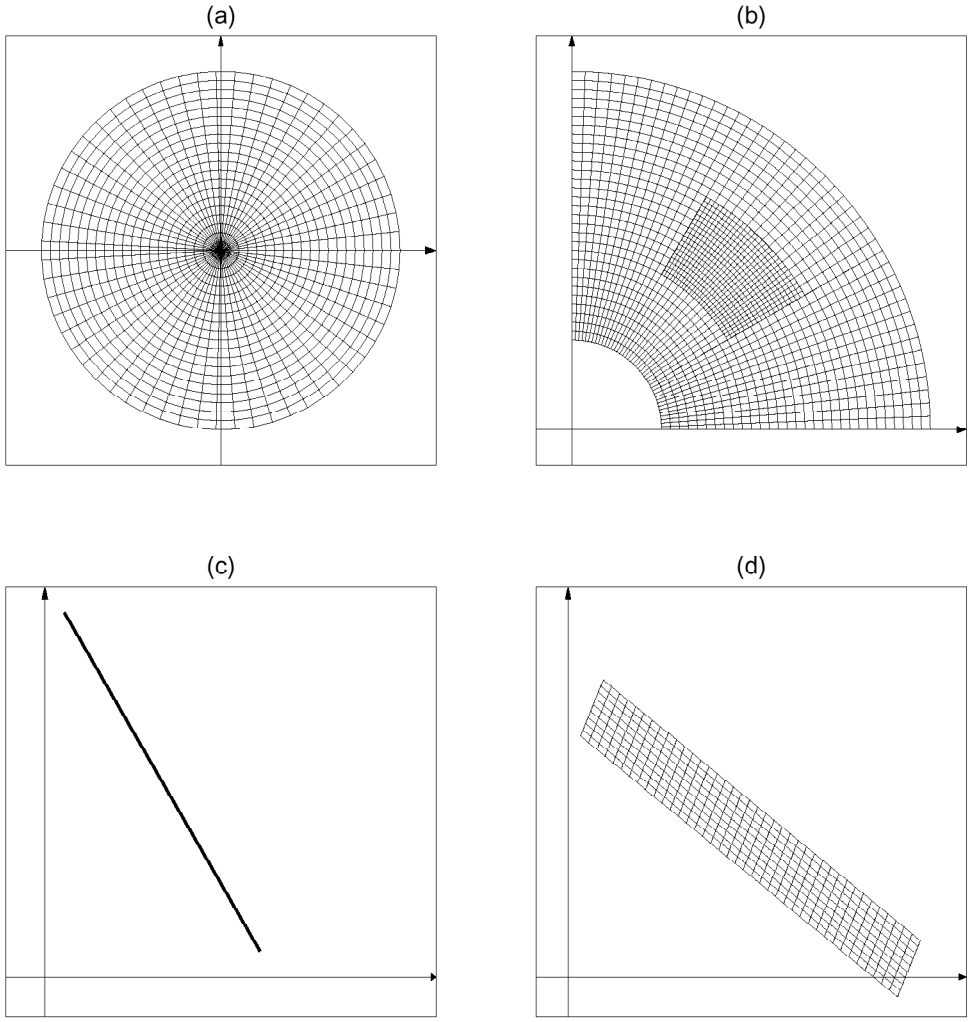

Figure 3.2: Some grids on which the AF and WD of a signal can be computed by using the fast ambiguity–slice and fast Wigner–slice computation algorithms: (a) a full polar grid, (b) a partial polar grid with non–uniform grid density, (c) an arbitrary line segment (d) and a parallelogram.

in $O(N \log N)$ flops by using the fast Fourier transform algorithm. Therefore the overall cost of computing the samples of the AF along any radial slice is $O(N \log N)$ flops.

Note that, the relationship in (3.6) is discrete in the radial variable k and continuous in the angular variable ϕ. By discretizing the angular variable, the samples of the AF along several radial lines can be computed. For instance, if this algorithm is used for a uniformly distributed set of angles $\phi_m = (\pi/M)k$, $0 \leq k \leq M-1$, covering the range $[0,\ \pi)$, then the samples of the AF located on a polar grid can be computed in $O(MN \log N)$ flops. In Fig. 3.2(a) we illustrate the shape of a polar grid on which the samples of the AF $A_x(\nu, \tau)$ can be computed by using this algorithm.

3.2.3 Computation of the Ambiguity Function along the Segments of the Radial Slices

In order to compute the samples of the AF on an arbitrarily positioned segment of a radial slice, the chirp z–transform (CZT) algorithm [86] can be used. Here, we will use a special version of this algorithm (also called chirp transform algorithm) to compute N' uniformly spaced samples of a radial slice $A_x^p(\lambda,\phi)$ on the interval $[\lambda_i,\ \lambda_f]\ \bmod (2\Delta_x)$ for arbitrary values of the parameters N', λ_i and λ_f.

To obtain the required samples, we substitute $\lambda = \lambda_i + k\Delta_\lambda$, $0 \le k \le N'-1$, in (3.5), where the sampling interval of the frequency variable is $\Delta_\lambda = \frac{\lambda_f - \lambda_i}{N'-1}$. After the rearrangement of the summation as

$$A_x^p(\lambda_i + k\Delta_\lambda, \phi) = \frac{1}{2\Delta_x} \sum_{n=-N}^{N-1} \left(|x_a[n]|^2 e^{\jmath\pi \frac{\lambda_i}{\Delta_x} n} \right) e^{\jmath\pi \frac{\Delta_\lambda}{\Delta_x} kn} \tag{3.7a}$$

$$= \sum_{n=-N}^{N-1} g[n] W^{kn} \qquad , \qquad k = 0, 1, \ldots, N'-1 \ , \tag{3.7b}$$

where $g[n]$ and W are defined as

$$g[n] = \frac{1}{2\Delta_x} |x_a[n]|^2 e^{\jmath\pi \frac{\lambda_i}{\Delta_x} n} \tag{3.8}$$

$$W = e^{\jmath\pi \frac{\Delta_\lambda}{\Delta_x}} \ , \tag{3.9}$$

we use the identity $kn = \frac{1}{2}[k^2 + n^2 - (k-n)^2]$ in (3.7b) and obtain an alternative but equivalent expression for $A_x^p(\lambda_i + k\Delta_\lambda, \phi)$:

$$A_x^p(\lambda_i + k\Delta_\lambda, \phi) = W^{k^2/2} \sum_{n=-N}^{N-1} W^{-(k-n)^2/2} (g[n] W^{n^2/2}) \qquad , \qquad k = 0, 1, \ldots, N'-1 \ . \tag{3.10}$$

In this expression, $A_x^p(\lambda_i + k\Delta_\lambda, \phi)$, can be interpreted as the convolution of the chirp–modulated signal $g[k]$ and the chirp $W^{-k^2/2}$, multiplied with another chirp $W^{k^2/2}$. Since the convolution can be computed efficiently by using the FFT algorithm, for the usual case of $N' \le N$, the uniformly spaced samples of the radial slice $A_x^p(\lambda,\phi)$ located in the segment $[\lambda_i,\ \lambda_f]\ \bmod (2\Delta_x)$ can be obtained in $O(N \log N)$ flops. In Fig. 3.2(b), we illustrate the shape of a partial polar grid, on which the samples of the AF $A_x(\nu,\tau)$ can be computed by using the algorithm of the previous section combined with the CZT algorithm. In this plot, the polar

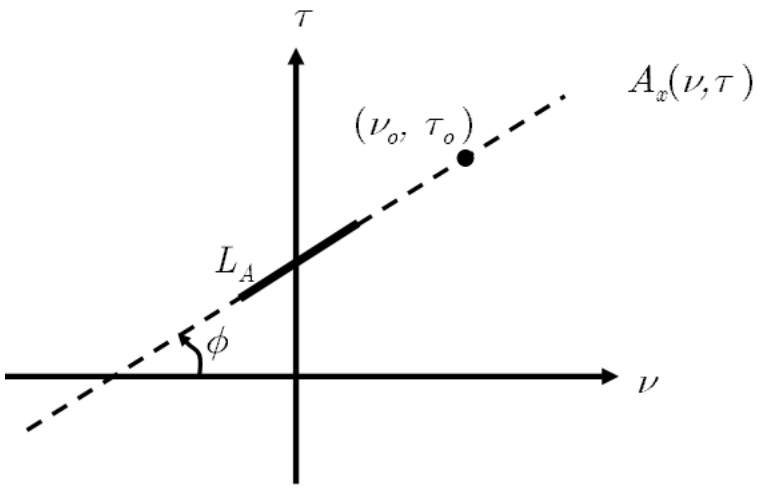

Figure 3.3: A non–radial line segment in the ambiguity function plane which lies on a line that passes through the point (ν_o, τ_o) and makes an angle of ϕ radians with the ν–axis.

grid has denser samples in the middle region. The samples on the radial slices which pass through both the denser and non–denser parts of the grid can be obtained by using the CZT algorithm three times: once to compute the samples in the denser region and twice to compute the samples in the non–denser regions.

3.2.4 Computation of the Ambiguity Function Along Arbitrary Line Segments

In this section we present a fast computational algorithm that computes the samples of AF on a non–radial slice. Let us consider the case of computing the samples of the AF $A_x(\nu, \tau)$ along the line segment L_A shown in Fig. 3.3. The following parameterization for the line segment L_A will be used in the derivations:

$$L_A = \{(\nu, \tau) | \nu = \nu_o + \lambda \cos\phi,\ \tau = \tau_o + \lambda \sin\phi,\ \lambda_i \leq \lambda \leq \lambda_f\} \ , \tag{3.11}$$

where (ν_o, τ_o) is an arbitrary point which lies on L_A and ϕ is the angle between L_A and the ν–axis. Using this parameterization of L_A and the definition of the AF, the non–radial slice of

the AF which lies on the line segment L_A can be written as

$$A_x(\nu_o + \lambda\cos\phi, \tau_o + \lambda\sin\phi) = \int x(t + \frac{\tau_o + \lambda\sin\phi}{2}) x^*(t - \frac{\tau_o + \lambda\sin\phi}{2}) \times e^{\jmath 2\pi(\nu_o + \lambda\cos\phi)t}\,\mathrm{d}t \quad (3.12a)$$

$$\equiv A_{yz}(\lambda\cos\phi, \lambda\sin\phi)\ , \quad (3.12b)$$

where $A_{yz}(\nu, \tau)$ is the cross–ambiguity function of the following time–domain signals $y(t)$ and $z(t)$

$$y(t) = x(t + \tau_o/2)e^{\jmath\pi\nu_o t} \quad (3.13)$$

$$z(t) = x(t - \tau_o/2)e^{-\jmath\pi\nu_o t}\ . \quad (3.14)$$

Thus, the non–radial slice of $A_x(\nu, \tau)$ is equal to the radial slice of the $A_{yz}(\nu, \tau)$ where both of the slices are in parallel. Hence, similar to (3.2), the projection–slice theorem can be used to express the slice of the $A_x(\nu, \tau)$ along the line segment L_A as the 1–D inverse FT of the ϕ–Radon projection of the corresponding cross–Wigner distribution $W_{yz}(t, f)$:

$$A_x(\nu_o + \lambda\cos\phi, \tau_o + \lambda\sin\phi) = \int \mathcal{R}DN\ [W_{yz}](r, \phi)e^{\jmath 2\pi r\lambda}\,\mathrm{d}r\ . \quad (3.15)$$

We note that analogous to (3.3), the ϕ–Radon projections of the cross WD can be obtained from the following FrFT relation [49], [75]:

$$\mathcal{R}DN\ [W_{yz}](r, \phi) = [\{\mathcal{F}^a\ y\}(r)]\,[\{\mathcal{F}^a\ z\}(r)]^* \equiv y_a(r)z_a^*(r)\ , \quad (3.16)$$

where $a = 2\phi/\pi$ is the FrFT order. Then, following the discussions in Section 3.2.2 and 3.2.3, we obtain the following expression for the N' uniformly spaced samples of the AF on the line segment L_A:

$$A_x(\nu_o + \lambda_k\cos\phi, \tau_o + \lambda_k\sin\phi) = \frac{1}{2\Delta_x}\sum_{n=-N}^{N-1} y_a(\frac{n}{2\Delta_x})z_a^*(\frac{n}{2\Delta_x})e^{\jmath\frac{\pi\lambda_k n}{\Delta_x}} \quad , \quad k = 0, 1, \ldots, N'-1\ , \quad (3.17)$$

where $\lambda_k = \lambda_i + \frac{\lambda_f - \lambda_i}{N'-1}k$. As in the last section, these samples of the AF on the non–radial line segment L_A can be computed using the chirp transform algorithm.

3.3 Fast Computation of the Wigner Distribution on Arbitrary Line Segments

In the rest of this chapter, we will present the dual development for the Wigner distribution. In the next section, we introduce the dual of the Radon–Wigner transform: the Radon–ambiguity function transform (RAFT). Then, we derive the relationship between the RAFT and FrFT. As in the computation of the AF samples, this relationship will naturally lead us to the fast computation algorithm for the required WD samples.

3.3.1 Radon–Ambiguity Function Transform

The Radon transformation has been found to be a useful tool in time–frequency signal processing with applications to detection of chirp rates [78] and signal–dependent kernel design [33]. As we show in the following sections, the Radon transform of the ambiguity function itself is also an important tool in the efficient computation of the WD slices.

Here, we introduce the Radon–ambiguity function transform of a signal $y(t)$ as the Radon transform of its ambiguity function. The RAFT can be written as

$$\mathcal{R}DN\ [A_y](r,\phi) = \int A_y(r\cos\phi - s\sin\phi, r\sin\phi + s\cos\phi)\,\mathrm{d}s\ \ , \tag{3.18}$$

where (r,ϕ) are the polar format variables. Using the projection–slice theorem, the radial slice of the WD at an angle ϕ can be written as the FT of $\mathcal{R}DN\ [A_y](r,\phi)$ with respect to the radial variable r

$$\int \mathcal{R}DN\ [A_y](r,\phi)e^{-\jmath 2\pi r\lambda}\,\mathrm{d}r \ = \ W_y(\lambda\cos\phi, \lambda\sin\phi) \tag{3.19a}$$

$$= \ W_y^p(\lambda,\phi)\ \ , \tag{3.19b}$$

where $W_y^p(\lambda,\phi) \triangleq W_y(\lambda\cos\phi, \lambda\sin\phi)$ is the polar representation of the WD.

To obtain a fast computational algorithm similar to that in Section 3.2.2, the samples of the projections $\mathcal{R}DN\ [A_y](r,\phi)$ have to be obtained efficiently. One of the important results obtained in this thesis is the following simple relation between the RAFT and the FRFT

$$\mathcal{R}DN\ [A_y](r,\phi) = y_{(a-1)}(r/2)y^*_{(a-1)}(-r/2)\ \ , \tag{3.20}$$

which is proved in Appendix A. Thus combining (3.19) with (3.20) and discretizing the obtained relationship, we obtain an algorithm which can be used to compute the samples of the WD on polar grids, such as the ones shown in Fig. 3.2(a) and Fig. 3.2(b). In the following section, based on the above relationship we propose an efficient algorithm to compute samples of the WD on arbitrary line segments.

3.3.2 Computation of the Wigner Distribution Along Arbitrary Line Segments

Suppose that we want to compute samples of the WD of a waveform $x(t)$, along an arbitrary line segment L_W in the Wigner plane. Since the line segment L_W may not pass through the origin, we cannot immediately use the results of the previous section. However, as in Section 3.2.4, we will express the required non–radial slice as the radial slice of the WD of another function which allows us to use the results of the previous section. In the following derivation we parameterize the line segment L_W as:

$$L_W = \{(t,f) | t = t_o + \lambda\cos\phi,\ f = f_o + \lambda\sin\phi,\ \lambda_i \leq \lambda \leq \lambda_f\}\ . \tag{3.21}$$

In this expression, (t_o, f_o) is an arbitrary point which lies on L_W and ϕ is the angle of L_W with the t–axis. Using this parameterization of L_W, the non–radial slice of the WD can be expressed as

$$\begin{aligned} W_x(t_o + \lambda\cos\phi, f_o + \lambda\sin\phi) &= \int x(t_o + \lambda\cos\phi + t'/2)x^*(t_o + \lambda\cos\phi - t'/2) \\ &\quad \times\ e^{-\jmath 2\pi(f_o + \lambda\sin\phi)t'}\,\mathrm{d}t' \qquad (3.22a) \\ &\equiv\ W_y(\lambda\cos\phi, \lambda\sin\phi)\ , \qquad (3.22b) \end{aligned}$$

where $W_y(\lambda\cos\phi, \lambda\sin\phi)$ is the radial slice of the WD of $y(t)$:

$$y(t) = x(t + t_o)e^{-\jmath 2\pi f_o t}\ . \tag{3.23}$$

Hence, the non–radial slice of the WD of $x(t)$ is the same as the radial slice of the WD of the time–shifted and frequency–modulated version of it, where both slices are in parallel. By using the projection–slice theorem given in (3.19), the non–radial slice of the WD of $x(t)$ can be obtained as

$$W_x(t_o + \lambda\cos\phi, f_o + \lambda\sin\phi) = \int \mathcal{R}DN\ [A_y](r,\phi)e^{-\jmath 2\pi r\lambda}\,\mathrm{d}r\ , \tag{3.24}$$

where $\mathcal{R}DN\ [A_y](r,\phi)$ is the ϕ–Radon projection of the ambiguity function $A_y(\nu,\tau)$. Since the required ϕ–Radon projection satisfies the following FrFT relationship:

$$\mathcal{R}DN\ [A_y](r,\phi) = y_{(a-1)}(r/2)y^*_{(a-1)}(-r/2)\ , \tag{3.25}$$

where $a = 2\phi/\pi$, it can be efficiently computed by using the fast FrFT algorithm proposed in [85] and given here as Algorithm 2. The steps of the proposed $O(N\log N)$ algorithm is given in Algorithm 4. Note that, unlike $\mathcal{R}DN\ [W_x](r,\phi)$, which is the ϕ–Radon projection of the WD given by (3.1), the double–sided bandwidth of $\mathcal{R}DN\ [A_y](r,\phi)$ is Δ_x.

3.4 Fast Computation of the Cross Ambiguity Function and the Cross Wigner Distribution on Arbitrary Line Segments

Up to now, our main objective was developing algorithms for efficient computation of the samples of the AF and WD on arbitrary line segments. However, in some applications [25], [60] it is required to compute the cross AF and the cross WD of a pair of given signals. As we show below, the same algorithms, with some slight modifications, can still be used to compute samples of the cross AF and the cross WD on arbitrary line segments efficiently.

3.4.1 Fast Ambiguity–slice Computation Algorithm: Fast Computation of the Cross Ambiguity Function on Arbitrary Line Segments

Suppose that we want to compute the samples of the cross AF of the two signals $y(t)$ and $z(t)$ on the line segment L_A shown in Fig. 3.3. This non–radial slice of the cross AF function is given as

$$\begin{aligned} A_{yz}(\nu_o+\lambda\cos\phi,\tau_o+\lambda\sin\phi) &= \int y(t+\frac{\tau_o+\lambda\sin\phi}{2})z^*(t-\frac{\tau_o+\lambda\sin\phi}{2}) \\ &\quad\times\ e^{\jmath 2\pi(\nu_o+\lambda\cos\phi)t}\,\mathrm{d}t \qquad (3.26a) \\ &\equiv A_{\tilde{y}\tilde{z}}(\lambda\cos\phi,\lambda\sin\phi)\ , \qquad (3.26b) \end{aligned}$$

where $A_{\tilde{y}\tilde{z}}(\lambda\cos\phi, \lambda\sin\phi)$ is the radial slice of the cross AF of the signals $\tilde{y}(t)$ and $\tilde{z}(t)$:

$$\tilde{y}(t) = y(t+\tau_o/2)e^{\jmath\pi\nu_o t} \tag{3.27}$$

$$\tilde{z}(t) = z(t-\tau_o/2)e^{-\jmath\pi\nu_o t} \ . \tag{3.28}$$

The radial–slice of the $A_{\tilde{y}\tilde{z}}(\nu,\tau)$ is the 1–D inverse FT of the ϕ–Radon projection of the $W_{\tilde{y}\tilde{z}}(t,f)$

$$A_{\tilde{y}\tilde{z}}(\lambda\cos\phi, \lambda\sin\phi) = \int \mathcal{R}DN\ [W_{\tilde{y}\tilde{z}}](r,\phi)e^{\jmath 2\pi\lambda r}\,\mathrm{d}r \ , \tag{3.29}$$

where the ϕ–Radon projection satisfies the following relation with the FrFTs of $\tilde{y}(t)$ and $\tilde{z}(t)$:

$$\mathcal{R}DN\ [W_{\tilde{y}\tilde{z}}](r,\phi) = \tilde{y}_a(r)\tilde{z}_a^*(r) \quad , \quad a = \frac{2}{\pi}\phi \ . \tag{3.30}$$

Then, the required non–radial slice of the $A_{yz}(\nu,\tau)$ can be obtained as

$$A_{yz}(\nu_o+\lambda\cos\phi, \tau_o+\lambda\sin\phi) = \int \tilde{y}_a(r)\tilde{z}_a^*(r)e^{\jmath 2\pi\lambda r}\,\mathrm{d}r \ . \tag{3.31}$$

Discretization of this expression yields the fast computational algorithm which is tabulated in Algorithm 3.

3.4.2 Fast Wigner–slice Computation Algorithm: Fast Computation of the Cross Wigner Distribution on Arbitrary Line Segments

In this section, we derive the algorithm for fast computation of the samples of the $W_{yz}(t,f)$ on an arbitrary line segment L_W as parameterized in (3.21). This non–radial slice of the cross WD can be expressed as the radial slice of $W_{\tilde{y}\tilde{z}}(t,f)$:

$$W_{yz}(t_o+\lambda\cos\phi, f_o+\lambda\sin\phi) = \int y(t_o+\lambda\cos\phi+t'/2)z^*(t_o+\lambda\cos\phi-t'/2) \times e^{-\jmath 2\pi(f_o+\lambda\sin\phi)t'}\,\mathrm{d}t' \tag{3.32a}$$

$$\equiv W_{\tilde{y}\tilde{z}}(\lambda\cos\phi, \lambda\sin\phi) \ , \tag{3.32b}$$

where the signals $\tilde{y}(t)$ and $\tilde{z}(t)$ are defined as

$$\tilde{y}(t) = y(t+t_o)e^{-\jmath 2\pi f_o t} \tag{3.33}$$

$$\tilde{z}(t) = z(t+t_o)e^{-\jmath 2\pi f_o t} \ . \tag{3.34}$$

Using the projection–slice theorem, this radial slice of the $W_{\tilde{y}\tilde{z}}(t,f)$ can be expressed as the 1–D FT of the ϕ–Radon projection $\mathcal{R}DN\ [A_{\tilde{y}\tilde{z}}](r,\phi)$ of the $A_{\tilde{y}\tilde{z}}(\nu,\tau)$

$$W_{\tilde{y}\tilde{z}}(\lambda\cos\phi,\lambda\sin\phi)=\int \mathcal{R}DN\ [A_{\tilde{y}\tilde{z}}](r,\phi)e^{-\jmath 2\pi\lambda r}\,\mathrm{d}r\ \ , \tag{3.35}$$

where the ϕ–Radon projection is given in terms of the $(a-1)^{\text{th}}$ order FrFTs of the signals $\tilde{y}(t)$ and $\tilde{z}(t)$:

$$\mathcal{R}DN\ [A_{\tilde{y}\tilde{z}}](r,\phi)=\tilde{y}_{(a-1)}(r/2)\tilde{z}^{*}_{(a-1)}(-r/2)\ \ . \tag{3.36}$$

Finally substituting (3.35) and (3.36) into (3.32) gives

$$W_{yz}(t_o+\lambda\cos\phi,f_o+\lambda\sin\phi)=\int \tilde{y}_{(a-1)}(r/2)\tilde{z}^{*}_{(a-1)}(r/2)e^{-\jmath 2\pi\lambda r}\,\mathrm{d}r\ \ . \tag{3.37}$$

Discretization of this expression as in (3.17) yields the fast computational algorithm which is tabulated in Algorithm 4.

3.5 Simulations

In this section, by using simulations, we will investigate the performance of the proposed algorithms. For this purpose, we consider the signals with analytically known ambiguity functions and Wigner distributions. This way, we will be able to investigate the error due to discretization of the fractional Fourier transformation on the obtained samples. First we will investigate the performance of the Algorithm 3 which computes the samples of the ambiguity function on arbitrary line segments. In this simulation, we use a linear–frequency modulated chirp signal with a rectangular envelope, $x(t)=\mathrm{rect}(t/T)e^{\jmath\pi[at^2+2bt]}$, where the $\mathrm{rect}(\cdot)$ function takes the value 1 if its argument falls into the range $[-T/2,\ T/2]$, a is the rate of the chirp and b is its initial phase. The corresponding ambiguity function has the following closed form expression:

$$A_x(\nu,\tau)=e^{\jmath 2\pi\tau b}\ (T-|\tau|)\,\mathrm{sinc}((\nu+a\tau)(T-|\tau|))\,\mathrm{rect}(\tau/2T)\ \ . \tag{3.38}$$

In the simulation performed here, the values of the parameters are chosen as $T=6$, $a=-1/4$ and $b=1$. Then by sampling $x(t)$ at a rate $\Delta_x=14$, we obtained $N=196$ uniformly spaced samples in the interval $[-\Delta_x/2,\ \Delta_x/2)$. Since the significant energy of the

a^{th} order FrFTs of $x(t)$ are confined into this interval, no scaling is applied to the continuous time signal $x(t)$. In other words the value of the scaling parameter is given as $s = 1$ which is also true for the other simulations in this section. In Fig. 3.4 (a), Algorithm 3 is used to compute the AF samples on the full polar grid with the angular spacing of $\pi/85$ radians and radial spacing of $\Delta_x/210$ normalized units. As shown in Fig. 3.4 (b), by using the same algorithm, samples of the AF can also be obtained over a partial polar grid with the same angular and radial sampling intervals. For the display purpose, the AF of the same signal could also be computed on a Cartesian grid. In this simulation, first the AF is computed by using the algorithm in [1], on the whole Cartesian grid with Doppler and delay spacings of $1/\Delta_x$ units. Then, in Fig. 3.4(c) and (d), real parts of the computed AF samples which reside on a full and partial circular disks with radius 3 are plotted, respectively. To investigate the accuracy of the proposed algorithm, we computed in $O(N \log N)$ flops the samples of the ambiguity function of the same chirp pulse over the radial line–segment shown in Fig. 3.5(a). The real parts of the computed samples and their deviation from the samples computed by using (3.38) are shown in Fig. 3.5 (b) and (c), respectively. As it can be seen from this example, the computed samples are highly accurate. Alternatively, the samples on the line segment shown in Fig. 3.5 (a) could be approximated from the computed AF samples on the Cartesian grid by using a crude interpolator such as the nearest neighbor interpolator. The result of this alternative approach is shown in Fig. 3.5(d) where the real parts of the computed samples are plotted. With the comparison of the approximation errors in Fig. 3.5 (c) and (e), it becomes apparent that the new algorithm produces a 10 times more accurate result for this simulation. Furthermore, when the line segment has arbitrary orientation with $O(N)$ samples on it, the alternative computation based on the Cartesian grid requires $O(N^2 \log N)$ flops. On the other hand, by using Algorithm 3, the same AF samples can be computed with 10 times more accuracy only in $O(N \log N)$ flops!

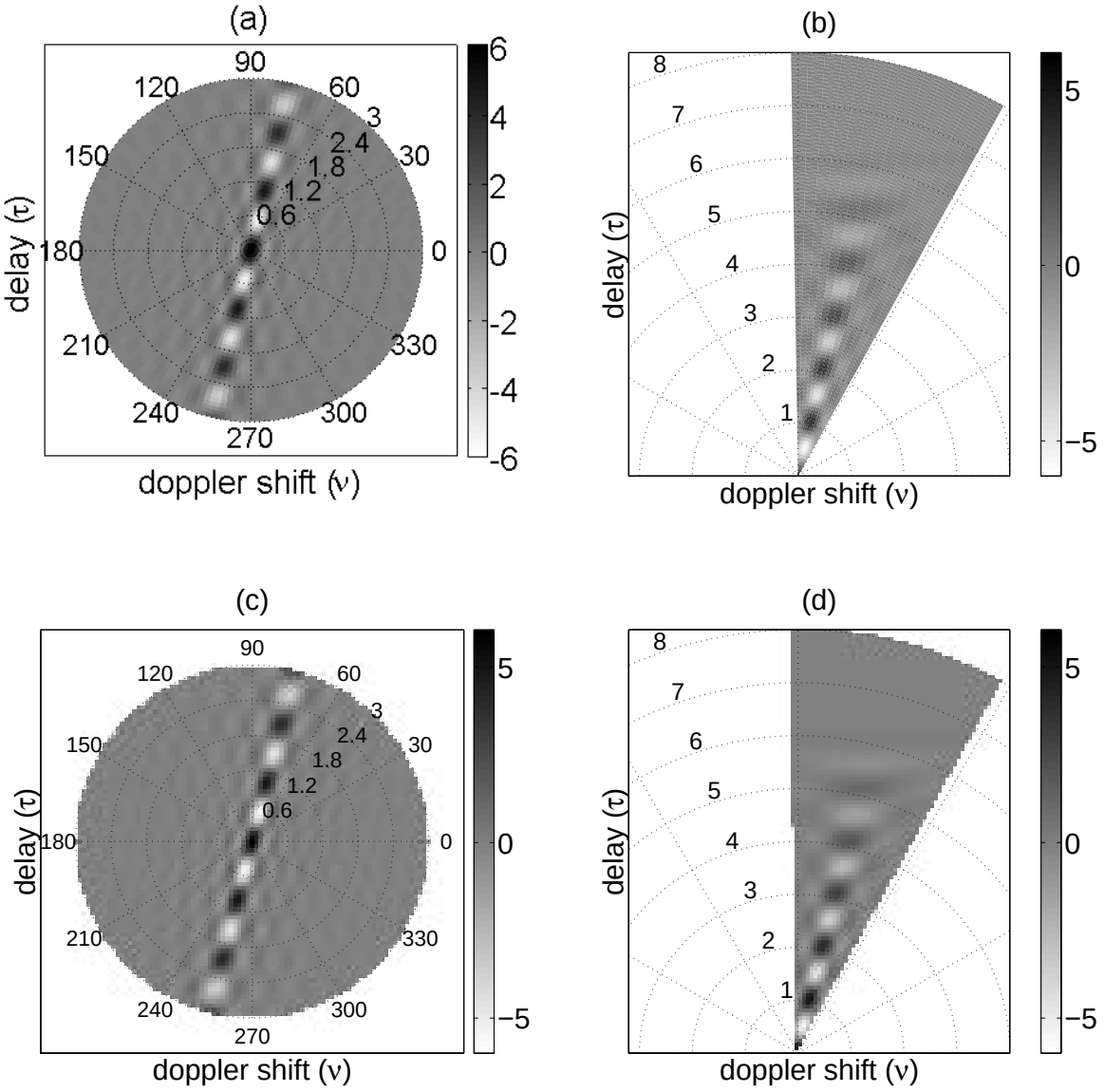

Figure 3.4: The digital computation of the AF of a chirp signal with a rectangular envelope: In the top two plots the real part of the AF of the pulse is computed on (a) full and (b) partial polar grids by repeated use of the Algorithm 3. For the purpose of comparison, the AF samples are also computed on a Cartesian grid by using [1]. In (c) and (d), the real parts of these AF samples which lie on a full and partial circular disks are plotted, respectively.

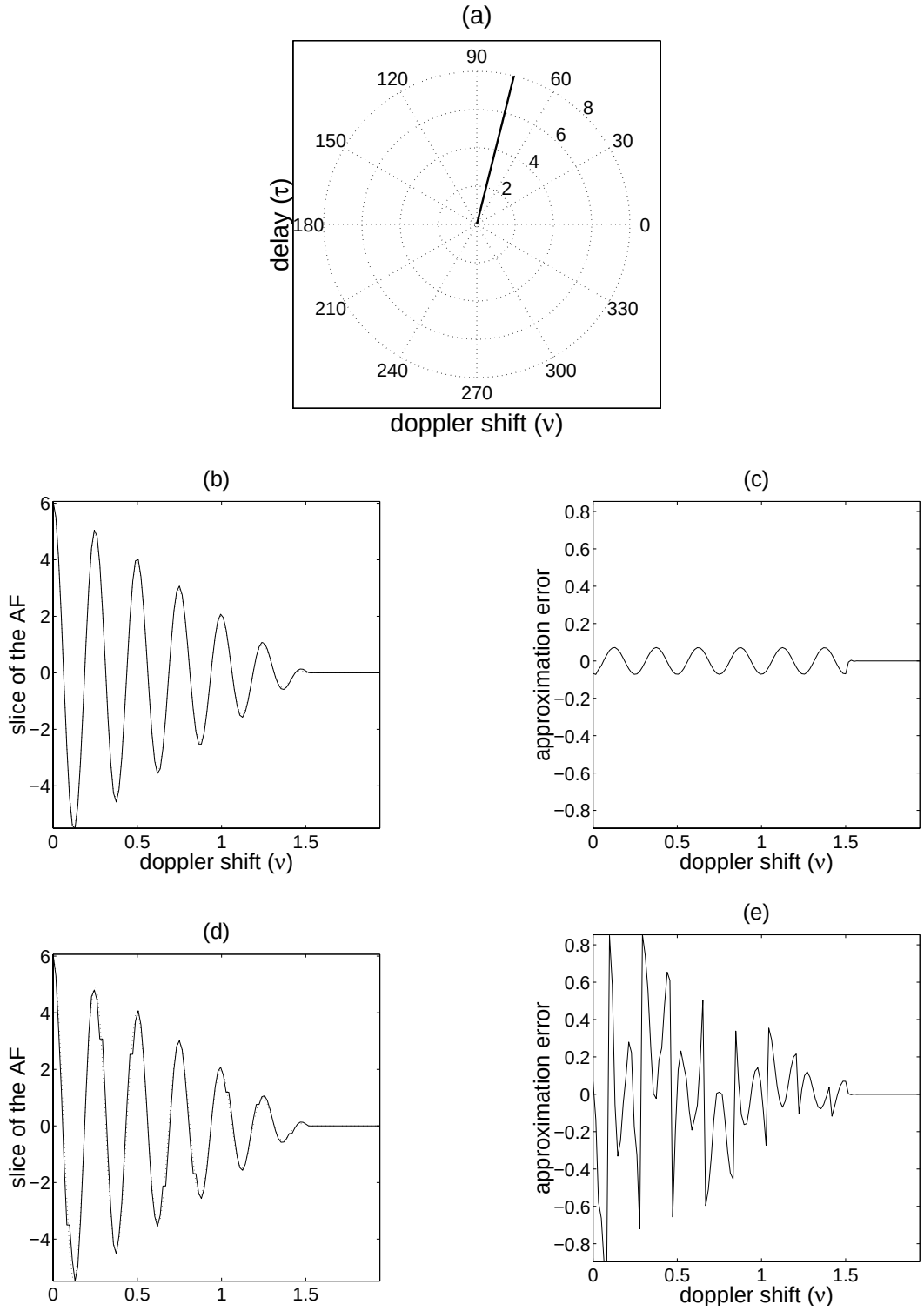

Figure 3.5: The digital computation of the AF of a chirp signal with a rectangular envelope: (a) shows the support of a radial line segment on which the samples of the AF given in Fig. 3.4 are computed. The real parts of the actual and computed AF samples on this line segment by using Algorithm 3 are in very good agreement as shown by the close overlay in (b). The error in the computation shown in (c) reveals the highly accurate nature of the computational algorithm. In (d), the same AF samples are approximated from the samples on the Cartesian grid by using nearest neighbor interpolation. The peak approximation error in (e) is approximately 10 times larger than the one in (c).

Next we investigate the accuracy of the algorithms in computing the WD of the Gaussian pulse $x(t) = 2^{1/4}e^{-\pi t^2}$, which has the Wigner distribution

$$W(t, f) = 2e^{-2\pi(t^2+f^2)} \quad . \tag{3.39}$$

By sampling $x(t)$ at a rate $\Delta_x = 10\sqrt{2}$, we obtained $N = 200$ uniformly spaced samples in the interval $[-\Delta_x/2,\ \Delta_x/2)$. The plots (a) and (b) in Fig. 3.6 are obtained by repeated application of the Algorithm 4. In plot (a) the WD is computed over a full and in plot (b) it is computed over a partial polar grid. For the purpose of comparison, the WD samples are also computed on a Cartesian grid by using the algorithm in [2] with a sampling interval of $1/(2\Delta_x)$ units both in time and frequency. Then, in Fig. 3.6(c) and (d), only the WD samples which lie on a full and partial circular disks are plotted.

To show the accuracy of the proposed algorithm, we computed in $O(N \log N)$ flops, samples of the Wigner distribution of the same Gaussian pulse over the non–radial line–segment shown in Fig. 3.7(a). The obtained samples and the approximation error are plotted in Fig. 3.7(b) and (c) respectively. For the purpose of comparison, the same AF samples are approximated from the Cartesian grid samples by using nearest neighbor interpolation. In Fig. 3.7(d) the approximated and actual AF samples, and in Fig. 3.7(e) the computation error are shown. As in the AF case presented above, not only the accuracy of the computed samples shown in Fig. 3.7(e) is significantly less than the accuracy obtained by using Algorithm 4, but also the computation of the Cartesian grid based algorithm requires $O(N^2 \log N)$ flops.

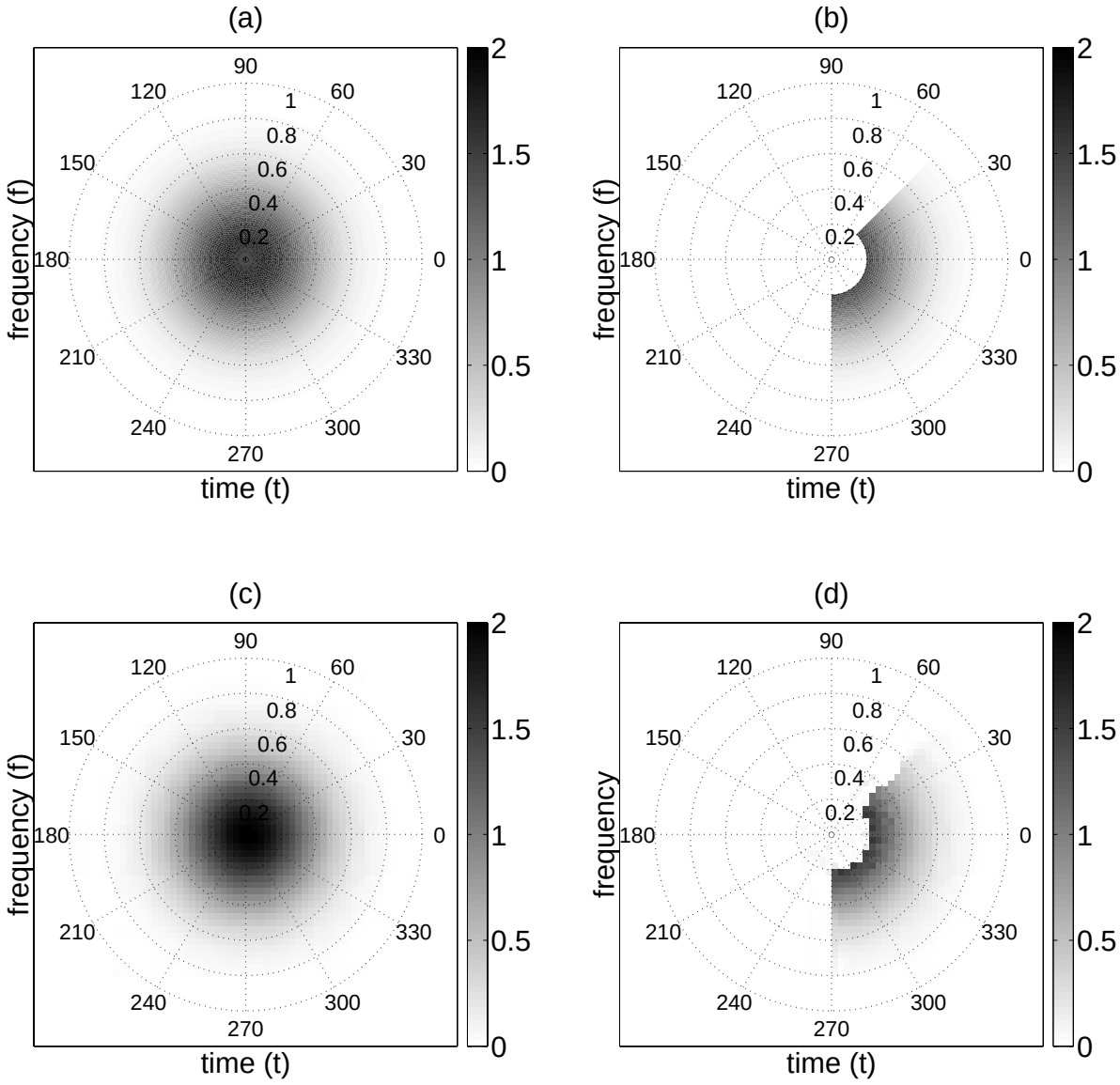

Figure 3.6: The digital computation of the WD of a Gaussian pulse: In the top two plots the WD of the pulse is computed on (a) full and (b) partial polar grids by repeated use of the Algorithm 4. For the purpose of comparison, the WD samples are also computed on a Cartesian grid by using [2]. In (c) and (d), the WD samples which lie on a full and partial circular disks are plotted, respectively.

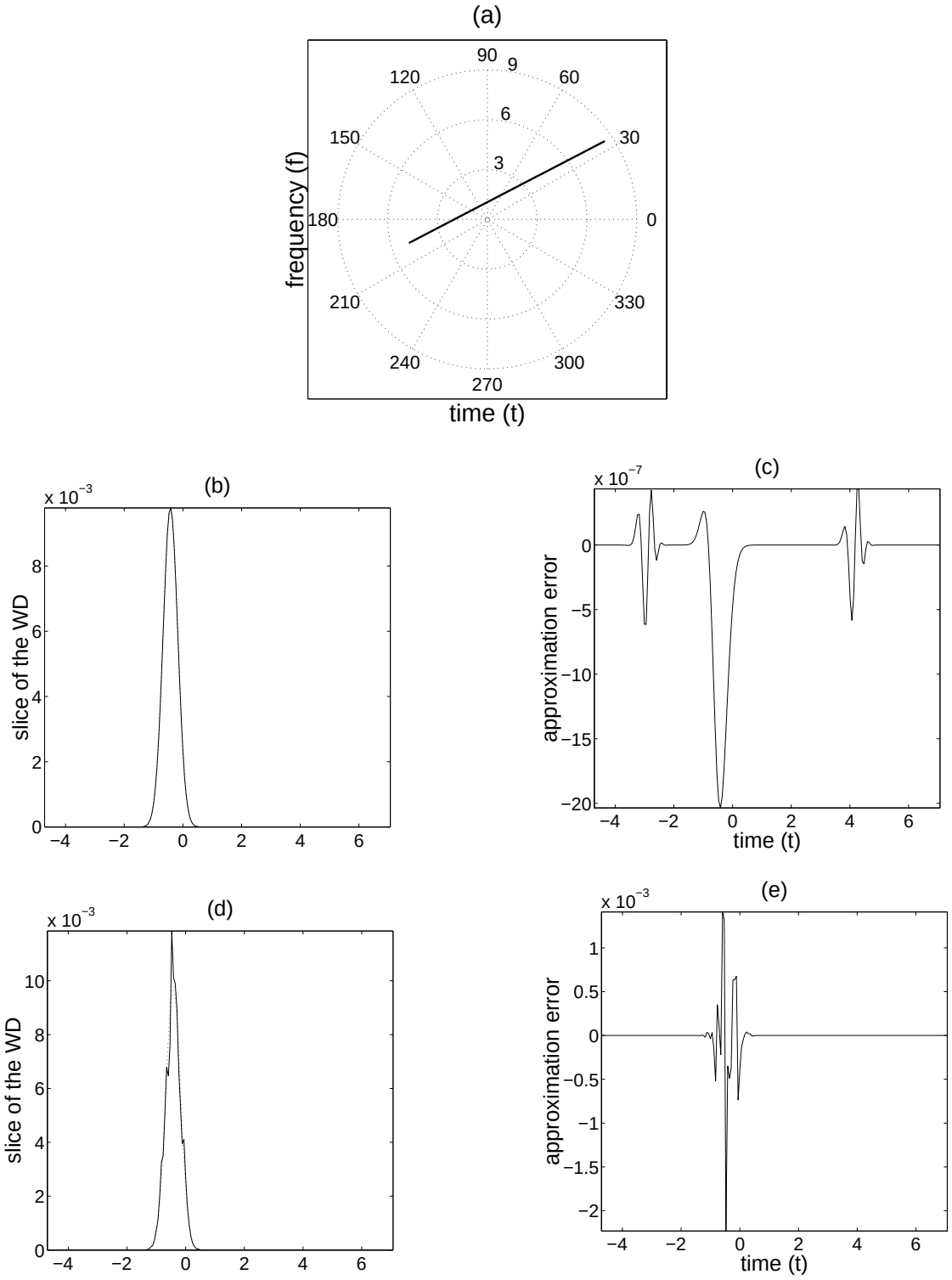

Figure 3.7: The digital computation of the WD of a Gaussian pulse: (a) shows the support of a non–radial line segment on which the samples of the WD given in Fig. 3.6 are computed. The actual and computed WD samples on this line segment are in very good agreement as shown by the close overlay in (b). The error in the computation shown in (c) reveals the highly accurate nature of the computational algorithm. In (d), the same WD samples are approximated from the samples on the Cartesian grid by using nearest neighbor interpolation. The error shown in (e) is approximately 1000 times larger than the one in (c).

Next we consider the digital computation of the WD of a multi–component signal $x(t)$ which is composed of two chirp pulses $x_1(t)$ and $x_2(t)$:

$$x(t) = x_1(t) + x_2(t) \ . \tag{3.40}$$

The chirp pulses are chosen as

$$x_k(t) = e^{\jmath\pi[a(t-to)^2+2b_k(t-t_o)]} \operatorname{rect}((t-t_o)/T) \ , \tag{3.41}$$

for $k = 1$ or 2. The WD of $x(t)$ can be analytically computed as

$$\begin{aligned} W_x(t,f) &= W_r(t-t_o, f-at-b_1) + W_r(t-t_o, f-at-b_2) \\ &\quad +2\cos(2\pi(b_2-b_1)(t-t_o))W_r(t-t_o, f-at-(b_1+b_2)/2) \ , \end{aligned} \tag{3.42}$$

where $W_r(t,f)$ is the WD of the $\operatorname{rect}(t/T)$ function:

$$W_r(t,f) = 2T(1-2|t|/T)\operatorname{rect}(t/T)\operatorname{sinc}(2(1-2|t|/T)fT) \ . \tag{3.43}$$

In (3.42), the first two terms are the auto–terms and the third one is the cross–term.

For the reported simulation here, the parameters of $x(t)$ are chosen as $\Delta_x = 30$, $a = -3$, $b_1 = 3$, $b_2 = -1$, $t_o = 3$ and $T = 5 + 1/\Delta_x$. The WD of $x(t)$ with these parameters is digitally computed on a grid like the one in Fig. 3.2(d) by using the Algorithm 4. The obtained result shown in Fig. 3.8(a) demonstrates the agreement with the analytical result given in (3.42). In this plot, we easily identify the auto–terms of the WD as the two darker shaded lines which are closer to the edges, and we identify the cross–term as the line which is at the middle part of the plot. The cross–term is highly oscillatory because of the cosine modulation in (3.42). In Fig. 3.8(b) and Fig. 3.8(c) computed samples of the auto and cross terms are shown over highly localized grids of the type given in Fig. 3.2(d). Finally, in Fig. 3.8(d) we provide the approximation error for the auto–terms only.

In Fig. 3.9, the Radon–Wigner transform and Radon–ambiguity function transform of the same multi–component signal are computed on polar grids by using the fractional Fourier transform relations (3.3) and (3.20). The locations of the peaks in the RWT are related to the rate and initial phase of the chirps in (3.41). When the chirp components are contaminated with additive white Gaussian noise, the locations of the peaks in the Radon–Wigner transform provide the maximum likelihood estimate of these parameters [82], [87]. Note that the

computation of the RWT and the RAFT of a signal over a full polar grid requires the computation of the same set of fractional Fourier transforms of the signal. Hence, when these transforms are to be calculated simultaneously, significant computational saving can be achieved by avoiding any extra computation of the FrFT samples.

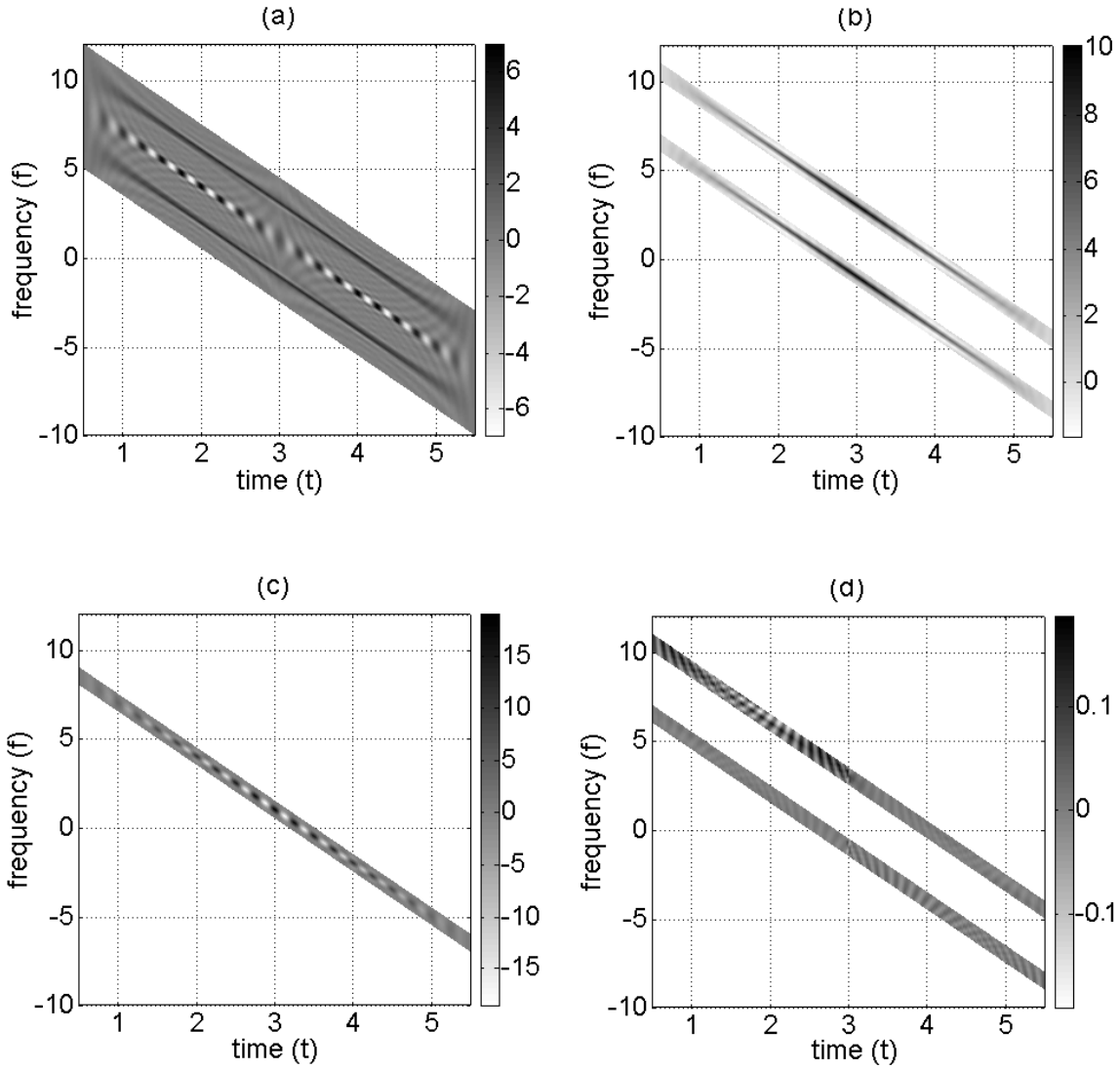

Figure 3.8: Computation of the WD samples of a multi–component chirp signal over various parallelogram grids to investigate the (a) whole, (b) auto and (c) cross terms. The efficient computation of the highly localized samples of the WD as in plots (b), (c) has a wide range application areas including component analysis, signal detection and signal extraction for non–stationary signals. As shown in (d), the error in the computed samples of the auto terms is very small.

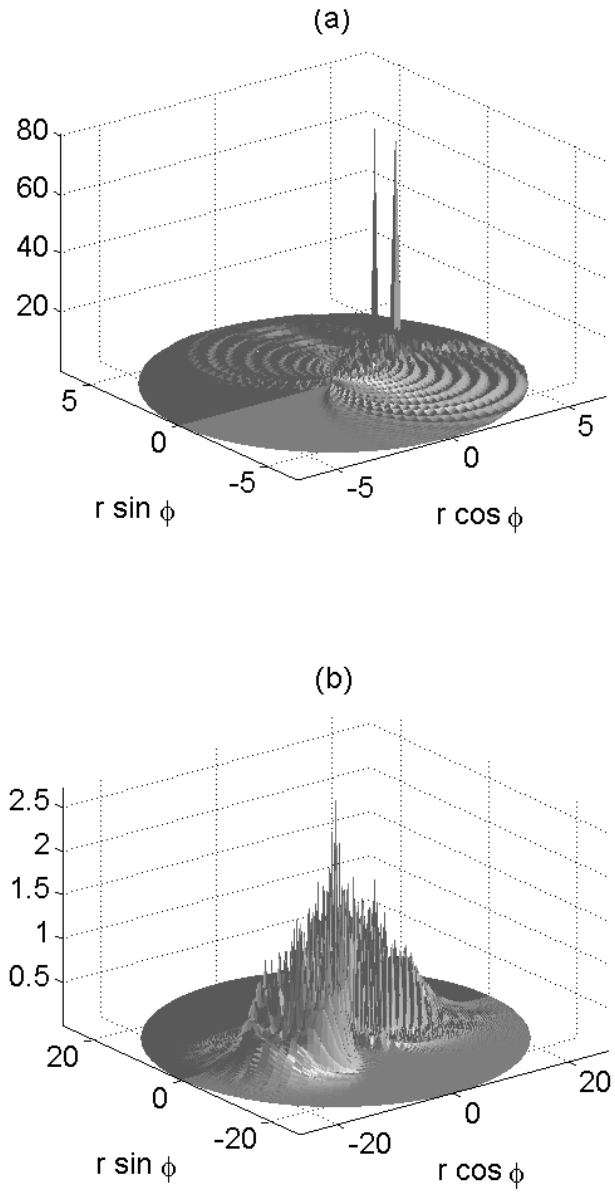

Figure 3.9: The digital computation of (a) the Radon–Wigner transform and (b) magnitude of the Radon–ambiguity function transform. In this chapter, the computation of these transforms constitute the intermediate steps in computation of the ambiguity function and the Wigner distribution on polar grids. These transforms have important applications in signal detection, multi–component signal analysis and data–adaptive kernel design for time–frequency signal analysis.

3.6 Conclusions

By using the fractional Fourier transformation of the time-domain signals, closed form expressions for the projections of their auto and cross ambiguity functions are derived. Based on a similar formulation for the projections of the auto and cross Wigner distributions and the well known 2-D Fourier transformation relationship between the ambiguity and Wigner domains, closed form expressions are obtained for the slices of both the Wigner distribution and the ambiguity function. By using the obtained analytical results, efficient algorithms are proposed for the computation of the auto or cross Wigner distribution and ambiguity function samples on arbitrary line segments. The proposed algorithms make use of a digital computation algorithm to approximate N uniformly spaced samples of FrFT in $O(N \log N)$ flops. The ability of obtaining samples on arbitrary line segments provides significant flexibility not only in computation of the high resolution distribution provided by TFCA but also in numerous computational applications of the Wigner distribution and the ambiguity function.

Chapter 4

The Simplified Version of the TFCA for Signals with Convex Time–Frequency Supports

4.1 Introduction

Much of the research in time–frequency signal processing has been devoted to design of new time–frequency representations. Among the representations developed so far the Wigner distribution has attracted much of the attention because of its nice theoretical properties [2], [6], [20], [21]. For signals with convex time–frequency supports, the WD gives the highest auto–term concentration. However, since it is a bilinear representation, it suffers from severe cross–term interference in the presence of more than one signal components. For instance the Wigner distribution of a multi–component signal $x(t) = \sum_{i=1}^{m} s_i(t)$ contains $m(m-1)/2$ cross terms of the form $2\mathfrak{Re}\{W_{s_i s_j}(t,f)\}$, $i < j$, in addition to the auto–components $W_{s_i s_i}(t,f) \equiv W_{s_i}(t,f)$, where $W_{s_i s_j}(t,f)$ is the cross WD of the signals $s_i(t)$ and $s_j(t)$ as defined in (2.3). The cross–terms usually interfere with the auto–components and decrease the interpretability of the Wigner distribution. Thus the existence of cross–terms limits the use of the Wigner distribution in some practical applications.

The geometry of the cross–terms has been extensively analyzed [23]. It has been found that

the cross terms lie at mid–time and mid–frequency of the auto–components, they are highly oscillatory and the frequency of oscillations increases with the increasing distance in time and frequency. Furthermore, cross–terms might have a peak value as high as twice that of the auto–components. Since cross–terms are highly oscillatory, it has been suggested that some sort of smoothing of the Wigner distribution is necessary to suppress the cross–terms.

In a unified framework, the distributions obtained by low–pass filtering the Wigner distribution are studied under the name of Cohen's bilinear class of shift invariant distributions [6]. In this class, the time–frequency distribution $TF_x(t,f)$ of a signal $x(t)$ is obtained as shown in (2.1). Equivalently, the time–frequency distribution of the signal $x(t)$ corresponding to a fixed kernel $\kappa(\nu,\tau)$ can be written as

$$TF_x(t,f) = \iint A_x(\nu,\tau)\kappa(\nu,\tau)e^{-\jmath 2\pi(\nu t+\tau f)}\,\mathrm{d}\nu\,\mathrm{d}\tau \quad , \tag{4.1}$$

where $A_x(\nu,\tau)$ is the (symmetric) ambiguity function given in (2.4b). The drawback of this class of distributions is that a fixed kernel can perform well only for a limited class of signals whose auto–terms in the AF plane are located inside the pass–band region of the kernel $\kappa(\nu,\tau)$. For other signals they offer a trade–off between good cross–term suppression and high auto–term concentration. Therefore to obtain a high–quality time–frequency representation, the kernel must be adapted to the characteristics of the input signal to obtain a data–adaptive smoothing. These considerations led to the development of Cohen's class of time–frequency representations with data–dependent kernels [6].

In this chapter we develop a novel approach to design data–adaptive time–frequency distributions for composite signals. Being a simpler version of TFCA, the new technique is tailored to analysis of composite signals whose components have *convex* time–frequency supports. Although, the analysis of this type of signals has been studied in depth in literature, the proposed method provides considerably better distribution than well–known techniques. In contrast to the vast body of previous work, the proposed approach is based on the Radon transform of the ambiguity function of the input signal, which is called as the Radon ambiguity function transform as defined in Section 3.3.1. By performing windowing on the resultant RAFT's, it eliminates significant part of the *outer* interference terms without reducing the auto–component concentration. Another limited but more advanced version of the TFCA

algorithm, which is capable of removing the *inner* interference terms of signals with *non–convex* time–frequency supports will be given in Chapter 5.

The outline of this chapter is as follows. In Section 4.2 the mathematical details of the new approach are given, in Section 4.3 some simulation results are presented and in Section 4.4 some conclusions are drawn.

4.2 Directional Smoothing of the Wigner Distribution

The suppression of cross–terms is usually performed by smoothing the WD with a low–pass filter. When, the low–pass filter is not appropriately chosen, the WD is smoothed in many directions in the time–frequency plane. However, if the auto–terms of the signal do not have low–pass characteristics along all orientations, naturally this leads to broadening of the auto–terms. For instance the WD slice of a linear frequency modulated chirp has a low–pass characteristic when the slice is along the chirp's major axis, but is has considerably higher frequency content when the slice is lying along its minor axis as illustrated in Fig. 4.1. Thus, during smoothing the WD to suppress the cross–terms, the broadening of the auto–terms can be avoided by using directional low–pass filters with adaptively chosen cut–off frequencies. By smoothing each auto–term only along its support, the oscillatory cross–terms with significant high–frequency content are suppressed without essentially decreasing the auto–component concentration. At the end a high resolution time–frequency distribution is obtained.

In this chapter, we assume that supports of the auto–components or the regions of the Wigner plane which are suspected to contain auto–components are specified before–hand. What has to be done is to efficiently filter the slices of these regions with data–adaptive low–pass filters. In the next subsection we develop a procedure to efficiently filter any arbitrarily chosen slice of the WD.

4.2.1 Directional Filtering Algorithm

Suppose that we want to filter the non–central Wigner distribution slice, $W_x(t_o + \lambda\cos\phi, f_o + \lambda\sin\phi)$, of $x(t)$ which passes through the point (t_o, f_o) and makes an angle of ϕ with

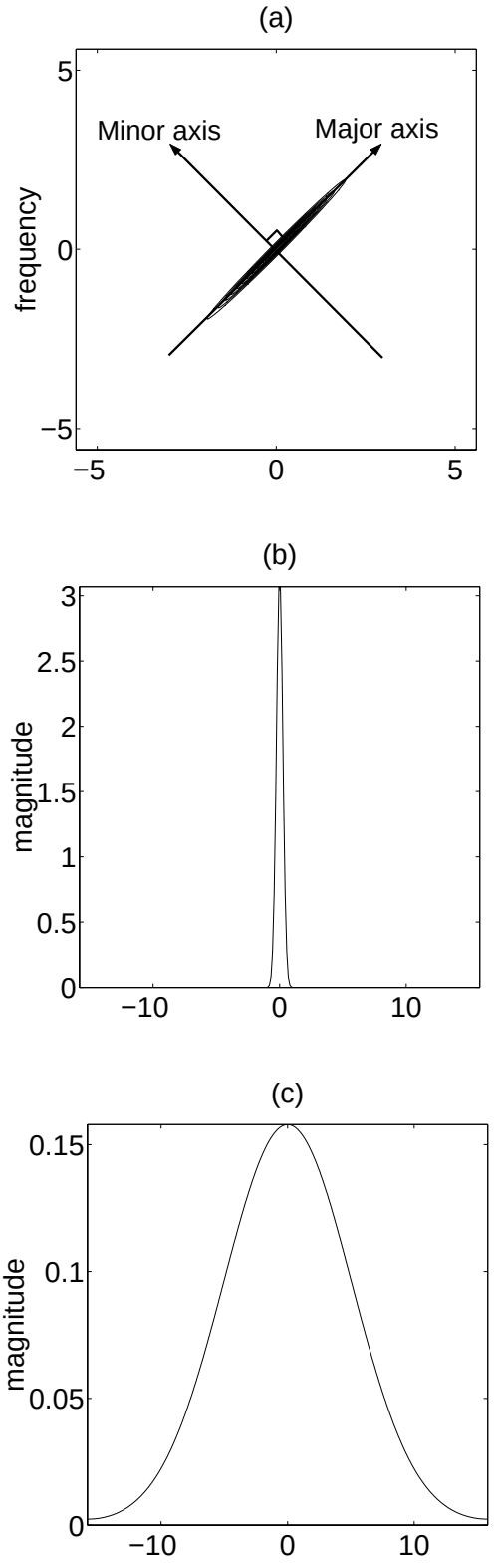

Figure 4.1: An illustration showing that different time–frequency slices of a signal may have significantly different bandwidths. For instance, although the WD slice of the chirp signal whose t–f distribution given in (a) has a low–pass spectrum along the major axis as shown in (b), it has considerably broader bandwidth along the minor axis as shown in (c).

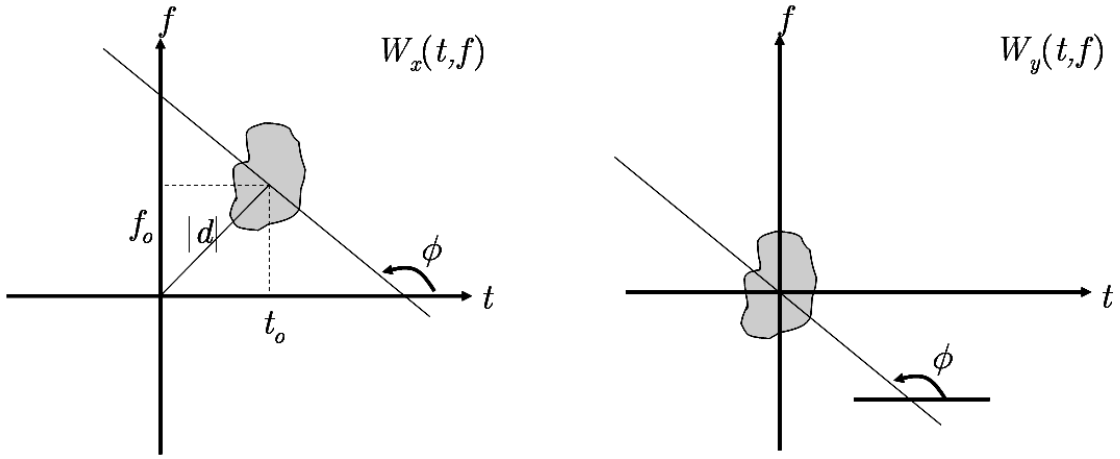

Figure 4.2: An illustration showing that the non–central (left) slice of a Wigner distribution $W_x(t,f)$ is the same as the central (right) slice of a Wigner distribution $W_y(t,f)$ when $y(t) = x(t+t_o)e^{-\jmath 2\pi f_o t}$. This basic relationship is used in Section 4.2 to compute the adaptively smoothed slices of the Wigner distribution $W_x(t,f)$.

the time–axis as shown in Fig. 4.2 . It is straightforward to prove that this non–central Wigner distribution slice of $x(t)$ is the same as the central Wigner distribution slice, $W_y(\lambda\cos\phi, \lambda\sin\phi)$, of $y(t)$ at the same angle ϕ (see Fig. 4.2) provided that the latter signal is defined in terms of the original one through the relation

$$y(t) = x(t+t_o)e^{-\jmath 2\pi f_o t} \quad . \tag{4.2}$$

Thus we can formulate the filtering problem in terms of the WD W_y. By denoting the radial slice of the WD W_y as $\mathcal{SLC}\ [W_y](\lambda,\phi) \equiv W_y(\lambda\cos\phi, \lambda\sin\phi)$, and impulse response of the real smoothing filter as $h(t)$, the directional filtering can be mathematically expressed as

$$s(\lambda,\phi) = h(\lambda) \underset{\lambda}{*} \mathcal{SLC}\ [W_y](\lambda,\phi) \quad , \tag{4.3}$$

where $s(\lambda,\phi)$ is the slice of the filtered Wigner distribution. By using the projection slice theorem [84], the central slice of the Wigner distribution W_y can be expressed as the Fourier transform of the Radon transform of the ambiguity function A_y:

$$\mathcal{SLC}\ [W_y](\lambda,\phi) = \int \mathcal{RDN}\ [A_y](r,\phi)e^{-\jmath 2\pi r\lambda}\,\mathrm{d}r \quad , \tag{4.4}$$

where the Radon transform of the ambiguity function is defined as

$$\mathcal{RDN}\ [A_y](r,\phi) = \int A_y(r\cos\phi - s\sin\phi, r\sin\phi + s\cos\phi)\,\mathrm{d}s \quad . \tag{4.5}$$

Thus (4.3) can be expressed in the (inverse) Fourier transform domain as

$$S(r,\phi) = H(r)\,\mathcal{R}DN\,[A_y](r,\phi)\ , \tag{4.6}$$

where $S(r,\phi)$ is the inverse Fourier transform of the slice $s(\lambda,\phi)$ with respect to the radial variable λ, and $H(r)$ is the inverse Fourier transform of the smoothing filter $h(t)$. As tabulated below, this equation gives the basis of the algorithm for filtering any slice of the Wigner distribution of a signal $x(t)$:

Algorithm 1 Directional Filtering Algorithm

Object of the algorithm: Given $y(t) = x(t+t_o)e^{-\jmath 2\pi f_o t}$ to smooth the non–central slice of the WD of $x(t)$ as shown in Fig. 4.2.

Steps of the algorithm:

1. Compute the Radon transform $\mathcal{R}DN\,[A_y](r,\phi)$ of the ambiguity function $A_y(\nu,\tau)$.
2. Design a multiplicative filter $H(r)$ to capture the energy around the origin and suppress the cross–terms away from the origin.
3. Apply the multiplicative filter $H(r)$ to the Radon transform $\mathcal{R}DN\,[A_y](r,\phi)$ to obtain $S(r,\phi)$.
4. Compute the slice $s(\lambda,\phi)$ of the smoothed distribution from $S(r,\phi)$ by using the Fourier transformation.

This procedure can be repeated on different slices where adaptively chosen filters are utilized on each slice depending on the auto–component location in the corresponding $\mathcal{R}DN\,[A_y](r,\phi)$. In digital implementation, the computation of the radon transform from ambiguity function requires $O(N^2)$ operations for a signal of N samples duration. Thus, to have a practically useful algorithm, we have to obtain the Radon transform of the ambiguity function efficiently. As we prove in Appendix A, the Radon transform of the ambiguity function $A_y(\nu,\tau)$ can be computed as

$$\mathcal{R}DN\,[A_y](r,\phi) = x_{(a-1)}(r/2+d)\,x^*_{(a-1)}(-r/2+d)\ , \tag{4.7}$$

where $a = 2\phi/\pi$ and $x_{(a-1)}(t)$ is the $(a-1)^{\text{th}}$ order fractional Fourier transformation [88] of the signal $x(t)$ and in polar format $(d,\phi-\pi/2)$ is the closest point on the non–central slice of the WD to the origin as shown in Fig. 4.2. Thus, by using (4.6) and (4.7), the smoothed non–central WD slice of $x(t)$ is obtained as

$$SW_x(t_o+\lambda\cos\phi,\, f_o+\lambda\sin\phi) = \int H(r)\,x_{(a-1)}(r/2+d)\,x^*_{(a-1)}(-r/2+d)e^{-\jmath 2\pi r\lambda}\,\mathrm{d}r\ . \tag{4.8}$$

Since digital computation of the fractional Fourier transform of a signal with N samples duration requires only $O(N \log N)$ operations [85], by discretization of (4.8), each WD slice of $x(t)$ can be smoothed in $O(N \log N)$ operations.

The expression given by (4.8) is in a form which is very suitable for digital computation. However, to find the kernel of the distribution, the effect of the directional smoothing should be investigated on the cartesian grid. For instance, if the smoothing operation is carried out in a single direction at all parts of the time–frequency plane, it can be shown that, the resultant distribution is equivalent to

$$SW_x(t,f) = W_x(t,f) \underset{t,f}{**} \left(h(t\cos\phi - f\sin\phi)\delta(t\sin\phi + f\cos\phi)\right) \quad . \tag{4.9}$$

Hence, the obtained distribution is in the Cohen's class of time–frequency distributions and $h(t\cos\phi - f\sin\phi)\delta(t\sin\phi + f\cos\phi)$ is the Fourier transform of the kernel $\kappa(\nu,\tau)$ of the distribution given in (2.1). On the other hand, if there are multiple components lying at different orientations, each component is smoothed along its orientation. Thus, the resultant distribution becomes

$$SW_x(t,f) = \sum_i \left[W_x(t,f) \underset{t,f}{**} \left(h_i(t\cos\phi_i - f\sin\phi_i)\delta(t\sin\phi_i + f\cos\phi_i)\right) \right] M_i(t,f) \quad , \tag{4.10}$$

where ϕ_i denotes the orientation angle of the i^{th} component in the time–frequency plane, $h_i(\lambda)$ denotes the corresponding smoothing filter and $M_i(t,f)$ is an indicator function denoting the support of the i^{th} component in the time–frequency plane. It should be emphasized that, when multiple components are present in $x(t)$, the resultant distribution is not in Cohen's class of time–frequency distributions, since (4.10) can not be put into the form given in (2.1).

4.3 Simulations

In this section we investigate the performance of the proposed method in removing the cross–terms residing on the auto–components of the Wigner distribution. The synthetic test signal used in the first simulated example is generated by linearly combining 5 linear FM signals with Gaussian envelopes as shown in Fig. 4.3(a). The readability of the Wigner distribution of this multi–component signal is severely degraded by the existence of cross–terms as seen

in Fig. 4.3(b). In Fig. 4.4(a), the Wigner distribution is computed on rectangular grids which contain supports of three of the auto–components. The smoothed WD slices computed by using the proposed approach are plotted in Fig. 4.4(b). In Fig. 4.5(a), the corresponding auto–term WD is given. Although the auto–term WD is a desirable distribution, in general it is not computable. However for the synthetic test signal considered here since the components $s^i(t)$ constituting the composite signal $x(t)$ are known beforehand, auto–term WD can be computed as $W_A(t,f) = \sum_{i=1}^{5} W_{s^i}(t,f)$, where $W_{s^i}(t,f)$ is the WD of $s^i(t)$. In Fig. 4.5(b), the difference between the desired auto–term WD and the computed TFD is plotted to illustrate the good performance of TFCA for this simulation example.

In the next example we investigate the case, where not only the interference terms but also one of the auto–components are superimposed on an auto–component. As shown in Fig. 4.6(a), the Wigner distribution of the multi–component signal displays significant cross and auto–term noise on the chirp signal centered at the origin. In Fig. 4.6(b), the smoothed slices of the WD along this chirp signal are plotted. As it can be seen from this plot, the noise terms are greatly suppressed.

4.4 Conclusions

A simplified form of the TFCA is presented for smoothing slices of the Wigner distribution to suppress the oscillatory cross–term components yielding a highly accurate representation of the auto–terms of the Wigner distribution. The simpler version of the TFCA algorithm, which is tailored for signals with convex–time frequency supports, is based on the recently established relationship between the Radon ambiguity function transform and fractional Fourier transform derived in Chapter 3. In contrast to the smoothing algorithms which work by applying a low pass filter globally to the WD, the new algorithm works locally on the WD slices. As shown by simulation examples, for signal terms with convex time–frequency supports, the proposed algorithm avoids the usual trade–off between cross–term suppression and auto–term broadening by taking into account the characteristics of the cross–terms on the WD slices.

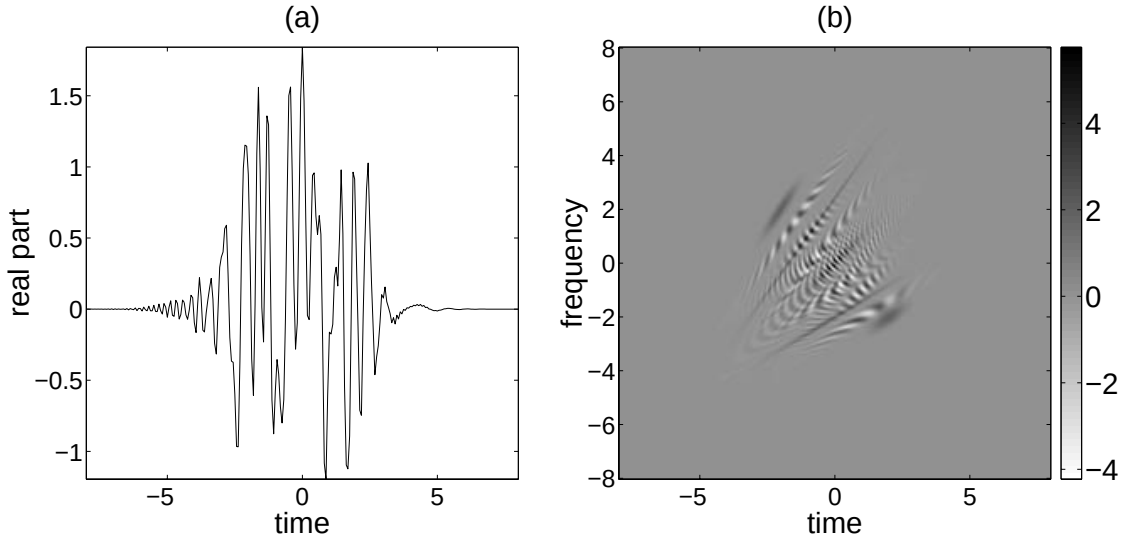

Figure 4.3: (a) The time domain representation of a composite signal which is composed of 5 linear FM signals and (b) the corresponding Wigner distribution.

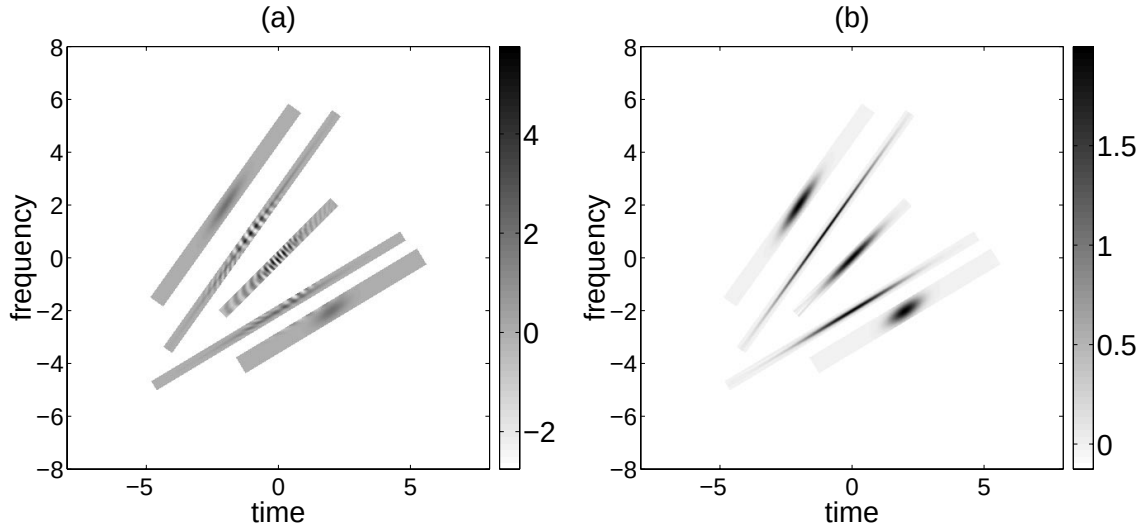

Figure 4.4: (a) The WD slices of the signal given in Fig. 4.3(a), which are computed along auto–term supports by using the Fast Wigner–Slice computation algorithm of Chapter 3. Although the WD slices given in (a) show significant cross–term interference, the smoothed WD slices computed by using the simplified version of the TFCA show negligible interference and auto–term distortion as shown in (b).

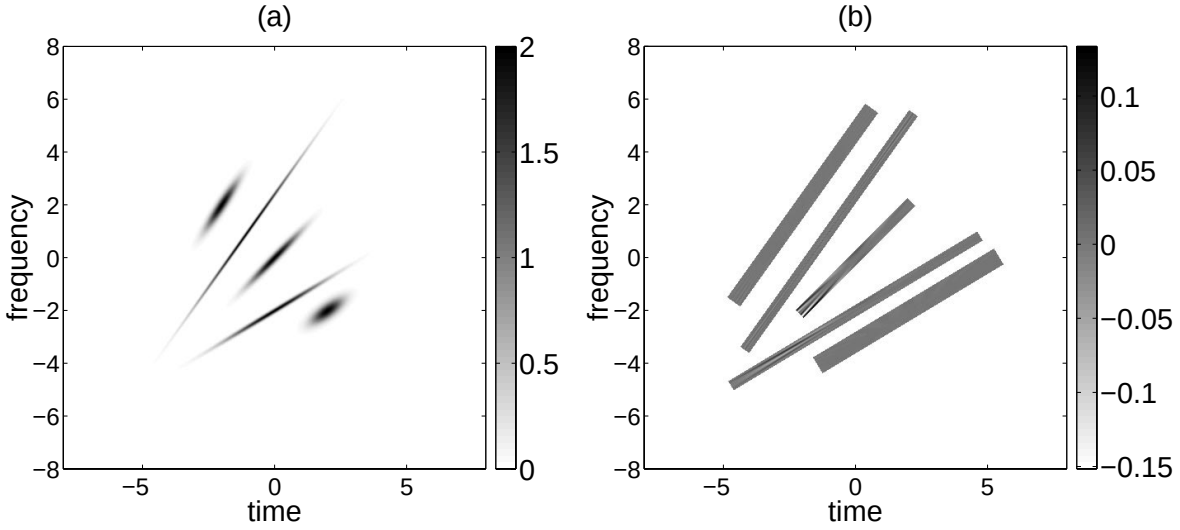

Figure 4.5: (a) The auto–term WD of the signal given in Fig. 4.3 (a), which is obtained by removing any noise and interference terms from its WD. Although the auto–term WD is a desirable distribution, in general it is not computable. However for the synthetic test signal considered here since the components $s^i(t)$ constituting the composite signal $x(t)$ are known beforehand, auto–term WD can be computed as $W_A(t,f) = \sum_{i=1}^{5} W_{s^i}(t,f)$, where $W_{s^i}(t,f)$ is the WD of $s^i(t)$. In (b), the difference between the desired auto–term WD and the computed TFD by TFCA is plotted to illustrate the good performance of TFCA.

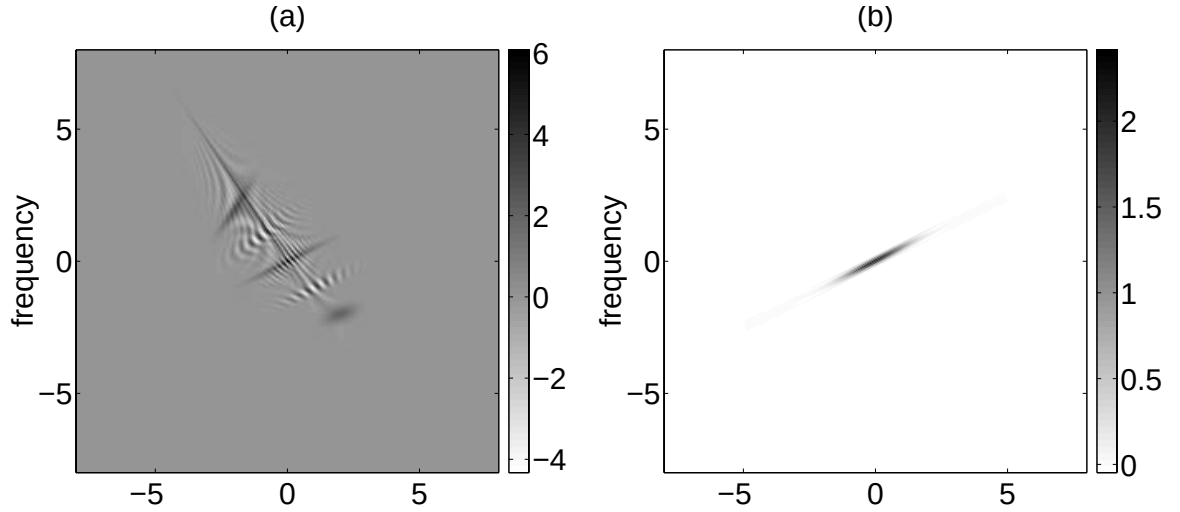

Figure 4.6: This simulation illustrates the use of directional smoothing algorithm when there are overlapping components in the time–frequency plane as shown in (a). The TFD slices along one of the auto–components are computed by using the simplified version of TFCA. The smoothed slices shown in (b) carries little auto–term and cross–term noise.

Chapter 5

The Simplified Version of the TFCA for Mono–Component Signals

5.1 Introduction

Time–frequency analysis is the primary tool for the analysis of non–stationary signals. Much of the research effort in time–frequency analysis is devoted to design of distributions which give a better description of the joint time and frequency content of signals. However, most of the algorithms have a trade–off between sharp auto–term concentration and reduced cross–term interference, or they are computationally very expensive to be useful in practical applications. The TFCA developed in this thesis provides a very sharp description of the signals with complicated structures while suppressing both inner and outer interference terms in the time–frequency plane. For instance, the limited version of the TFCA developed in Chapter 4 avoids the usual trade–off between the auto–term concentration and cross–term interference for signals with convex time–frequency supports by performing directional smoothing on the WD slices on the time–frequency support of the auto components. However, the inner interference terms of components with non–convex time–frequency support could only be partially suppressed by that limited version of the TFCA. To alleviate this problem, in this chapter we develop a more advanced form of the TFCA by incorporating a novel

fractional domain[1] warping technique, which is first presented in [48]. This more general but still limited version of the TFCA can handle not only signals with convex time–frequency supports but also *mono–component* signals with *non–convex* supports in the time–frequency plane. Although the obtained high resolution time–frequency representation does not belong to Cohen's class[2], it gives a very good time–frequency description of *mono–component* signals by suppressing their inner interference terms. When digitally implemented for a signal with N samples duration, the complexity of the algorithm is only $O(N \log N)$ flops for each computed time–frequency slice. The final form of the TFCA, that can handle both *mono* and *multi–component* signals which may have *convex* or *non–convex* time–frequency supports will be presented in Chapter 6.

The outline of the chapter is as follows. In Section 5.2 the concept of fractional domain warping is introduced, in Section 5.3 the mathematical details of the new approach are given on a simulated example and finally in Section 5.4 conclusions are drawn.

5.2 Fractional Domain Warping

Time domain warping is especially useful in the processing of frequency modulated signals. It has been utilized in a diverse set of applications such as speaker and speech recognition [89], transversal filtering with non–uniform tap spacing [90], synthesis of time–varying filters for frequency varying signals [91] and time–frequency signal decomposition [92]. A typical member of frequency modulated signals is in the form of $x(t) = A(t)e^{j2\pi\varphi(t)}$, where $A(t)$ is the narrow–band amplitude and $\varphi(t)$ is the phase in Hz. Ideally, the warping function for the FM signal should be chosen as the inverse of its phase, $\zeta(t) = \varphi^{-1}(f_s t)$, where $f_s > 0$ is an arbitrary scaling constant. With this choice, the warped function takes the following form

$$x_\zeta(t) \equiv x(\zeta(t)) = A(\zeta(t))e^{j2\pi f_s t} \quad . \tag{5.1}$$

which is a sinusoidal function at frequency f_s with envelope $A(\zeta(t))$. Consequently, the algorithms designed to operate on sinusoidal signals can be utilized on the warped signal $x_\zeta(t)$.

[1] Fractional domain is also called fractional Fourier transform domain [53].

[2] It does not belong to Cohen's class of time–frequency distributions defined by (2.1), because it cannot be described by either a fixed or signal dependent kernel.

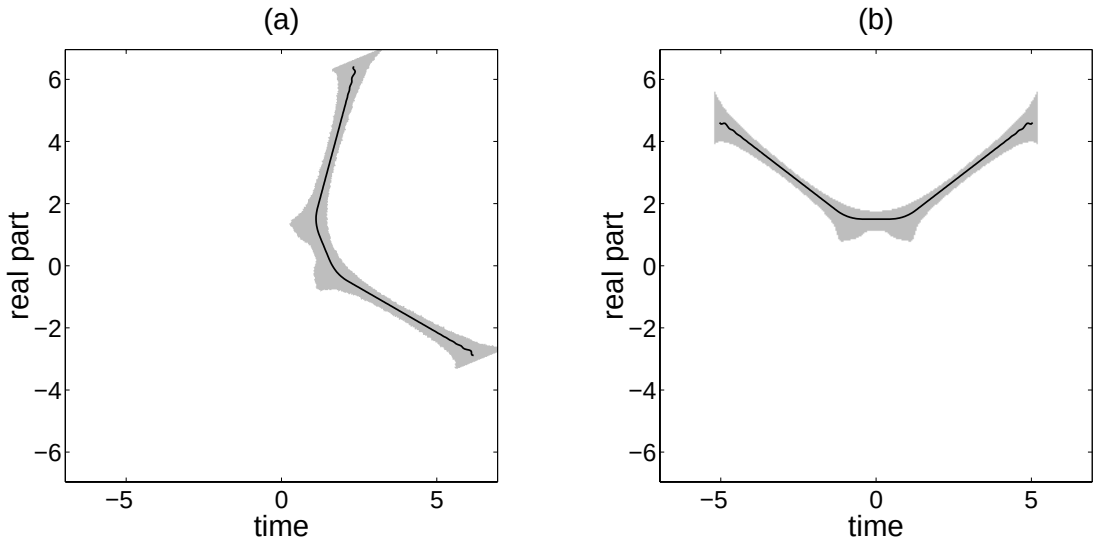

Figure 5.1: (a)–(b) the spines of the signals $x(t)$ and $x_a(t)$ given in Fig. 5.2 plotted on the support of their auto–term WDs, respectively. Although the spine in (a) is a multi–valued function of time, the spine corresponding to the rotated support becomes a single–valued function of time as shown in (b).

Fractional domain warping is the generalization of the time domain warping to fractional domains [48], [93]. The warped fractional Fourier transform of a signal $x(t)$ is obtained by replacing the time-dependence of its FrFT with a warping function $\zeta(t)$. Thus, if $x(t)$ is the time domain signal with the a^{th} order FrFT $x_a(t)$, $a \in \mathbb{R}$, and $\zeta(t)$ is the warping function, then the warped FrFT of the signal is computed by the following equations

$$x_a(t) := \{\mathcal{F}^a\, x\}(t) \triangleq \int K_a(t,t')x(t')\,\mathrm{d}t' \tag{5.2a}$$

$$x_{a,\zeta}(t) := x_a(\zeta(t)) \ , \tag{5.2b}$$

where the kernel of the FrFT $K_a(t,t')$ is given in Section 2.2 and $\zeta(t)$ is the warping function associated with $x_a(t)$. For each analyzed signal component, the warping function is determined based on spine of the component, which is defined as the center of mass along the time–frequency domain support of the signal component. To compute the warping function $\zeta(t)$, a single valued spine is needed as formulated in Section 5.3. If the support of the signal component $x(t)$ is as shown in Fig. 5.1 (a), its spine is a multiple valued function of time. However if the support is rotated as shown in Fig. 5.1 (b), the spine corresponding to the rotated support becomes a single valued function of time and is identical with the instantaneous frequency. Since, these time–frequency domain rotations are made possible by fractional Fourier transformation as illustrated in Fig. 5.2, fractional Fourier transformation extends the

class of signals which may benefit from the warping transformation.

In the following sections, we introduce the use of fractional domain warping transformation to time–frequency analysis of signals with localized time–frequency supports. For the sake of clarity, first we present a simplified form of the TFCA for the analysis of *mono–component* signals, then extend it to *multi–component* case in Chapter 6.

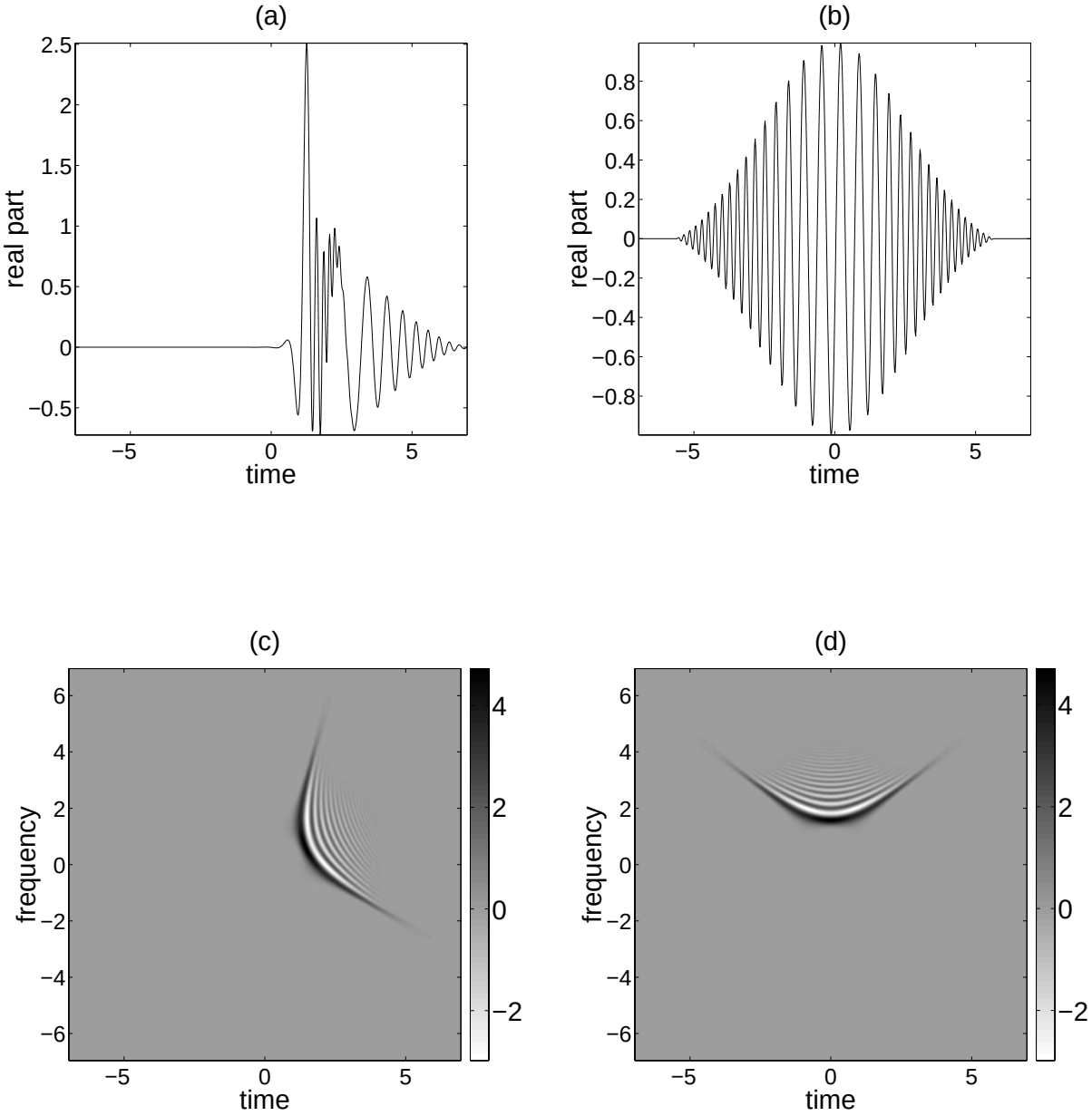

Figure 5.2: (a) A signal $x(t)$, (b) its $a = (-0.75)^{\text{th}}$ order FrFT $x_a(t)$ and (c)–(d) the WDs of the signals $x(t)$ and its FrFT. The Wigner plots illustrate the rotation property of the fractional Fourier transform on time–frequency plane: (right) The WD of $x_a(t)$ is the same as (left) the WD of the $x(t)$ rotated by $-a\pi/2 = 3\pi/8$ radians in the counter–clock wise direction.

5.3 Analysis of *Mono–Component* Signals by TFCA

The analysis of mono–component signals by TFCA starts with estimating support of the signal in the time–frequency plane. To this end either the conventional short–time Fourier transform (STFT) or one of its enhanced versions can be utilized [94], [95]. Since the STFT is a linear transformation, unlike bilinear time–frequency distributions, it does not pass cross–term interference. Although it has a lower resolution compared to bilinear time–frequency distributions, its use is satisfactory in this application, since TFCA requires only an estimate of the signal's support in the time–frequency plane. In Fig. 5.3(a), the magnitude of the STFT of the signal shown in Fig. 5.2(a) is given, where $h(t) = e^{-\pi t^2}$ is used as the window function in STFT computation. Then, by using the watershed segmentation algorithm [3], the support of the STFT is computed automatically as shown in Fig. 5.3(b).

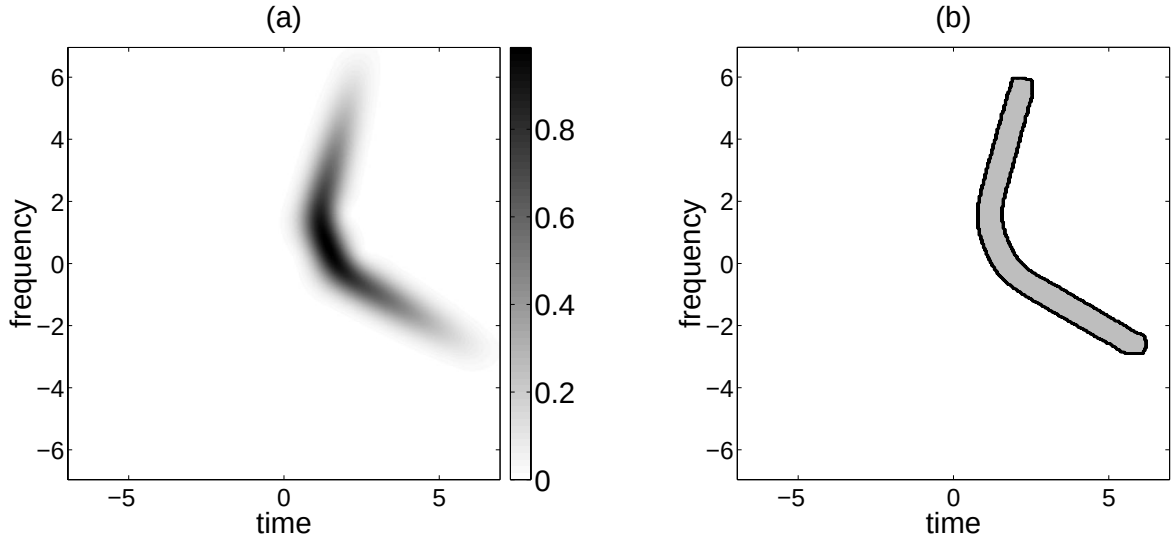

Figure 5.3: (a) The short–time Fourier transform $STFT_x(t, f)$ of the signal $x(t)$ given in Fig. 5.2(a), and (b) support of the STFT computed by using watershed segmentation algorithm [3].

In the second stage of the TFCA, the order a of the FrFT is chosen such that after $a\pi/2$ radians rotation of the time–frequency support of $x(t)$ in the clock–wise direction, spine becomes a single valued function of time. For this example with $a = -0.75$ chosen, the rotated support of $x(t)$ has a single valued spine as shown in Fig. 5.1(b). Actually, any a in the interval of $[-0.50, \ -1.00]$ could have been reliably used for this purpose.

In the third stage of the TFCA, the spine of the signal $x_a(t)$ is estimated. Since after

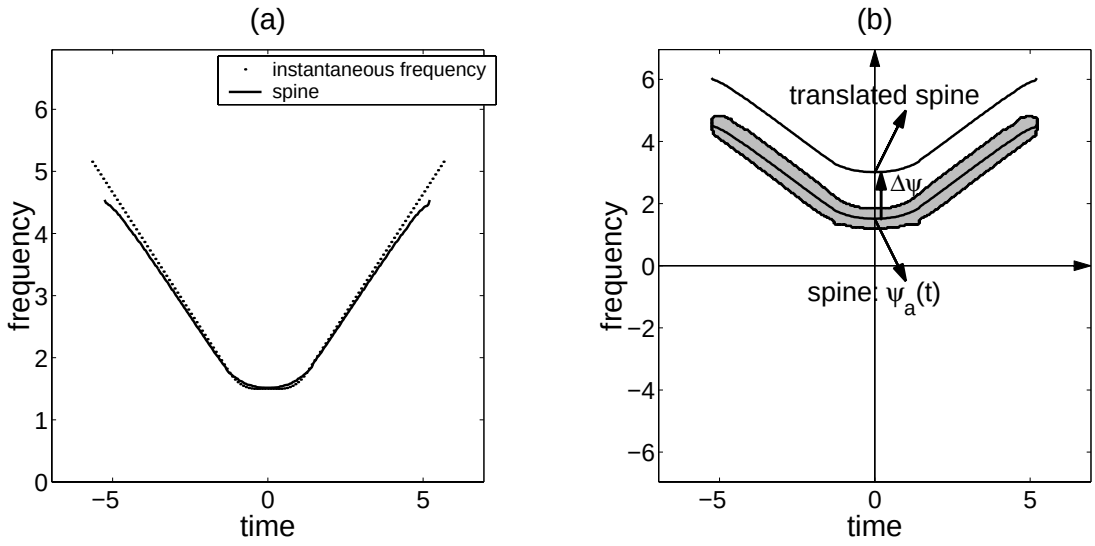

Figure 5.4: (a) The estimated spine $\psi_a(t)$ overlaid with the actual instantaneous frequency of the fractional Fourier transformed signal $x_a(t)$, (b) spine $\psi_a(t)$ of $x_a(t)$ shown on the support of its STFT.

the rotation, the spine of $x_a(t)$ becomes a single valued function of time, an instantaneous frequency estimation algorithm [24], [71], [94], [96], [97] can be used to determine the spine. In this thesis the spine is obtained by

$$\psi_a(t) = \frac{\int f|STFT_{x_a}(t,f)|^2 \,\mathrm{d}f}{\int |STFT_{x_a}(t,f)|^2 \,\mathrm{d}f} \quad , \tag{5.3}$$

where the magnitude squared STFT in (5.3) is called as spectrogram, which is a smoothed bilinear t–f distribution [24]. The close fit of the estimated spine by using this estimator and the actual instantaneous frequency is shown in Fig. 5.4(a). The estimated spine is also shown on the time–support of the STFT in Fig. 5.4(b).

After identification of the spine, the inverse of the warping function is found by integration. When the time domain support of $\psi_a(t)$ is $t_1 \leq t \leq t_N$, the inverse of the warping function is computed by

$$\Gamma(t) = \int_{t_1}^{t} \psi_a(t') \,\mathrm{d}t' \ , \ t_1 \leq t \leq t_N \tag{5.4}$$

$$\zeta^{-1}(t) = \Gamma(t)/f_{\psi_a} + t_1 \ , \ t_1 \leq t \leq t_N \ , \tag{5.5}$$

where f_{ψ_a} is the mean of the spine

$$f_{\psi_a} = \int_{t_1}^{t_N} \psi_a(t') \,\mathrm{d}t' \ . \tag{5.6}$$

With these definitions, the warping function $\zeta(t)$ becomes

$$\zeta(t) = \Gamma^{-1}(f_{\psi_a}(t - t_1)) \ , \quad t_1 \leq t \leq t_N \ . \tag{5.7}$$

If the spine $\psi_a(t)$ is a strictly positive function of time, $\Gamma(t)$ defined in (5.4) is a monotonically increasing function of time. Therefore, its inverse given in (5.7) exists and it is unique. Otherwise, we work with the frequency modulated signal $x_a^{\delta_f}(t) \triangleq x_a(t)e^{\jmath 2\pi t\delta_f}$, where δ_f is chosen such that the spine $\psi_a^{\delta_f}(t) \triangleq \psi_a(t) + \delta_f$ of $x_a^{\delta_f}(t)$ is a strictly positive function of time. Hence, for clarity of the presentation, we assume that $\psi_a(t)$ is a strictly positive function of time. As an illustration, the effect of the warping operation on the synthetic signal given in Fig. 5.2(a) is shown in Fig. 5.5(a). In this example, the warped signal $x_{a,\zeta}(t)$ is computed by using (5.2) with $a = -0.75$ and $\delta_f = 0$.

In digital implementation of the fractional domain warping transformation, uniformly spaced samples $x_{a,\zeta}(kT)$, $k \in \mathbb{Z}$, of $x_{a,\zeta}(t)$ are to be computed from the available uniformly spaced samples $x(kT)$ of $x(t)$, where T is the sampling interval. This can be done by using the fast FrFT computation algorithm [85] in (5.2a) and by using an interpolation algorithm in (5.2b). A multitude of interpolation algorithms exist for this purpose. In this thesis the spline interpolator is preferred for its simplicity [98].

After the warping operation, time–frequency support of the signal $x_{a,\zeta}(t)$ is localized around the line segment (λ, f_{ψ_a}), $t_1 \leq \lambda \leq t_N$, in the time–frequency plane. Thus, by using the warping operation the signal component with non–convex time–frequency support is transformed to a component with convex support in the time–frequency plane. Since $x_{a,\zeta}(t)$ is a mono–component signal with a convex time–frequency support, the simplified form of the TFCA given in Chapter 4 provides a high resolution time–frequency representation with negligible inner interference term in the warped fractional domain. In the following, we will detail how the time–frequency representation will be obtained from the smoothed Wigner distribution of the warped signal in a^{th} fractional domain. A summary of the steps is as follows.

To obtain, the time–frequency representation of the mono–component signal, the smoothed Wigner distribution of the warped signal will be used to obtain a high resolution time–frequency representation of the signal in the a^{th} fractional domain. Then, this fractional domain representation has to be rotated back to obtain the desired time–frequency representation. In the rest of this section, these steps are presented in detail.

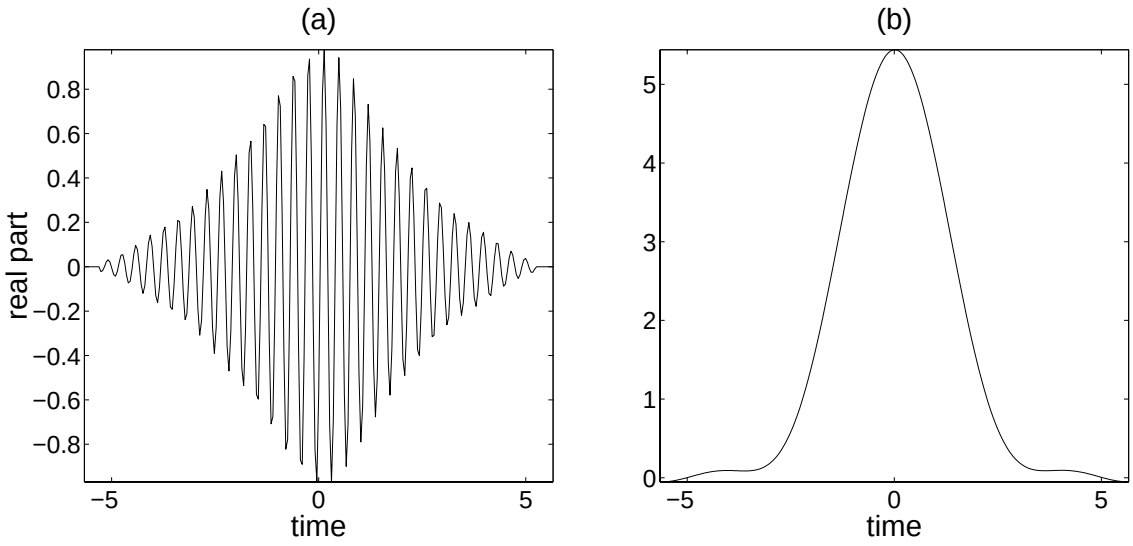

Figure 5.5: (a) The fractional domain warped version $x_{(-0.75,\zeta)}(t)$ of the signal $x(t)$ given in Fig. 5.2 (a), and (b) the corresponding smoothed WD slice $\mathcal{H}_{x_{(-0.75,\zeta)}}(t, f_\psi)$ of $x_{(-0.75,\zeta)}(t)$. The TFCA uses this smoothed WD slice to compute the time–frequency slice $\mathcal{H}_{x_{(-0.75)}}(t, f)$ of $x_{(-0.75)}(t)$ which lies on the spine $\psi_a(t)$ shown in Fig. 5.4(b).

Following the computation of the smoothed WD slice of the warped signal on the line segment (λ, f_{ψ_a}), $t_1 \leq \lambda \leq t_N$, as illustrated in Fig. 5.5(b), the time–frequency slice of the distribution $\mathcal{H}_{x_a}(t, f)$ which lies on the spine $\psi_a(t)$ is found as

$$\mathcal{H}_{x_a}(\zeta(\lambda), \psi_a(\zeta(\lambda))) = SW_{x_{a,\zeta}}(\lambda, f_{\psi_a}) \ , \ t_1 \leq \lambda \leq t_N \ , \tag{5.8}$$

where the smoothed WD slice $SW(x_{a,\zeta}(\lambda, f_{\psi_a})$ is computed by using the simplified version of the TFCA given in Chapter 4. In digital implementation, samples of the smoothed WD slice $SW_{x_{a,\zeta}}(t, f_{\psi_a})$, $t_1 \leq \lambda \leq t_N$, can be computed by using the fast computation algorithm given in [49].

Samples of $\mathcal{H}_{x_a}(t, f)$ lying on translated spines can also be computed efficiently as follows. By imposing the frequency shifting property on the TFD of $x_a(t)$, we require that when $y_a(t) = x_a(t)e^{j2\pi\Delta_{\psi_a}t}$ is a linearly frequency modulated version of $x_a(t)$, the following relation exists between the time–frequency distributions of these signals:

$$\mathcal{H}_{x_a}(t, f + \Delta_{\psi_a}) = \mathcal{H}_{y_a}(t, f) \ . \tag{5.9}$$

Hence, time–frequency distribution slice of $\mathcal{H}_{y_a}(t, f)$ which lies on the spine $\psi_a(t)$ shown in Fig. 5.4(b) is the same as the time–frequency distribution slice of $\mathcal{H}_{x_a}(t, f)$ which lies on the

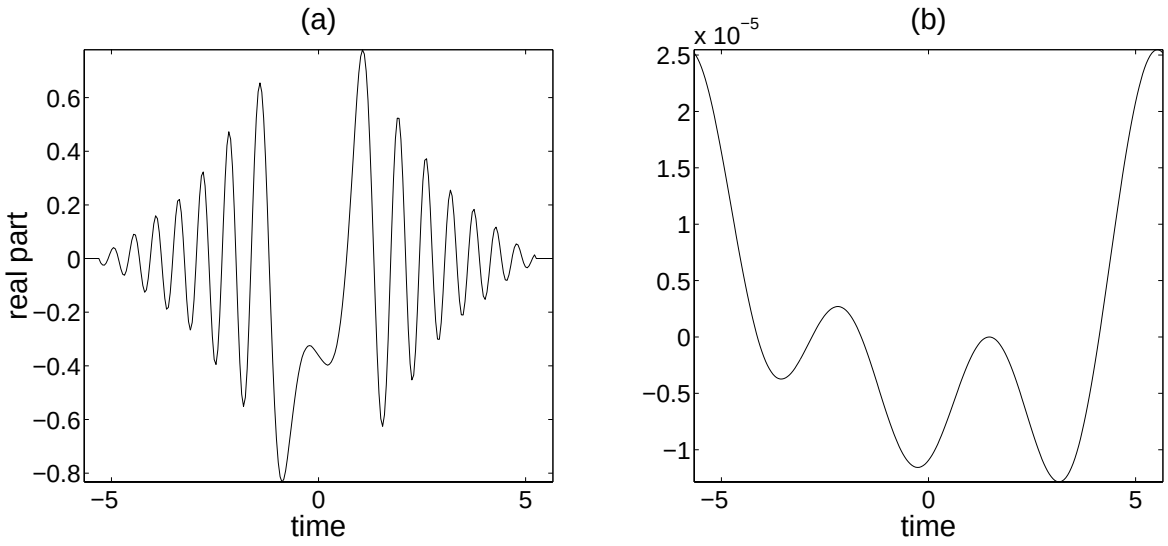

Figure 5.6: (a) The warped version $y_{(-0.75,\zeta)}(t)$ of the signal $y_{(-0.75)}(t) = x_{(-0.75)}(t)e^{j2\pi\Delta_\psi t}$ where $x(t)$ is the same synthetic signal used in Fig. 5.5 and (b) the corresponding smoothed WD slice $\mathcal{H}_{y_{(-0.75,\zeta)}}(t, f_\psi)$ of $y_{(-0.75,\zeta)}(t)$. TFCA uses this smoothed WD slice to compute the time–frequency slice $\mathcal{H}_{x_{(-0.75)}}(t, f)$ of $x_{(-0.75,\zeta)}(t)$ which lies on the translated spine shown in Fig. 5.4(b).

translated spine shown in the same figure:

$$\mathcal{H}_{x_a}(t, \psi_a(t) + \Delta_{\psi_a}) = \mathcal{H}_{y_a}(t, \psi_a(t)) \ . \tag{5.10}$$

Therefore, by using (5.10) and the relation given in (5.8) with $x(t)$ replaced by $y(t)$, the time–frequency distribution slice of $\mathcal{H}_{x_a}(t, f)$, which lies on the translated spine shown in Fig. 5.4(b) is given as the smoothed WD slice of the warped signal $y_{a,\zeta}(t)$ on the line segment (λ, f_{ψ_a}), $t_1 \leq \lambda \leq t_N$:

$$\begin{aligned} \mathcal{H}_{x_a}(\zeta(\lambda), \psi_a(\zeta(\lambda)) + \Delta_{\psi_a}) &= \mathcal{H}_{y_a}(\zeta(\lambda), \psi_a(\zeta(\lambda))) \\ &= SW_{y_{a,\zeta}}(\lambda, f_{\psi_a}) \ , \ t_1 \leq \lambda \leq t_N \ . \end{aligned} \tag{5.11}$$

For instance, for the particular value of Δ_{ψ_a} shown in Fig. 5.4(b), the warped signal $y_{a,\zeta}(t)$ and its Wigner distribution slice computed by using the fast computation algorithm given in [49] are shown in Fig. 5.6(a)-(b), respectively.

In practice, the warped form of the signal $y_a(t)$ is straightforward to compute, since $y_{a,\zeta}(t) = x_{a,\zeta}(t)e^{j2\pi\Delta_{\psi_a}\zeta(t)}$. Thus in the digital implementation, interpolation of the samples $x_a(\zeta(kT))$ from the uniformly spaced samples $x_a(kT)$ should be done only once. For any value of Δ_{ψ_a} the above relation between the warped signals $x_{a,\zeta}(t)$ and $y_{a,\zeta}(t)$ should be used.

In TFCA, the relation given in (5.11) is used to compute the time–frequency distribution slice of $\mathcal{H}_{x_a}(t,f)$ on a curve which is parameterized as $(t(\lambda), f(\lambda)) = (\zeta(\lambda), \psi_a(\zeta(\lambda)) + \Delta\psi_a)$. Hence, for each value of Δ_{ψ_a} the algorithm derived above gives the samples of a different slice of the time–frequency distribution of $x_a(t)$. Thus, by using different values for Δ_{ψ_a}, the TFCA can compute the TFD $x_a(t)$ on a desired region of the time–frequency plane. In the simulated example, by using the mapping rule (5.11) for a set of Δ_{ψ_a} values, TFCA provided a very sharp t–f description of the signal $x_a(t)$ as shown in Fig. 5.7(a).

Finally, to remove the rotation effect induced by the fractional Fourier transformation, computed slices of $\mathcal{H}_{x_a}(t,f)$ are rotated back by $a\pi/2$ radians in the counter clock wise direction. The rotated slices of the time–frequency distribution $\mathcal{H}_x(t,f)$ of $x(t)$ are obtained as

$$\mathcal{H}_x(t_r(\lambda), f_r(\lambda)) = \mathcal{H}_{x_a}(\zeta(\lambda), \psi_a(\zeta(\lambda)) + \Delta_{\psi_a}) \ , \ t_1 \leq \lambda \leq t_N \ , \tag{5.12}$$

where $t_r(\lambda)$ and $f_r(\lambda)$ are given by:

$$\begin{aligned} t_r(\lambda) &= \zeta(\lambda)\cos(a\pi/2) - (\psi_a(\zeta(\lambda)) + \Delta_{\psi_a})\sin(a\pi/2) \\ f_r(\lambda) &= \zeta(\lambda)\sin(a\pi/2) + (\psi_a(\zeta(\lambda)) + \Delta_{\psi_a})\cos(a\pi/2) \ , \ t_1 \leq \lambda \leq t_N \ . \end{aligned} \tag{5.13}$$

The resultant TFD of $x(t)$ obtained by rotating the TFD of $x_a(t)$ given in Fig. 5.7(a) is shown in Fig. 5.7(b).

5.4 Conclusions

A simplified version of the TFCA is developed to obtain very high resolution distribution of mono–component signals with convex or non–convex time–frequency supports. By utilizing a novel fractional domain warping concept and the algorithms given in Chapters 3–4, the simplified version of the TFCA significantly suppresses the inner interference terms of the signal components and produces a very good time–frequency description of them. The performance of the new time–frequency distribution is illustrated on a simulation example.

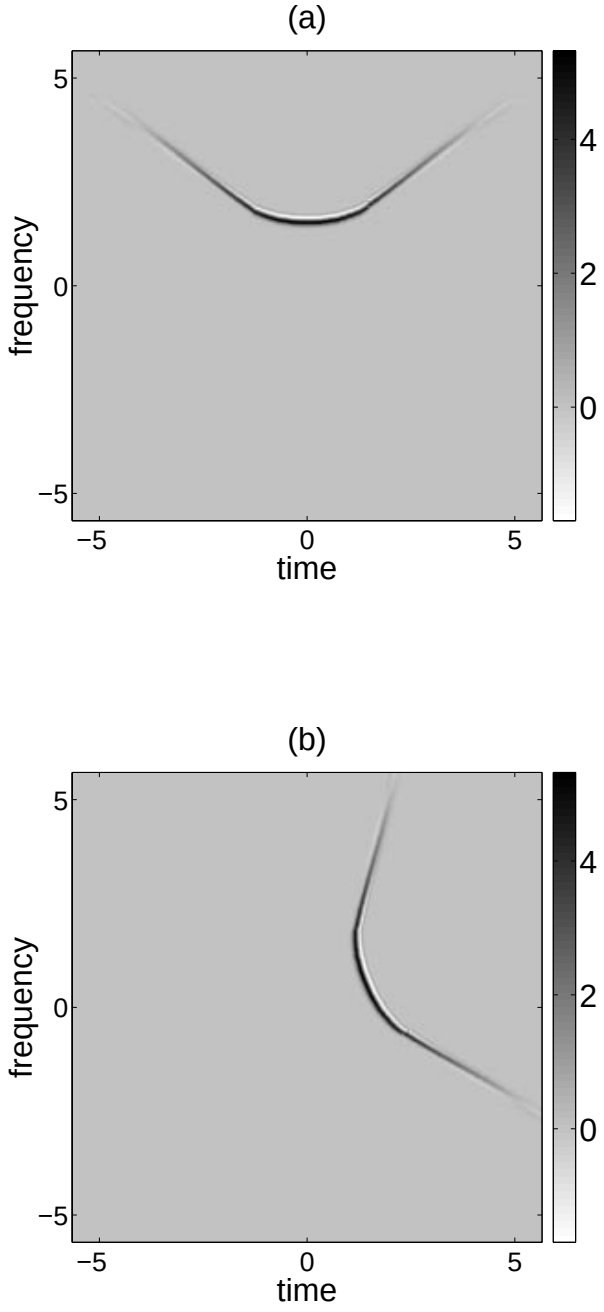

Figure 5.7: (a)–(b) The time–frequency distributions of $x_{(-0.75)}(t)$ and $x(t)$, respectively, which are obtained by using the TFCA. Note that after computing the time–frequency distribution $\mathcal{H}_{x_{(-0.75)}}(t, f)$ of $x_{(-0.75)}(t)$, the TFCA provides the time–frequency distribution $\mathcal{H}_x(t, f)$ of $x(t)$ by rotating $\mathcal{H}_{x_{(-0.75)}}(t, f)$ by an amount proportional to the order, $a = -0.75$, of the fractional Fourier transformation.

Chapter 6

The Full Version of the TFCA

6.1 Introduction

In the previous chapters, we presented the limited versions of the TFCA for some special class of signals. The proposed fast computation algorithms efficiently remove the inner and outer interference terms of that limited class of signals in the time–frequency plane. In this chapter, we present the full version of the TFCA.

In the full version of TFCA, the analysis of a multi–component signal $x(t) = \sum_{i=1}^{m} s^i(t)$ with m components $s^i(t)$ starts by identification of the supports of the individual components. To this purpose, we propose to use an image segmentation algorithm on the short–time Fourier transform of the composite signal. Then, by using the support information on one of these components, for instance $s^1(t)$, the TFCA maps the composite signal $x(t)$ into an appropriate warped fractional domain, where the chosen component $s^1(t)$ with a possibly complicated cross–term structure in the original time–frequency plane has an approximately convex time–frequency support in the warped domain. In the second stage of the processing, the TFCA uses a practical and highly efficient time–frequency domain incision algorithm to extract the analyzed signal component $s^1(t)$ in the warped fractional domain. Then by efficiently smoothing WD slices of the extracted signal component, the TFCA provides the distribution of the extracted component in the warped fractional domain. Finally by mapping the computed distribution back into the original time–frequency plane, the TFCA provides a high resolution

distribution for that component with significantly reduced interference terms.

After completing its analysis on a chosen signal component, the TFCA proceeds by subtracting the estimated component $s^1(t)$ from the composite signal $x(t)$. Since the utilized incision algorithm provides highly accurate estimates, the computed residual signal is composed of essentially $m-1$ components $s^i(t)$, $2 \leq i \leq m$. Thus by iterating the time–frequency analysis and incision stages each time on a reduced complexity residual signal, the TFCA provides the time–frequency distributions of the individual signal components. In the final stage of processing, the TFCA computes the time–frequency distribution of the composite signal by fusing the computed distributions of the individual signal components.

The use of a component extraction algorithm as part of the TFCA brings the following benefits:

- Computational efficiency increases, since usually extracted components have shorter time supports.
- The quality of the resultant distribution improves, since by incision large amount of noise can be removed.
- The identification of the supports of the remaining components simplifies, because the extraction of a component s^i in an N–component signal also removes the $N-1$ cross–terms of the form $2\mathfrak{Re}\{W_{s^i s^j}(t,f)\}$, $i<j$, in the time–frequency domain.

Since these expected benefits are dependent on the performance of the component extraction algorithm, we propose to use an efficient but highly accurate fractional domain incision technique developed in this chapter.

The organization of this chapter is as follows. In Section 6.2 we give the mathematical details of the FDI algorithm. Then, in Section 6.3 we present the full version of TFCA on a simulated example and compare the performance of TFCA with some well known methods on synthetic and real data sets.

6.2 Fractional Domain Incision Algorithm: An Efficient Algorithm for Extraction of Signal Components with Convex Time–Frequency Supports

Time–frequency based extraction of the individual signal components of a given multi–component signal can be conducted in two stages. In the first stage detection and identification of the individual signal components is performed on the time–frequency plane. Then, the signal components are estimated based on the obtained time–frequency information on them. In the following subsections both stages of the component extraction problem are fully analyzed on a simulated example. To convey the ideas clearly, noise–free signals are used in the simulation example. The effect of noise to the performance of TFCA will be investigated in Section 6.3.

6.2.1 Detection and Identification of Signal Supports In the Time–Frequency Plane

The search for signal components which have compact time–frequency supports typically starts with the careful examination of the time–frequency distribution of the composite signal. The Wigner distribution is the most commonly used time–frequency analysis tool which provides the highest resolution time–frequency characterization of chirp–like signals. However, because of its bilinear nature, the supports of the actual signal components may not be visible in the presence of cross–terms of the Wigner distribution. For instance, if the signal $s(t)$ is composed of m signal components, $s_i(t)$, $1 \leq i \leq m$, then by using (2.2) and (2.3) the corresponding Wigner distribution can be written as:

$$\begin{aligned} W_s(t,f) &= \int s(t+t'/2)s^*(t-t'/2)e^{-\jmath 2\pi f t'}\,\mathrm{d}t' \\ &= \int \sum_i s_i(t+t'/2)s_i^*(t-t'/2)e^{-\jmath 2\pi f t'}\,\mathrm{d}t' \\ &= \sum_i W_{s_i}(t,f) + 2\sum_{i<k} \mathfrak{Re}\{W_{s_i s_k}(t,f)\}\ , \end{aligned} \tag{6.1}$$

where the auto–Wigner distributions corresponding to m individual signal components are accompanied by $m(m-1)/2$ cross–Wigner distributions [6]. As shown in Fig. 6.1(b), the cross–Wigner terms may partially or totally overlap with the auto–Wigner terms making it very difficult if not impossible to detect and identify the time–frequency supports of the individual signal components.

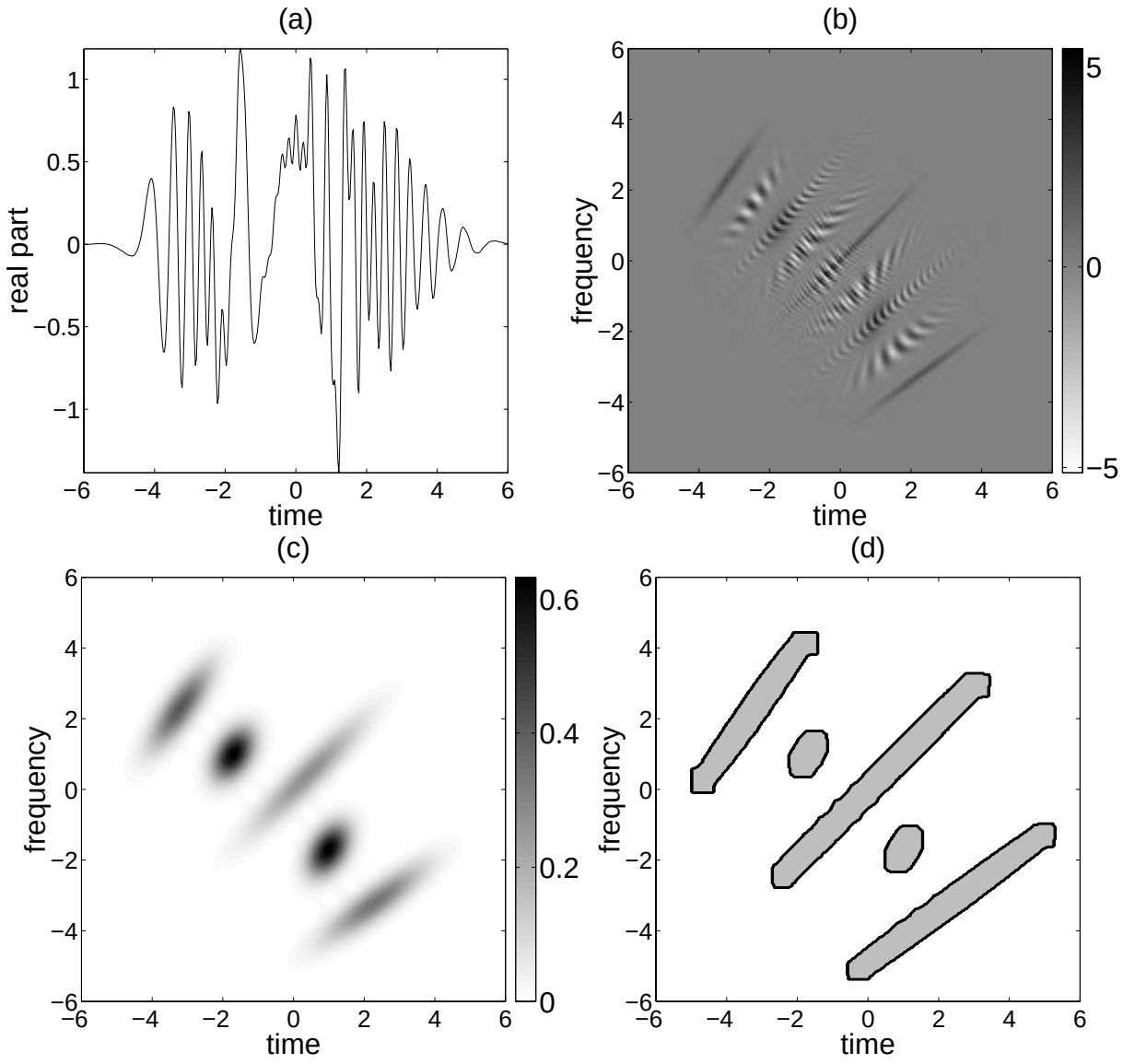

Figure 6.1: Illustration of support identification in time–frequency plane: (a) The time domain representation of a multi–component signal $s(t)$, which is composed of 5 linear FM signals, (b) and (c) the Wigner distribution and short–time Fourier transform of $s(t)$, respectively, (d) time–frequency supports of components computed by using the watershed segmentation algorithm on the STFT of $s(t)$.

In this thesis, STFT is used to identify the time–frequency supports of individual components. Although it has a lower resolution than the WD as shown in Fig. 6.1(c), being a *linear* distribution, it doesn't contain troublesome interference terms. In other words, the STFT of a composite signal is the sum of the STFTs of the individual components of the composite signal. In this thesis, we propose to detect the time–frequency supports of the signal components *automatically*, by using a segmentation algorithm on the computed STFT. In Fig. 6.1(d), the result obtained by using the watershed segmentation algorithm [3] on the computed STFT is given. As shown in this figure, the supports of the individual components can be detected well enough by using the watershed segmentation algorithm.

6.2.2 Component Estimation by Fractional Domain Incision

In the second stage of processing, the obtained information on the supports of the individual signal components is used to design proper time–frequency incision techniques to extract the components directly from the signal. To demonstrate the required processing for the signal component extraction, consider the supports of auto–terms of the Wigner distribution of a composite signal as shown in Fig. 6.2. In order to extract the signal component which is localized at the center of the time–frequency plane, a time–frequency incision around this component should be performed. Among many alternatives, the simplest incision can be performed by first applying a frequency domain mask $H_1(f)$ to $S(f)$ whose support is the same as the frequency axis projection of the signal component. Then, to the result a time–domain mask $h_2(t)$, whose support is the projection of the signal component on the time–axis, can be applied to approximate the signal component. This way, the estimated signal component will have its time–frequency support approximately limited into the dashed–box around the desired signal component. Formally, the component estimate is obtained by:

$$\hat{s}_i(t) = h_2(t)[h_1(t) * s(t)] \approx s_i(t) \ . \tag{6.2}$$

In a more general case, if the supports of the auto–components in the time–frequency plane are as shown in Fig. 6.3, then it is not possible to extract $s_i(t)$ from $s(t)$, by successive maskings in frequency and time domains. Because in this case there does not exist a rectangular region in the time–frequency plane, which contains only the support of the i^{th}

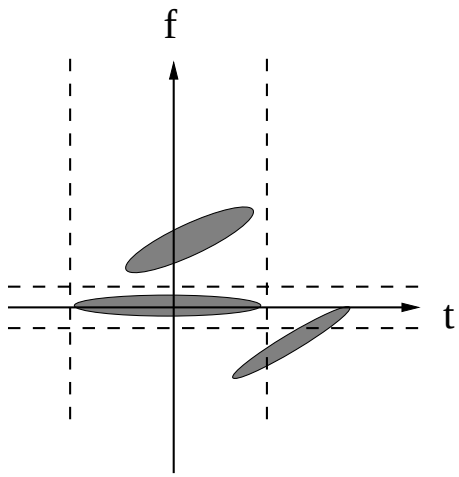

Figure 6.2: The extraction of the component centered at the origin of the time–frequency plane by using frequency and time domain masks.

auto–component but not the others. However, a viable solution in this case is first to translate the origin of the time–frequency plane to approximate center (t_i, f_i) of the i^{th} auto–component as shown in Fig. 6.3. The required translation can be performed as:

$$\tilde{s}(t) = s(t + t_i)e^{-\jmath 2\pi t f_i} \quad . \tag{6.3}$$

Note that the i^{th} component of the signal $\tilde{s}(t)$ is $\tilde{s}_i(t) = s_i(t + t_i)e^{-\jmath 2\pi t f_i}$. Then the fractional Fourier transform [99] of this signal is

$$\tilde{s}_{a_i}(t) \equiv \{\mathcal{F}^{a_i}\,\tilde{s}\}(t) \triangleq \int K_{a_i}(t, t')\tilde{s}(t')\,\mathrm{d}t' \quad , \tag{6.4}$$

where $a_i = 2\phi/\pi$ is the order of the FrFT and $K_{a_i}(t, t')$ is the kernel of the transformation given in (2.8). Since the WD of the a_i^{th} order FrFT of a signal is the same as the WD of the original signal rotated by angle of $a_i\pi/2$ in the clock–wise direction [88], [99], the WD of $\tilde{s}_{a_i}(t)$ is aligned with one of the axis as shown in Fig. 6.3(c). Thus after the elementary operations of translation and rotation in the time–frequency plane, the WD of $\tilde{s}_{i,a_i}(t)$ fits into a compact rectangular region as shown in Fig. 6.3(c). Therefore, as in Fig. 6.2, the i^{th} component of $s(t)$ can be extracted in the transform domain by successive maskings as:

$$\hat{\tilde{s}}_{i,a_i}(t) = h_2(t)[h_1(t) * \tilde{s}_{a_i}(t)] \quad , \tag{6.5}$$

where $h_2(t)$ is the time–domain mask and $h_1(t)$ is the inverse Fourier transform of the frequency domain mask $H_1(f)$. After obtaining an estimate for $\tilde{s}_{i,a_i}(t)$, an estimate of $s_i(t)$

can be easily computed by reversing the operations of translation and rotation in the time–frequency plane:

$$\hat{\tilde{s}}_i(t) = \mathcal{F}^{-a_i}[\hat{\tilde{s}}_{i,a_i}(t)] \tag{6.6}$$

$$\hat{s}_i(t) = \hat{\tilde{s}}_i(t - t_i)e^{\jmath 2\pi(t-t_i)f_i} \ . \tag{6.7}$$

In practice the required fractional Fourier transform can be directly carried on the given

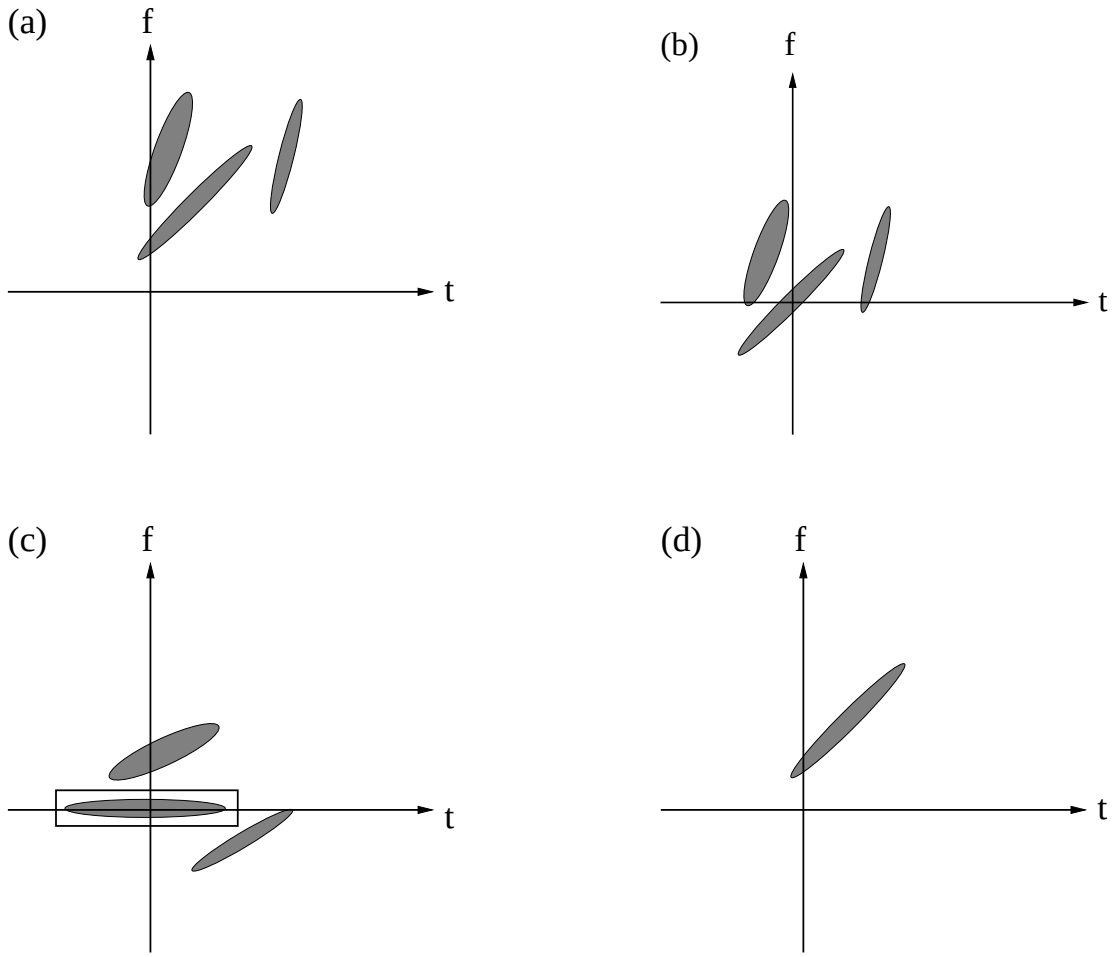

Figure 6.3: An illustration showing the steps of fractional domain incision algorithm: (a) shows the supports of the auto–terms in the WD of $s(t)$, (b) shows the corresponding supports for the time and frequency translated signal $\tilde{s}(t) = s(t + t_i)e^{-\jmath 2\pi f_i t}$. After computing the fractional Fourier transformation of $\tilde{s}(t)$, the support of the middle component in $\tilde{s}_{a_i}(t) = \mathcal{F}^{a_i}[\tilde{s}(t)]$ is aligned with the time–axis as shown in (c). Thus, as discussed in Section 6.2.2, this component can be extracted by frequency and time domain masking operations, respectively. After extraction of the component, the steps of fractional Fourier transformation, time and frequency translation operations are reverted to obtain the time–domain representation of the extracted component. The time–frequency support of the extracted component after these operations is shown in (d).

Nyquist rate samples of the composite signal $s(t)$ by using the algorithm given in [85] and summarized in Appendix B.1. As shown in [85], the complexity of the fractional Fourier transform is the same as FFT. Therefore, the overall complexity of the proposed signal component extraction algorithm is $O(N \log N)$ for a component whose time domain support is of approximately N samples in duration.

The required incision in the more general case shown in Fig. 6.3 can also be performed by using fractional Fourier domain filtering techniques given in [57], [100], [101]. However, the proposed techniques in [57], [100], [101] are for noise suppression. Therefore, there is a need for improvement in these techniques to suppress both the noise and the other signal components.

6.2.3 Simulation of the Fractional Domain Incision Algorithm

In this section we investigate the performance of the fractional domain incision algorithm by conducting computer simulations on the synthetic signal given in Fig. 6.1 (a). The corresponding Wigner distribution shown in Fig. 6.1(b) is very much cluttered with the cross–terms. Because of the significant overlaps between the cross and auto terms, it is rather difficult to identify supports of auto–terms given in Fig. 6.1(b). However, as shown in Fig. 6.1(c)–(d), by using the first stage of the processing supports of the individual signal components can be identified accurately.

To illustrate the performance of the second stage of processing, we present results on extracting two of the chirp components of the composite signal shown in Fig. 6.1. The estimate of the long chirp component which is located at the center of the t–f plane in Fig. 6.1 is given in Fig. 6.4 (a). This result is obtained by performing time–frequency domain incision on a rotated time–frequency plane obtained by using fractional Fourier transformation of order 0.5 corresponding to $\pi/4$ radians of rotation. The error in the estimated signal component is shown in Fig. 6.4(b). As seen from this figure, the extracted signal component is a very close approximation of the original signal component with a normalized error of $E_i = 1.3 \times 10^{-3}$ which is defined as:

$$E_i = \frac{||\boldsymbol{x}_i - \hat{\boldsymbol{x}}_i||}{||\boldsymbol{x}_i||} \tag{6.8}$$

where $\boldsymbol{x}_i$ and $\hat{\boldsymbol{x}}_i$ are the actual and estimated signal components in vector notation.

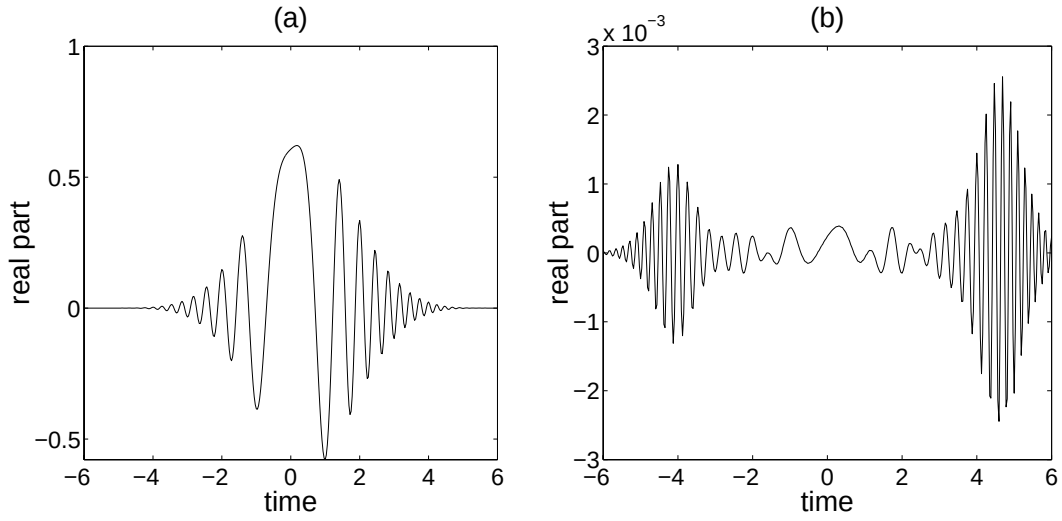

Figure 6.4: Performance of the fractional domain incision algorithm: (a) The estimate of the long chirp component in Fig. 6.1(b) which is located about the origin of the time–frequency plane and (b) the difference of the estimate from the actual signal component.

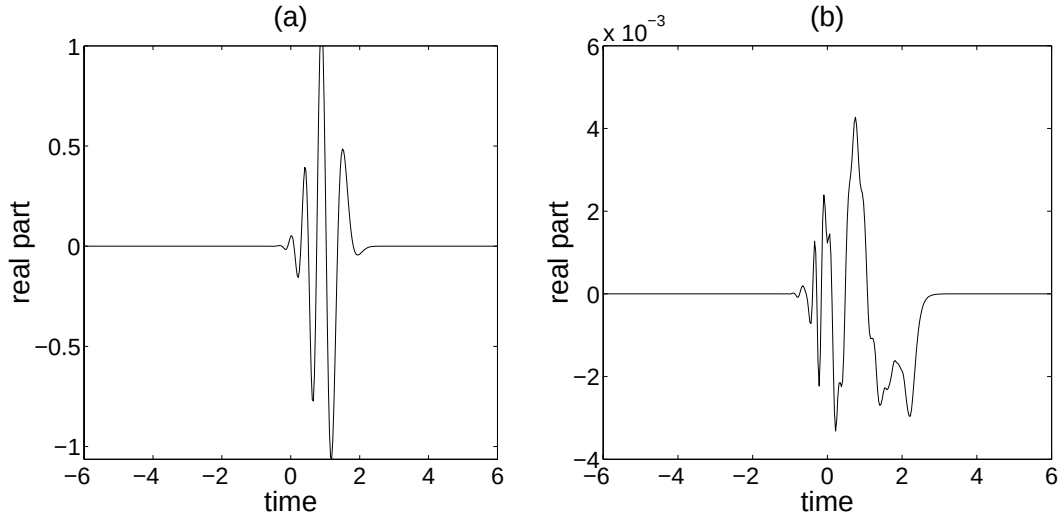

Figure 6.5: Performance of the fractional domain incision algorithm: (a) The estimate of the short chirp component in Fig. 6.1(b) whose time-frequency center lies to the right of the origin and (b) the difference of the estimate from the actual signal component.

The estimate of the shorter chirp component which is located just to the right of the longest chirp component in Fig. 6.1 is shown in Fig. 6.5(a). This result is obtained by first translating the origin of the time–frequency plane to the center of the chirp component. Then the time–frequency domain incision over the estimated support of the signal component is performed on a rotated time–frequency plane obtained by using fractional Fourier transformation of order 0.5 corresponding to $\pi/4$ radians of rotation. The difference plot of the estimated and actual

signal component is shown in Fig. 6.5(b) to illustrate the accuracy of the algorithm. As seen from this figure, the extracted signal component is a very close approximation of the original signal component with a normalized error of $E_i = 2.5 \times 10^{-3}$.

6.3 Analysis of *Multi–Component* Signals by TFCA

In this section, the full version of TFCA is presented. To clearly present this technique, steps of the TFCA is shown on a three–component signal $s(t)$, which is obtained by adding two more components to the mono–component signal analyzed in Section 5.3. To illustrate the effect of noise on TFCA, noise corrupted signal $x(t) = s(t) + w(t)$ is used in the analysis, where samples of w(t) are independent identically distributed circular Gaussian noise. The mean signal energy to noise power spectral density ratio is chosen as 5 dB. The noisy signal $x(t)$ and its Wigner distribution $W_x(t, f)$ are shown in Fig. 6.6(a) and (b), respectively. The WD plot clearly show significant problems of cross–terms. In Fig. 6.7(a) the short time Fourier transform, $STFT_x(t, f)$ of the multi–component signal $x(t)$ is shown. Although STFT has lower resolution then the WD, supports of all components can be detected well enough on computed STFT by using the watershed segmentation algorithm [3] as shown in Fig. 6.7(b).

The first component to be analyzed by TFCA is manually chosen as one of the peripheral components. In the presented example, the component which is located at the top right in Fig. 6.7(b) is chosen as the first component, $s^1(t)$, to be analyzed by TFCA. The appropriate FrFT order a_1 and the spine $\psi_{a_1}(t)$ of the first component $s^1_{a_1}(t)$ in fractional Fourier transform domain are estimated as in mono–component case. However instead of the short–time Fourier transforms of $x(t)$ and $x_{a_1}(t)$, their masked versions $STFT_x^M(t, f) \triangleq STFT_x(t, f)\, M(t, f)$ and $STFT_x^{M_{a_1}}(t, f) \triangleq STFT_{x_{a_1}}(t, f)\, M_{a_1}(t, f)$ are used, where the masks $M(t, f)$ and $M_{a_1}(t, f)$ are indicator functions of the supports of $s^1(t)$ and $s^1_{a_1}(t)$ which are obtained automatically by using watershed segmentation algorithm [3]. In the presented example, a_1 is estimated as -0.75 and the estimate of the spine $\psi_{a_1}(t)$ computed by using the indicator function $M_{a_1}(t, f)$ given in Fig. 6.8(a) is plotted in Fig. 6.8(b) overlaid with the actual spine. The corresponding root mean square estimation error for the spine is 0.102 Hz in this example. Then, the warped FrFT $x_{a_1,\zeta_1}(t)$ is computed, which is shown in Fig. 6.9(a). To obtain the

support of the first warped component, the short time Fourier transform $STFT_{(x_{a_1,\zeta_1})}(t,f)$ of the warped signal, which is shown in Fig. 6.9 (b), is computed. The STFT component with convex support corresponds to the first warped component. Note that in the computation of the STFT, a Gaussian window, $h(t) = e^{-\pi t^2/4}$, is used.

In the second stage of processing, the warped signal component will be extracted. For this purpose various time–frequency processing techniques such as [55], [56], [58–61] can be used. In the following, we will present results based on the time–frequency domain incision technique [56]. The warped signal component can be extracted by using a simple incision technique by first applying a frequency domain mask $H_1(f)$ to $S(f)$ and then applying a time domain mask $h_2(t)$ to the result. The supports of the frequency domain mask and time domain masks are chosen to enclose the support of the first component in $STFT_{(x_{a_1,\zeta_1})}(t,f)$ into a rectangular region as shown with horizontal and vertical dashed lines in Fig. 6.9(b). This way, the estimated signal component will have its time–frequency support approximately limited into the dashed–box around the desired signal component. Formally, the warped component estimate is obtained by:

$$\hat{s}^1_{a_1,\zeta}(t) = h_2(t)[h_1(t) * x_{a_1,\zeta}(t)] \ , \tag{6.9}$$

where $h_2(t)$ is the time–domain mask and $h_1(t)$ is the inverse Fourier transform of the frequency domain mask $H_1(f)$. After obtaining an estimate for $s^1_{a_1,\zeta}(t)$, an estimate of $s^1(t)$ can be easily computed by inverse warping, and inverse fractional Fourier transformation operations, respectively:

$$\hat{s}^1_{a_1}(t) := \hat{s}^1_{a_1,\zeta_1}(\zeta_1^{-1}(t)) \tag{6.10a}$$

$$\hat{s}^1(t) := \{\mathcal{F}^{(-a_1)}\, \hat{s}^1_{a_1}\}(t) \ . \tag{6.10b}$$

In the presented example, the FrFT order is $a_1 = -0.75$. The resultant signal obtained after these operations is shown in Fig. 6.10 (a) overlaid with the actual component $s^1(t)$. The corresponding estimation error shown in Fig. 6.10 (b) indicates the accuracy of the time–frequency domain incision algorithm despite excessive noise. In the signal extraction stage of TFCA, more sophisticated time–varying filtering techniques can be used to extract the warped signal components. If there are no overlapping signal components, the extraction can be performed by using any of the well known techniques. On the other hand, at the incision stage where overlapping components are to be extracted, we propose to use time–frequency

domain signal synthesis techniques such as [59],[60]. A comparative study of using alternative techniques will be presented in a future work.

In practice the required fractional Fourier transform can be directly carried on the given Nyquist rate samples of the composite signal $x(t)$ by using the algorithm given in [85] and summarized in Algorithm 2. As shown in [85], the complexity of the fractional Fourier transform is the same as the FFT. Therefore, the overall complexity of the utilized signal component extraction algorithm is $O(N \log N)$ for a component whose time domain support is of approximately N samples in duration.

After extraction of the first component, the same analysis is repeated on the residual signal $r^1(t) = x(t) - \hat{s}^1(t)$ to estimate the second component and its corresponding TFD. Continuing in this manner, all components of the composite signal are estimated. In Fig. 6.11 and Fig. 6.12 the estimates of the remaining signal components and the corresponding estimation errors are plotted. The estimation errors $e^i(t) = s^i(t) - \hat{s}^i(t)$ given in these figures show the accuracy of the fractional domain incision technique used in TFCA.

At the end of these iterations we have obtained estimates for all three signal components. The final residual, $r^3(t) = x(t) - \sum_{i=1}^{3} \hat{s}^i(t)$, given in Fig. 6.13 (a) shows that after the extraction of the identified signal components, the residual is noise–like. Once the TFCA isolates the individual signal components, their corresponding high resolution time–frequency representations can be obtained as described in Section 5.3 for mono–component signals. Then, the TFCA computes the time–frequency distribution of the composite signal by summing the computed time–frequency distributions of the individual components as shown in Fig. 6.13(b). The computed distribution has a very sharp resolution and has negligible outer or inner interference terms as this figure clearly shows.

Before comparing the performance of TFCA with some well know time–frequency analysis techniques, we note that if the identified support of the warped signal component is free of outer interference terms, then the TFCA can provide a time–frequency distribution of that component without the use of signal extraction. Otherwise, the signal components that has outer interference terms can only be analyzed reliably after the extraction of those signal components causing the interference. Hence, the extraction of signal components is a must in this case. However, TFCA aims not only to provide a time-frequency distribution, but also, to

extract the identified signal components. Therefore, we always make use of signal extraction as part of TFCA.

To assess the performance of TFCA, we compared its performance with some fixed kernel time–frequency distributions and two well known data adaptive techniques: The reassignment method [46] and the optimal radially–gaussian kernel TFD technique [35]. In Fig. 6.14 (a), Fig. 6.15 (a) and Fig. 6.16 (a), the pseudo Wigner distribution (PWD), the smoothed pseudo Wigner distribution (SPWD) and the spectrogram are shown, respectively. The corresponding reassigned distributions, i.e., reassigned PWD, reassigned SPWD and reassigned spectrogram are given in Fig. 6.14 (b), Fig. 6.15 (b) and Fig. 6.16 (b), respectively. These plots show that when the smoothing of the WD is not enough to suppress the cross–terms sufficiently, the reassigned TFD obtained from the corresponding smoothed distribution also includes cross–terms. When the cross–terms are sufficiently suppressed as shown in Fig. 6.16 (a), the windowed chirp signal at the bottom left part of the t–f plane has a line segment like distribution after reassignment as shown in Fig. 6.16 (b), which violates the uncertainty principle. In Fig. 6.17(a)–(b), the results for ORGK time–frequency distribution are given for volume parameter $\alpha = 3$ and $\alpha = 5$, respectively. Although ORGK is able to resolve all three components, there is significant cross–term interference in the obtained TFD. Furthermore, there is a distortion in the auto–term of the component with non–convex t–f support.

To compare the performance of computed time–frequency distributions numerically, we define a normalized fit error associated with any TFD $\Upsilon(t, f)$ as

$$e_{\Upsilon} = ||W_A(t, f) - M_{W_A}(t, f)\, \Upsilon(t, f)||/||W_A(t, f)|| \ , \tag{6.11}$$

and a normalized interference energy defined by

$$E_{\Upsilon} = ||(1 - M_{W_A}(t, f))\, \Upsilon(t, f)||/||W_A(t, f)|| \ , \tag{6.12}$$

where $W_A(t, f)$ is the auto–term WD which is obtained by removing any noise and artifacts including the inner and outer interference terms from the WD, $M_{W_A}(t, f)$ is the indicator function describing the support of the auto–term WD and $||\cdot||$ is the Frobenius norm. Thus, (6.11) gives the fit error between the distribution $\Upsilon(t, f)$ and the auto–term WD $W_A(t, f)$ in the support of the auto–term WD. On the other hand, (6.12) gives the amount of interference energy left in the computed distribution which lies outside the support of the

Distribution	Normalized Fit Error	Normalized Interference Energy
WD	1.064	1.406
TFCA	0.535	0.044
PWD	0.561	13.208
reassigned PWD	1.202	21.965
SPWD	0.736	3.538
reassigned SPWD	1.291	3.734
spectrogram	0.951	7.529
reassigned spectrogram	1.919	24.781
ORGK ($\alpha = 3$)	1.002	0.712
ORGK ($\alpha = 5$)	1.039	0.804

Table 6.1: The normalized fit errors and interference energies associated with the distributions computed in this thesis to obtain the TFD of the three–component signal given in Fig. 6.6(a). The table shows that the TFCA provides the minimum fit error and the interference energy among the computed distributions.

auto–term WD. Although the auto–term WD is a desirable distribution, in general it is not computable. However for the synthetic test signal considered here, since the component $s^i(t)$ constituting the composite signal $x(t)$ are known beforehand, auto–term WD can be computed as $W_A(t,f) = \sum_{i=1}^{3} W_i(t,f)\, M_{W_i}(t,f)$, where $W_i(t,f)$ is the WD of $s^i(t)$ and $M_{W_i}(t,f)$ is the indicator function describing the support of the i^{th} auto–term obtained by using the watershed segmentation algorithm [3]. Under this performance criterion, the fit errors and interference energy associated with the distributions given by WD, TFCA, PWD, reassigned PWD, SPWD, reassigned SPWD, spectrogram, reassigned spectrogram and ORGK techniques are given in Table 6.1. The tabulated values show that, TFCA performs significantly better than the other distributions studied in this simulation example.

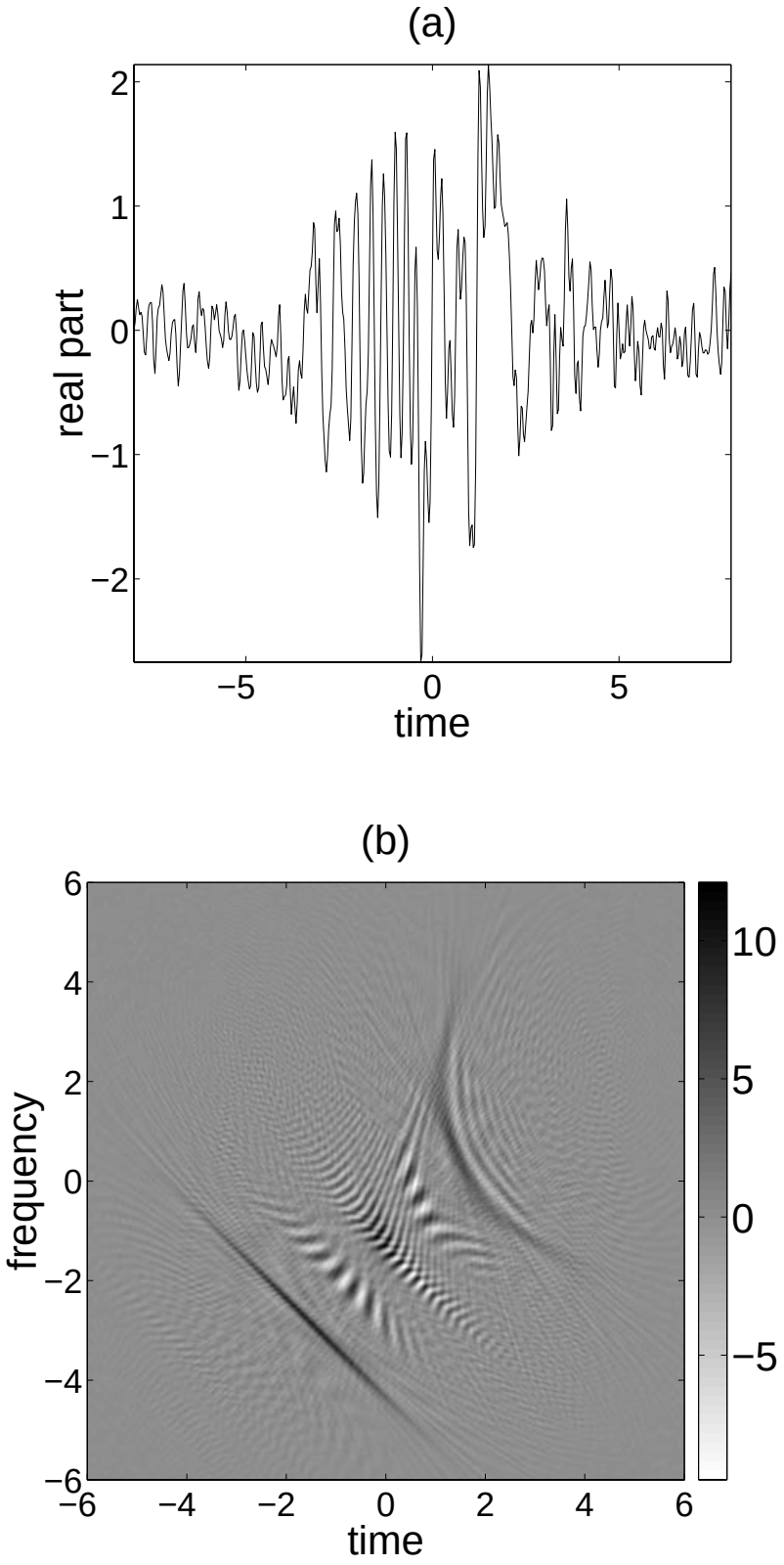

Figure 6.6: (a) The time domain representation of a multi–component signal $x(t)$ and (b) its Wigner distribution $W_x(t, f)$. While the signal component with non–convex t–f support in (b) suffers from inner interference terms, the middle signal component is completely immersed under outer interference terms.

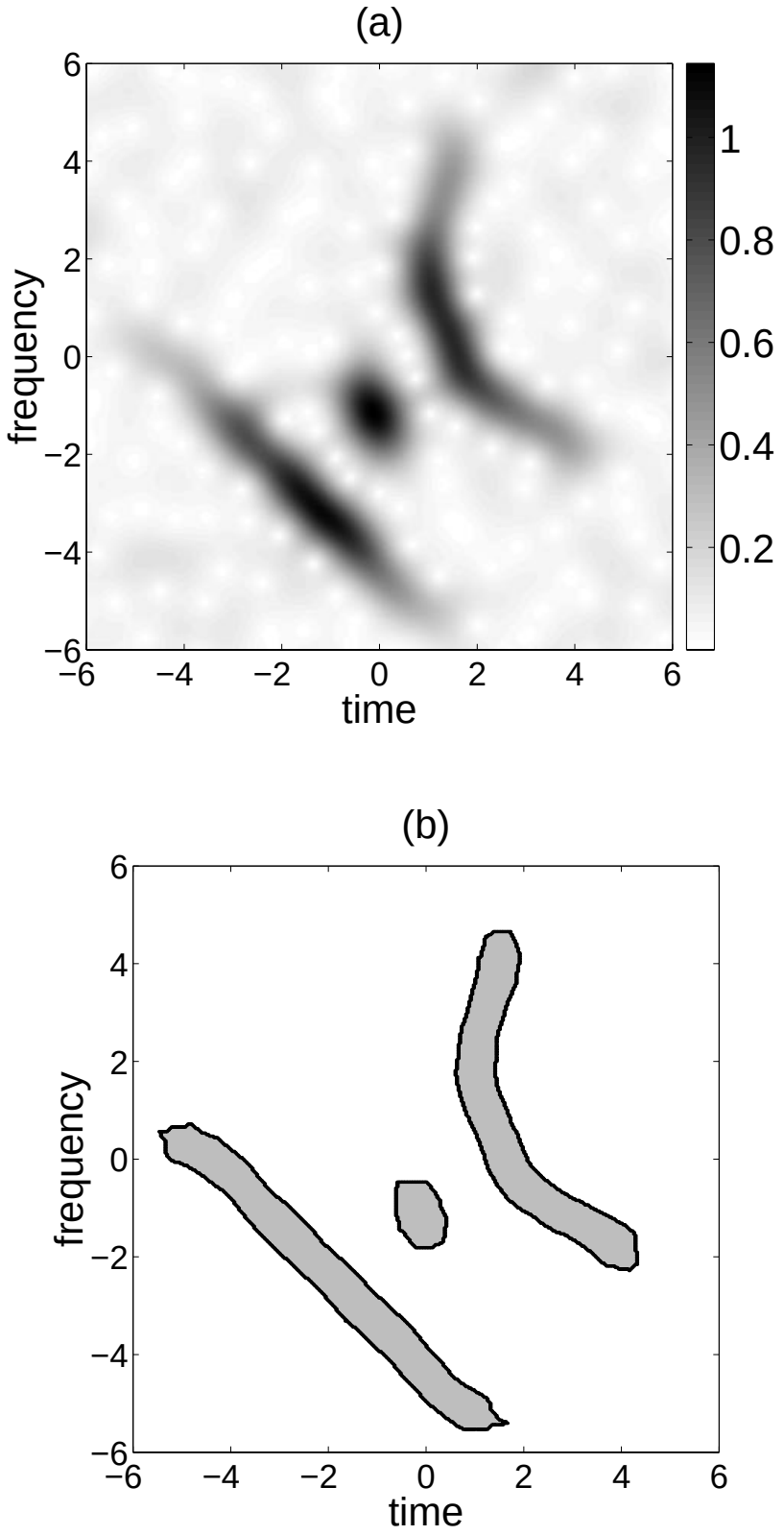

Figure 6.7: (a) The short time Fourier transform of $x(t)$ given in Fig. 6.6 (a) computed by using the window function $h(t) = e^{-\pi t^2}$, (b) supports of the components in STFT computed by using the watershed segmentation algorithm [3]

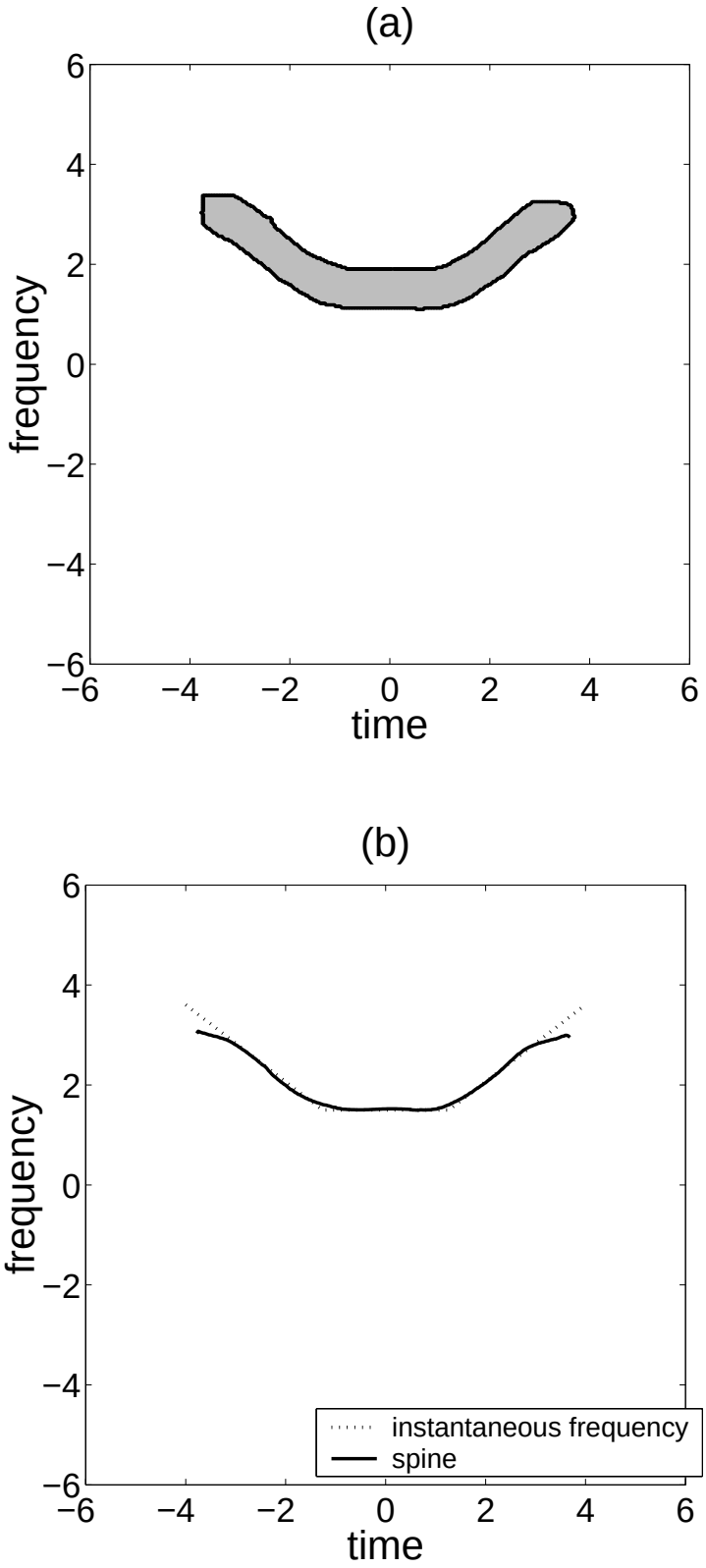

Figure 6.8: (a) The indicator function $M_{a_1}(t, f)$, $a_1 = -0.75$, designating the support of the component $s_1(t)$ in the a_1^{th} fractional domain, (b) the computed spine and the actual instantaneous frequency of the component $s_1(t)$ in the a_1^{th} fractional domain.

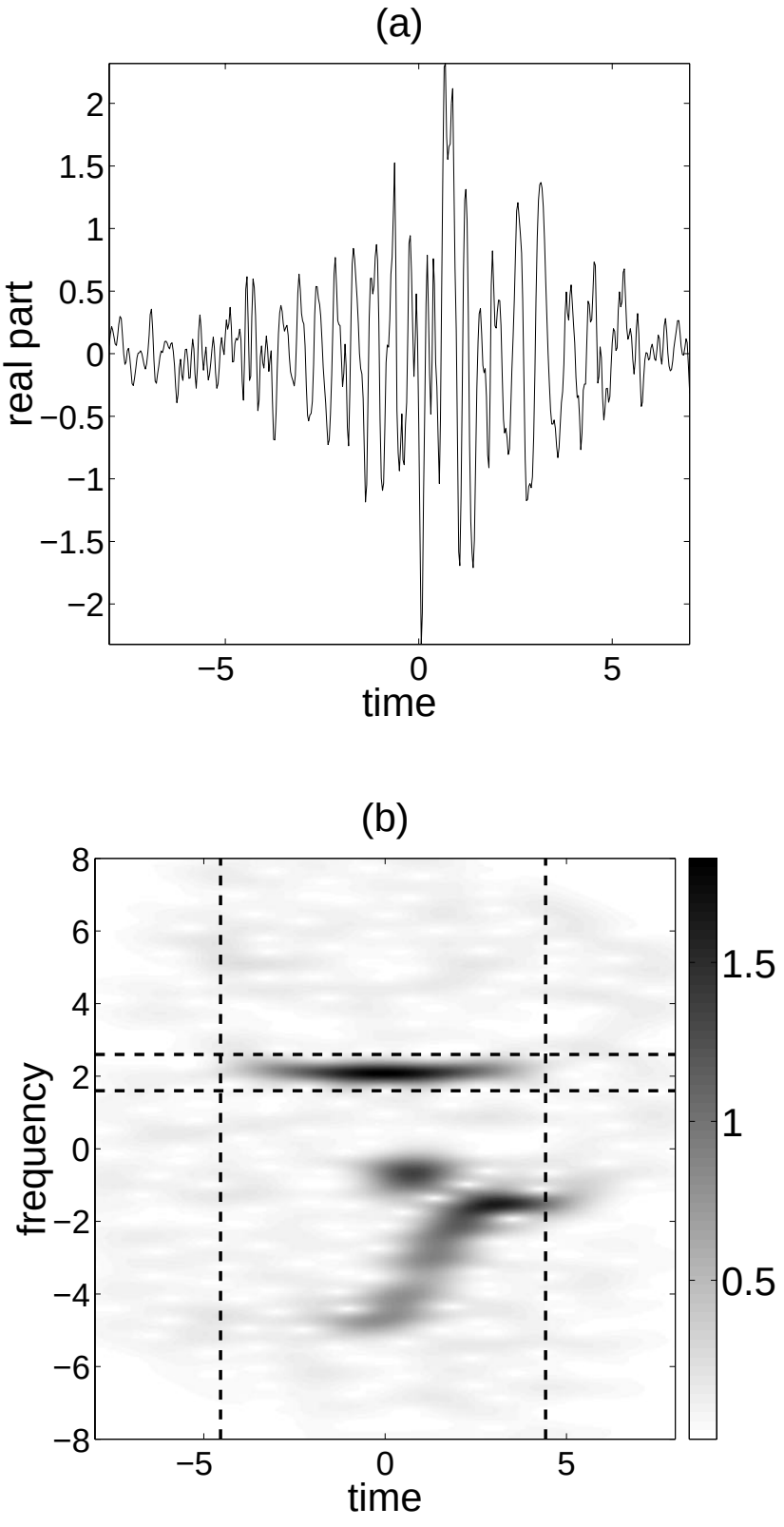

Figure 6.9: (a) the warped FrFT $x_{a_1,\zeta_1}(t)$ of the signal given in Fig. 6.6(a), and (b) its short time Fourier transform $STFT_{(x_{a_1,\zeta_1})}(t,f)$. The horizontal and vertical lines in (b) designate the supports of the frequency and time domain incision masks, respectively, which are utilized by TFCA to extract the signal component located inside the dashed rectangular box.

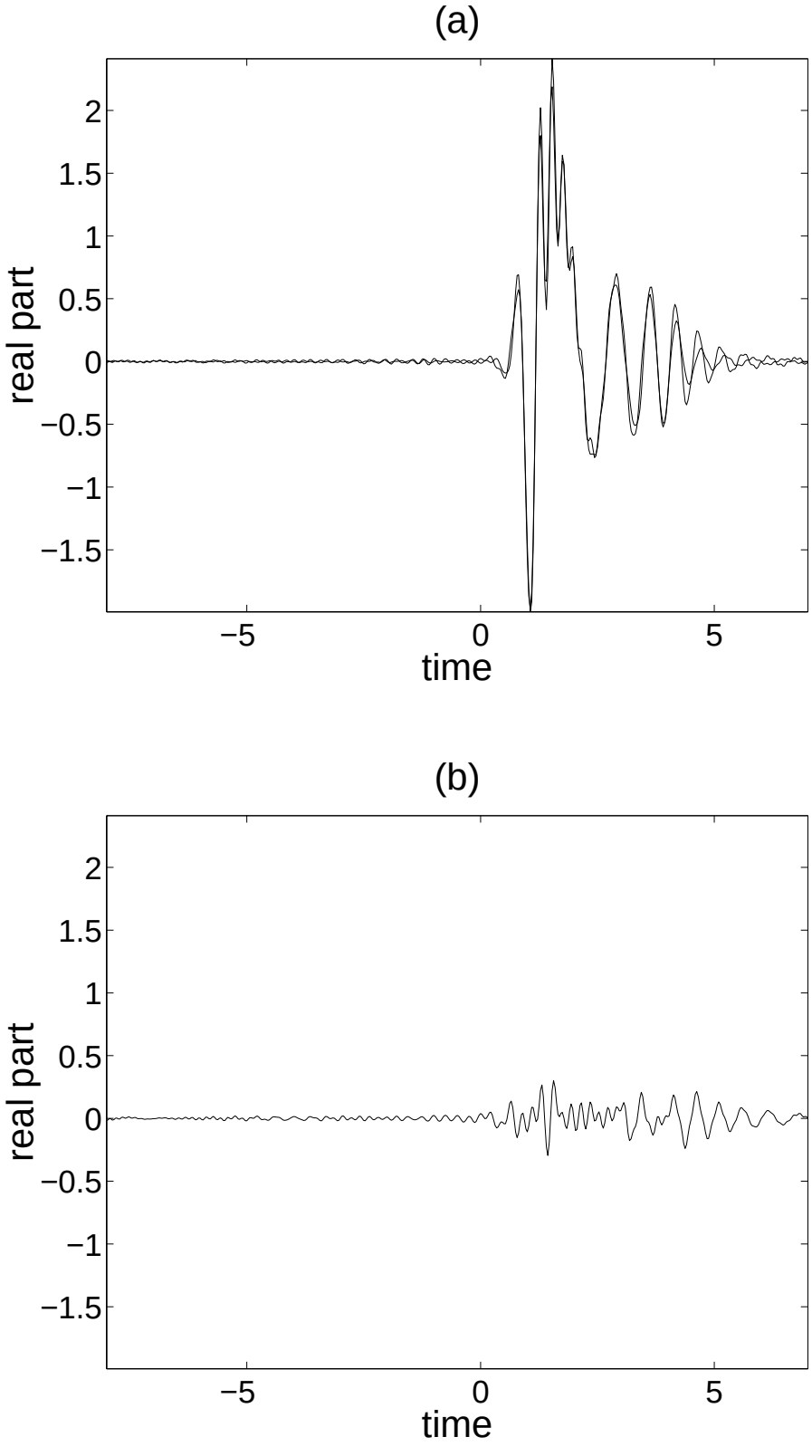

Figure 6.10: (a) The overlay plot of component $s^1(t)$ and its estimate $\hat{s}^1(t)$ computed by TFCA, and (b) the corresponding estimation error. Although the composite signal shown in Fig. 6.6(a) is very much corrupted with noise, the TFCA provides fairly good estimate of the analyzed signal component.

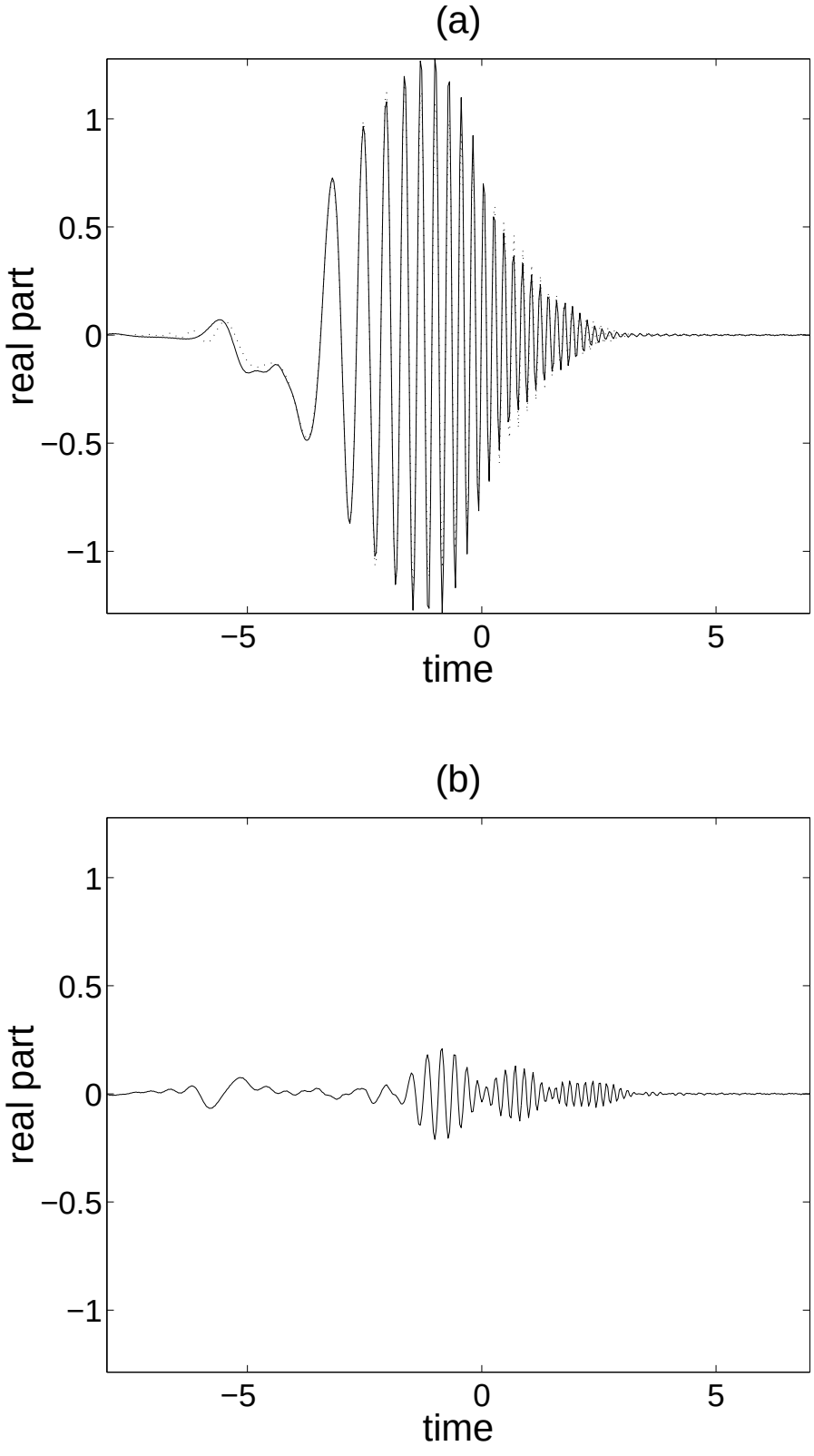

Figure 6.11: (a) The overlay plot of component $s^2(t)$ and its estimate $\hat{s}^2(t)$ computed by TFCA, and (b) the corresponding estimation error. Although the composite signal shown in Fig. 6.6(a) is very much corrupted with noise, the TFCA provides fairly good estimate of the analyzed signal component.

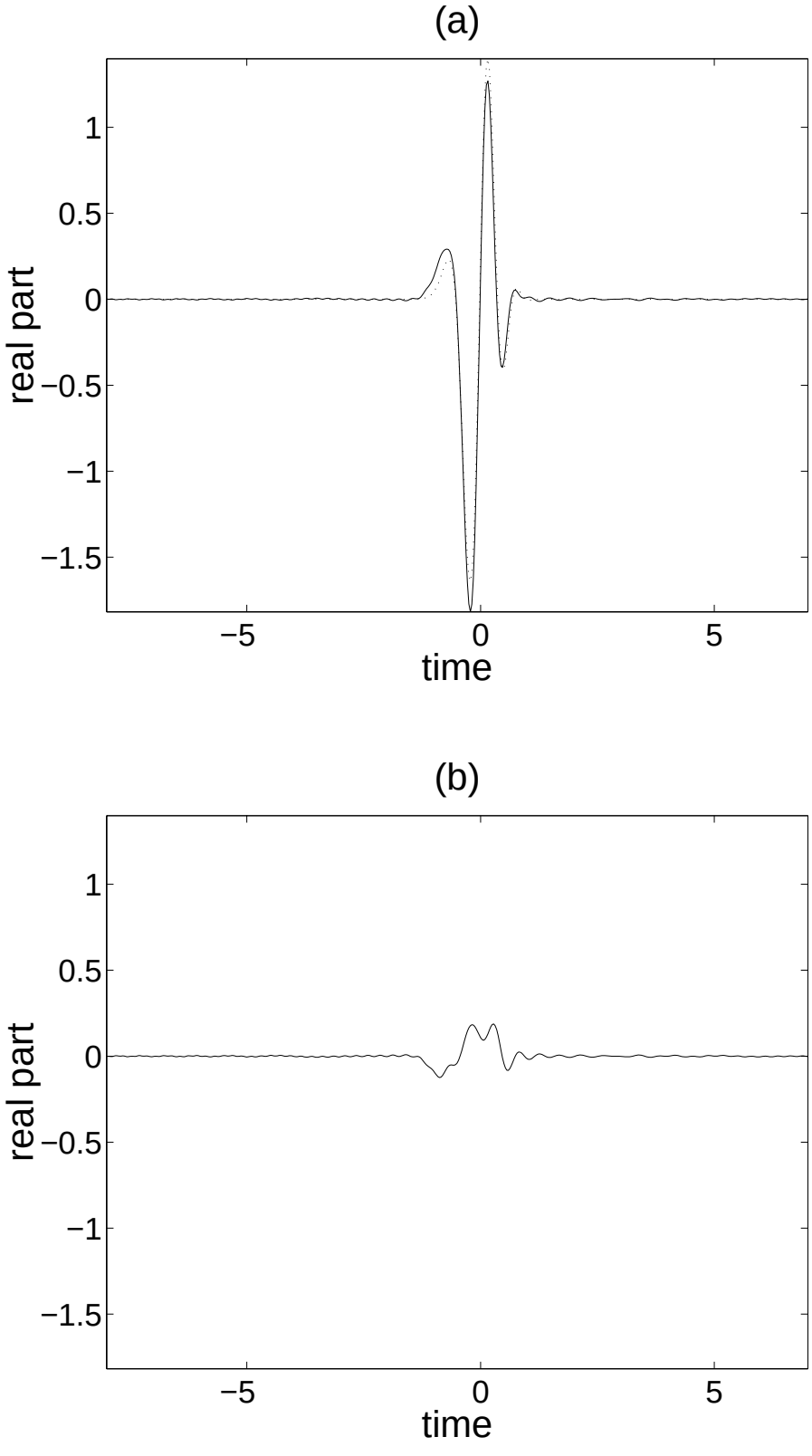

Figure 6.12: (a) The overlay plot of component $s^3(t)$ and its estimate $\hat{s}^3(t)$ computed by TFCA, and (b) the corresponding estimation error. Although the composite signal shown in Fig. 6.6(a) is very much corrupted with noise, the TFCA provides fairly good estimate of the analyzed signal component.

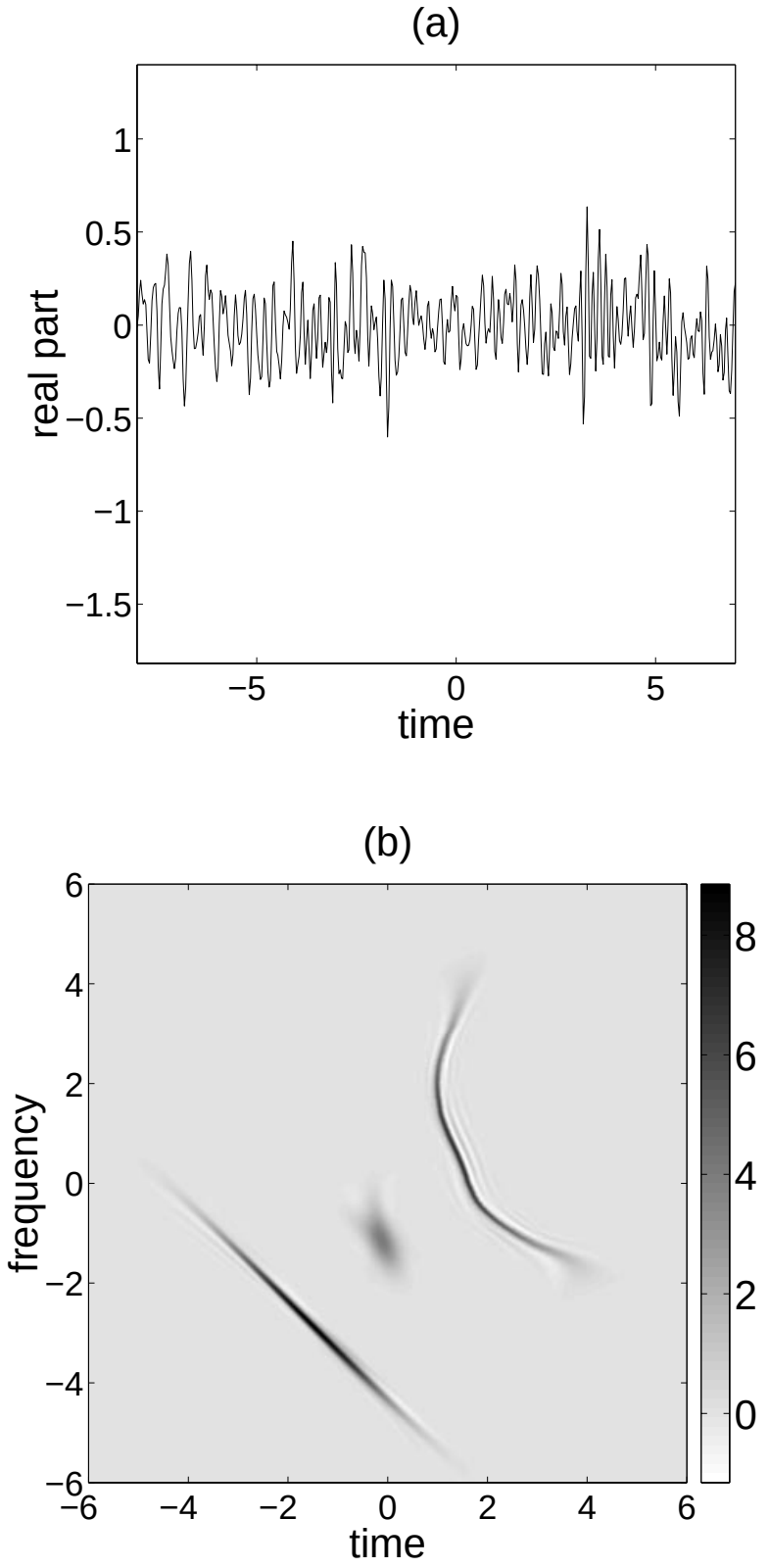

Figure 6.13: (a) The residual signal $r^3(t) = x(t) - \hat{s}_1(t) - \hat{s}_2(t) - \hat{s}_3(t)$, and (b) the time–frequency distribution of the signal given in Fig. 6.6(a) computed by TFCA. In TFCA, the TFD of the composite signal $x(t)$ is computed by first extracting the individual signal components, and then summing the TFDs of the extracted components which are computed by using fractional domain warping algorithm.

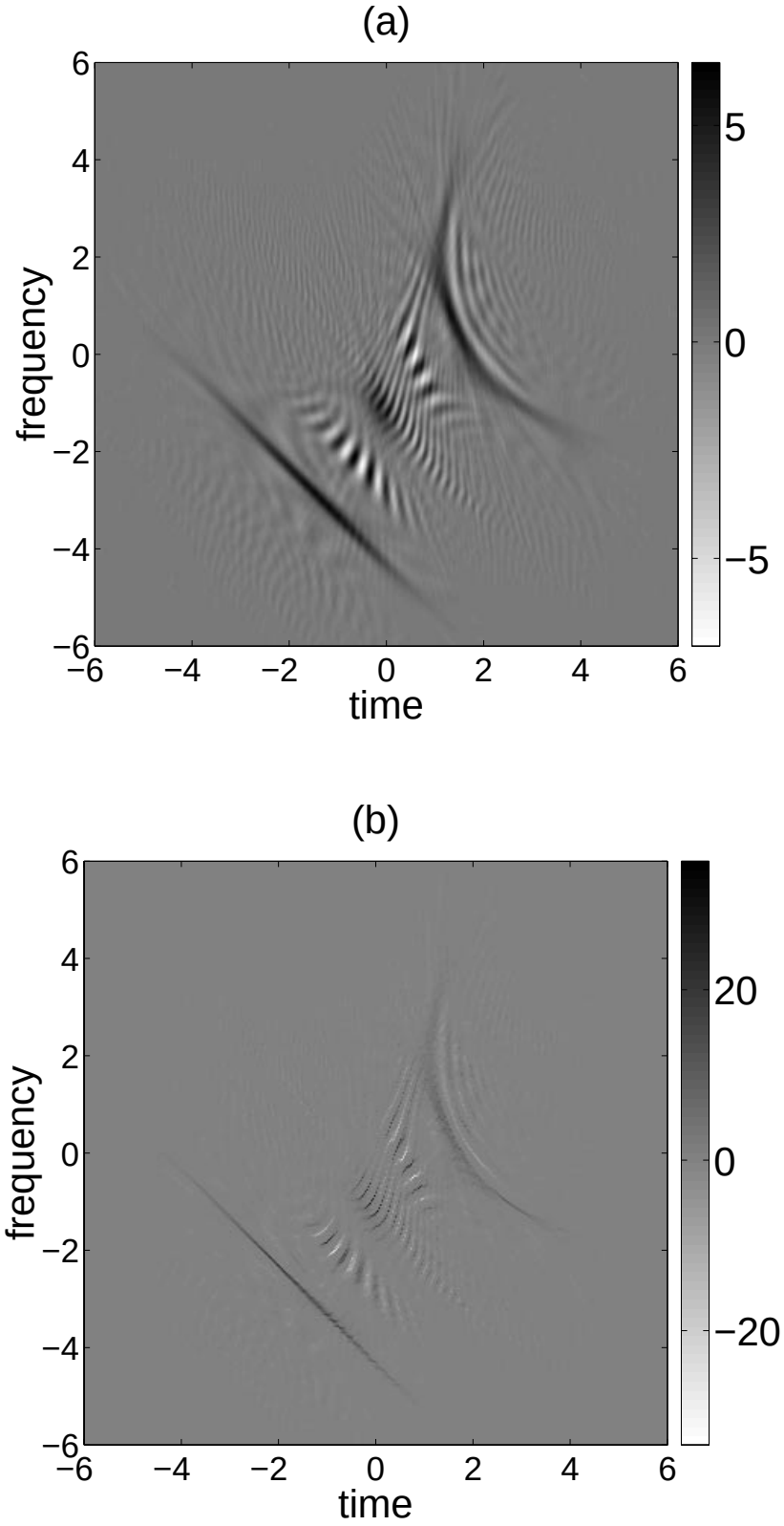

Figure 6.14: (a)–(b) The TFD of the signal given in Fig. 6.6(a) obtained by using the PWD and reassigned PWD techniques, respectively.

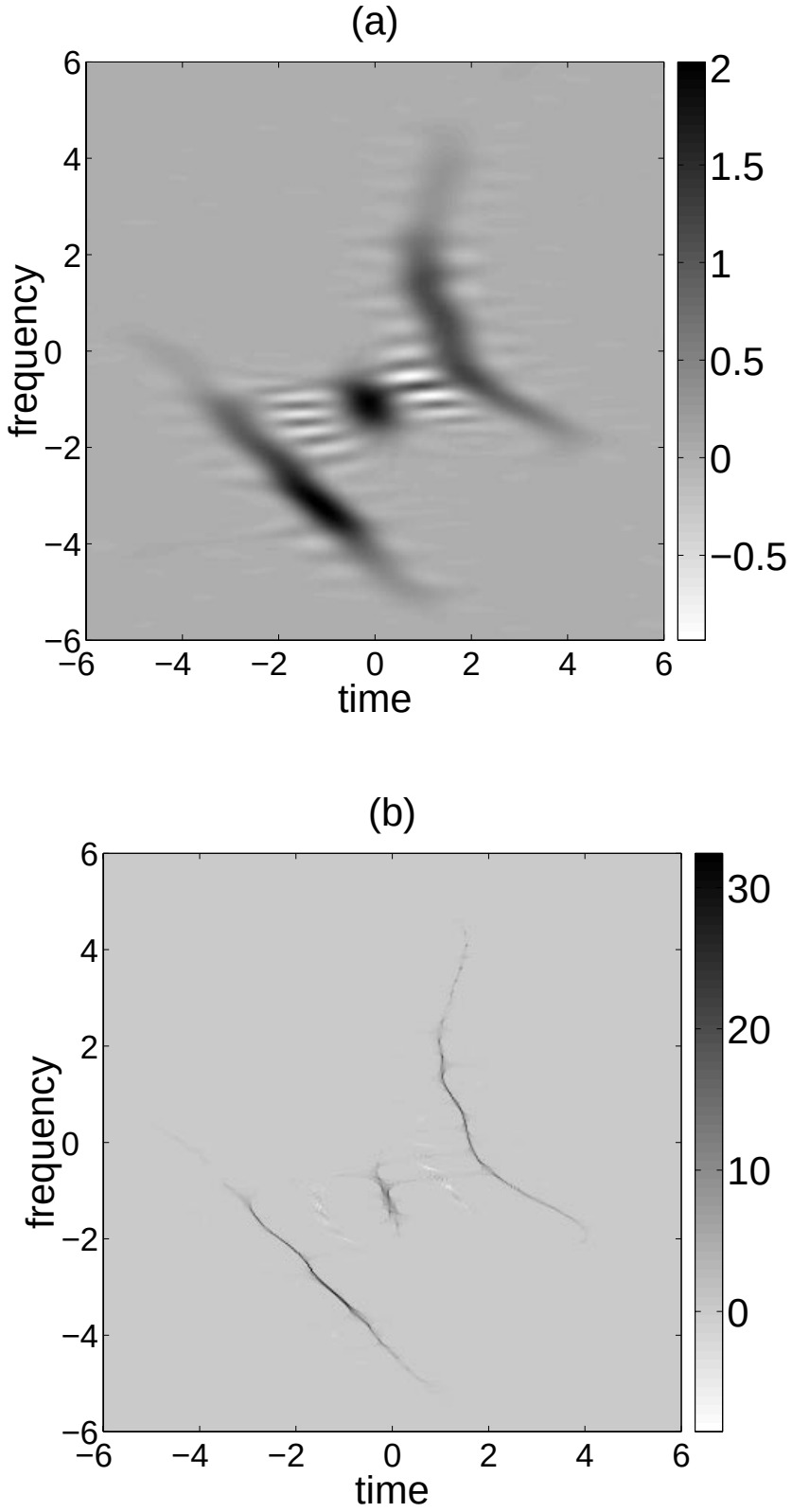

Figure 6.15: (a)–(b) The TFD of the signal given in Fig. 6.6(a) obtained by using the SPWD and reassigned SPWD techniques, respectively.

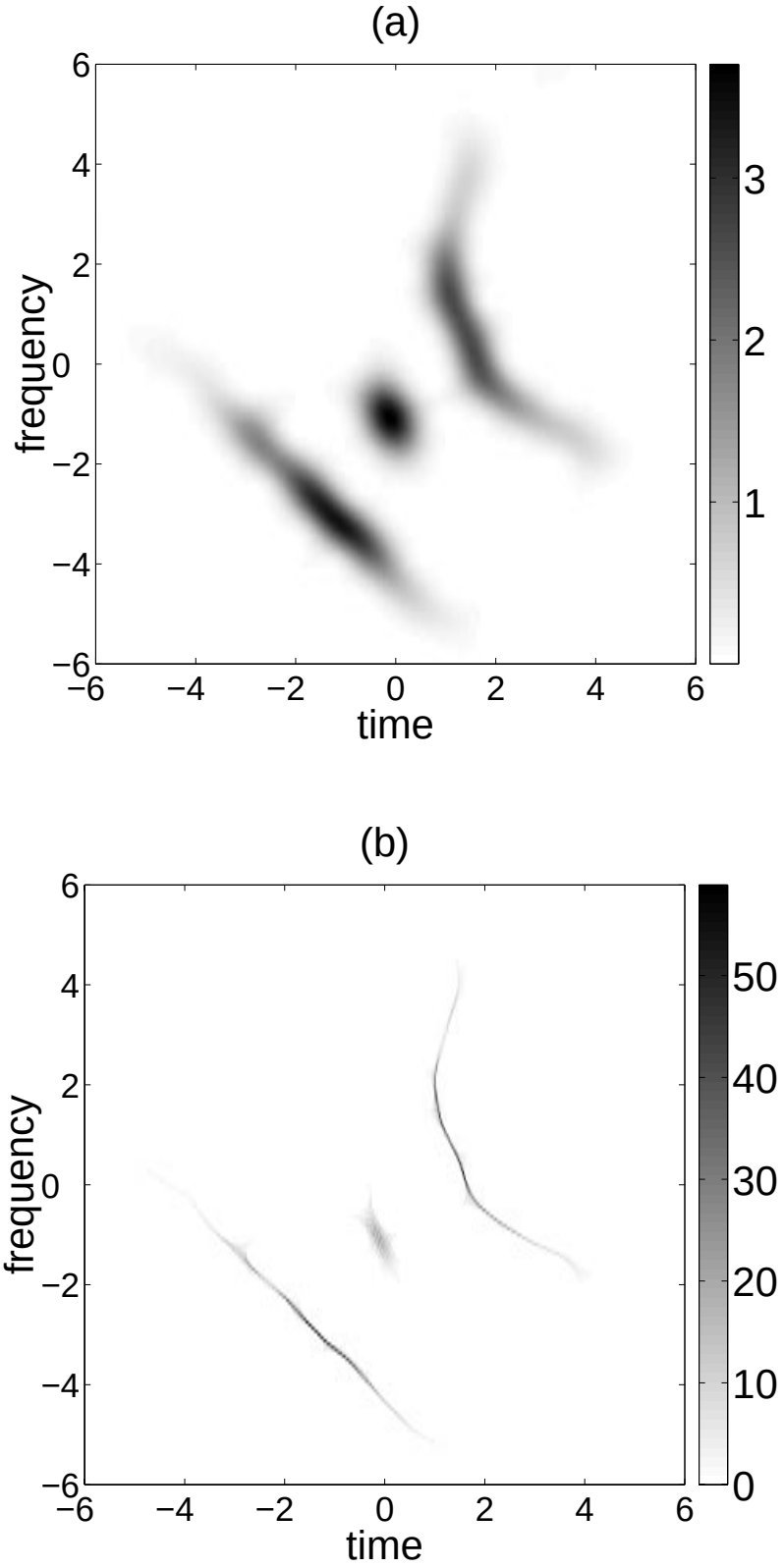

Figure 6.16: (a)–(b) The TFD of the signal given in Fig. 6.6 (a) obtained by using the spectrogram and reassigned spectrogram techniques, respectively.

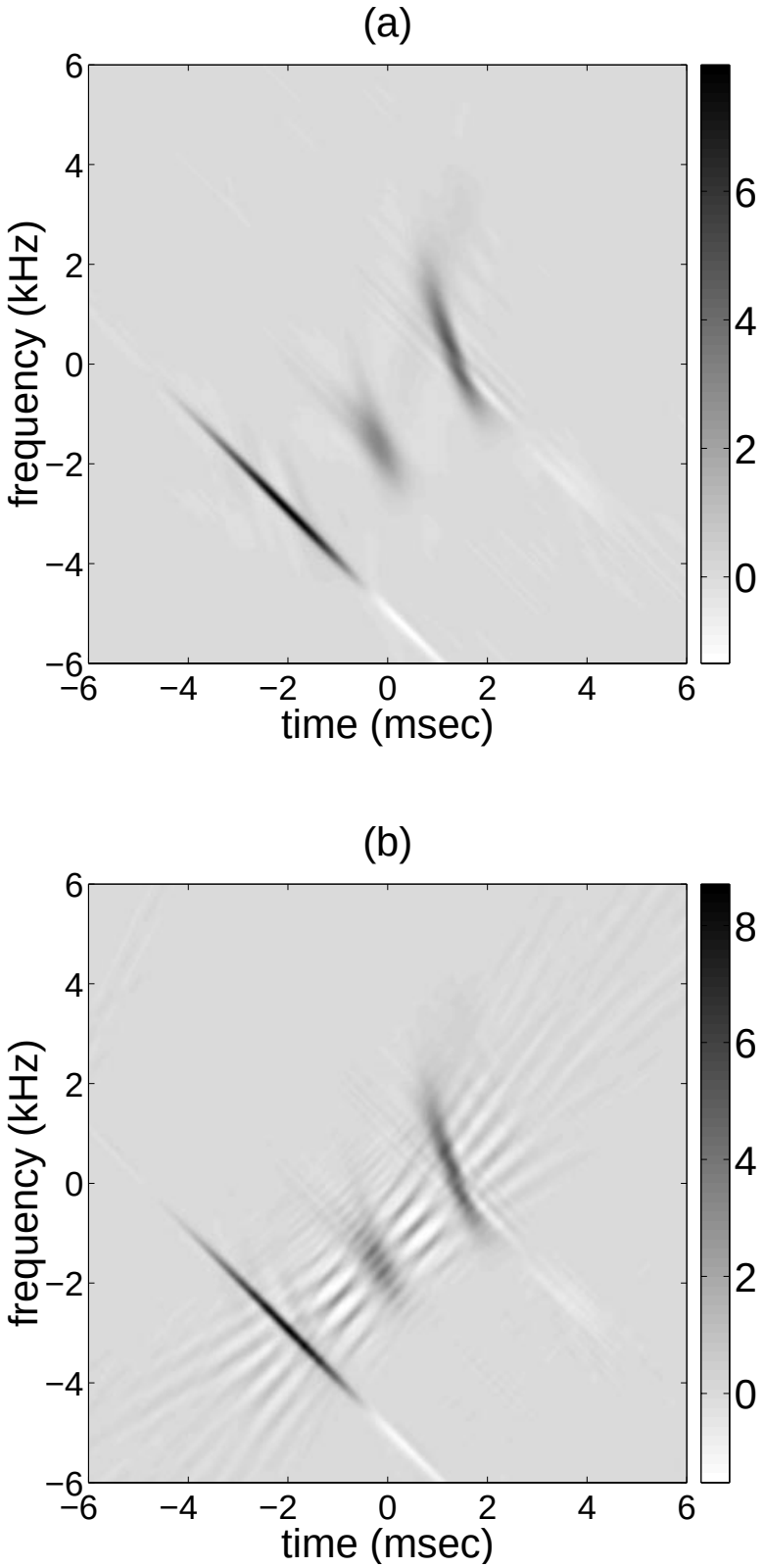

Figure 6.17: (a)–(b) The TFDs of the signal given in Fig. 6.6(a) obtained by using the optimal radially Gaussian kernel technique. In (a) and (b) the volume parameter used in ORGK was chosen as $\alpha = 3$ and $\alpha = 5$, respectively.

6.3.1 Analysis of a recorded bat echolocation signal by TFCA

Since the components of the synthetic test example are known, it served well in assessing the accuracies of the estimated signal components by TFCA. In the rest of this section, to illustrate the performance of TFCA on real signals, a recorded bat sound is analyzed. Also, a comparison of the TFCA and some other well known time–frequency representations is given. The recorded signal is a digitized 2.5 ms echolocation pulse emitted by a large brown bat, eptesicus fuscus, which is plotted in Fig. 6.18(a) and can be downloaded at [4]. As shown in the WD plot given in Fig. 6.18(b), the analyzed signal is composed of several components with non–convex time–frequency supports. Therefore, the WD contains both inner and outer interference terms. The result of TFCA on this signal are given in Fig. 6.19 – 6.22, where Fig. 6.19 – 6.21 show the estimates of the signal components provided by TFCA which is a distinctive benefit compared with conventional TFDs. The TFD of bat signal computed by TFCA provides well localized supports for the analyzed signal components as shown in Fig. 6.22. Since the TFCA first extracts signal components and then computes the time–frequency distributions of extracted signal components, the time–frequency distribution obtained for the weakest signal component is as good as the time–frequency distribution of the strongest signal component. The results of PWD, SPWD, spectrogram and the corresponding reassignment methods on the same bat echolocation signal are given in Fig. 6.23 – 6.25, respectively. For this simulation, the reassigned smoothed pseudo WD and reassigned spectrogram provides a visually clearer picture than the reassigned PWD. However these figures also show that, after the reassignment operation, the relative strength of the weakest component is considerably reduced relative to the stronger components. This is a problem arising from mapping energy at different points in t–f plane to the same location. Fig. 6.26(a)–(b) shows the ORGK time–frequency distribution of the same signal, for the corresponding volume parameters of $\alpha = 3$ and $\alpha = 5$, respectively. Although ORGK suppresses the outer interference terms very effectively, the TFCA provides a better localization of the chirping components. This observation is more evident for the chirp component which is located at the lower part of the time–frequency plane, especially between the time intervals of 0 and 0.5 ms. Furthermore, there is a decrease of time–frequency resolution compared with the WD and TFCA. For instance, the support of the weak chirp component which is located at the top part of the time–frequency plane is dispersed in the ORGK time–frequency distribution as shown in Fig. 6.26.

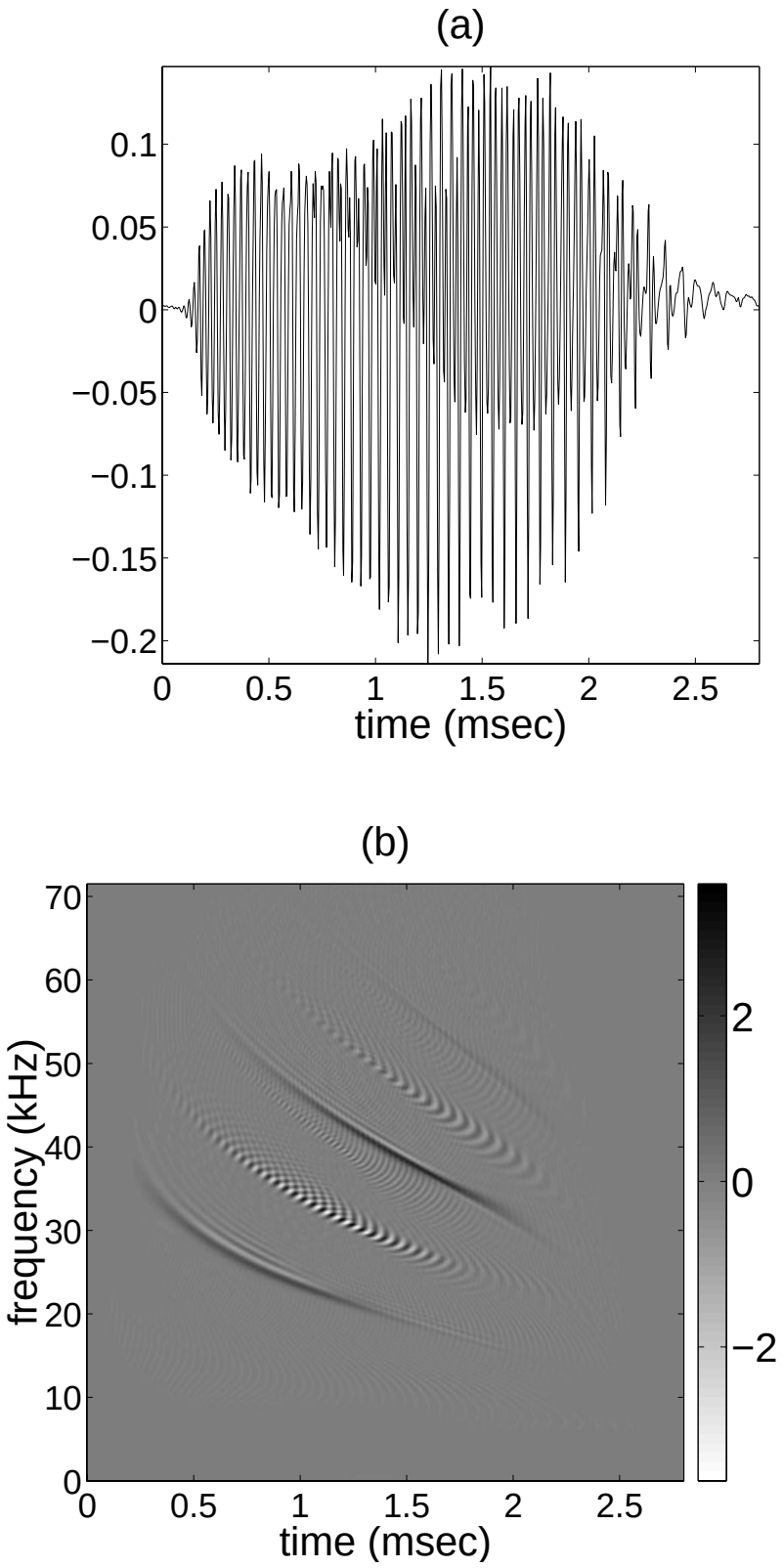

Figure 6.18: (a) Digitized 2.5 microsecond echolocation pulse emitted by the large brown bat, Eptesicus Fuscus [4] and (b) its Wigner distribution.

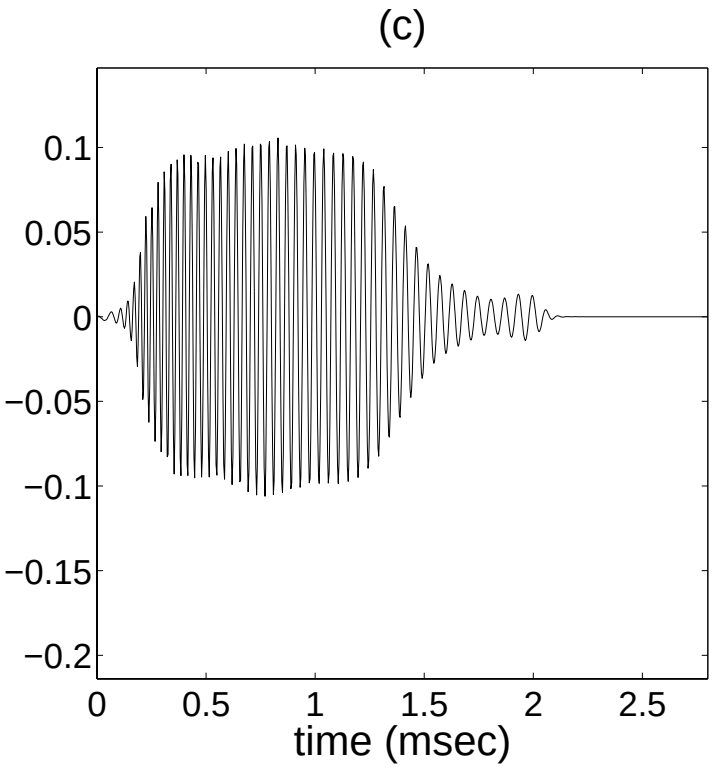

Figure 6.19: The TFCA estimate of chirping component located in the bottom part of the t–f plane in Fig. 6.18(b).

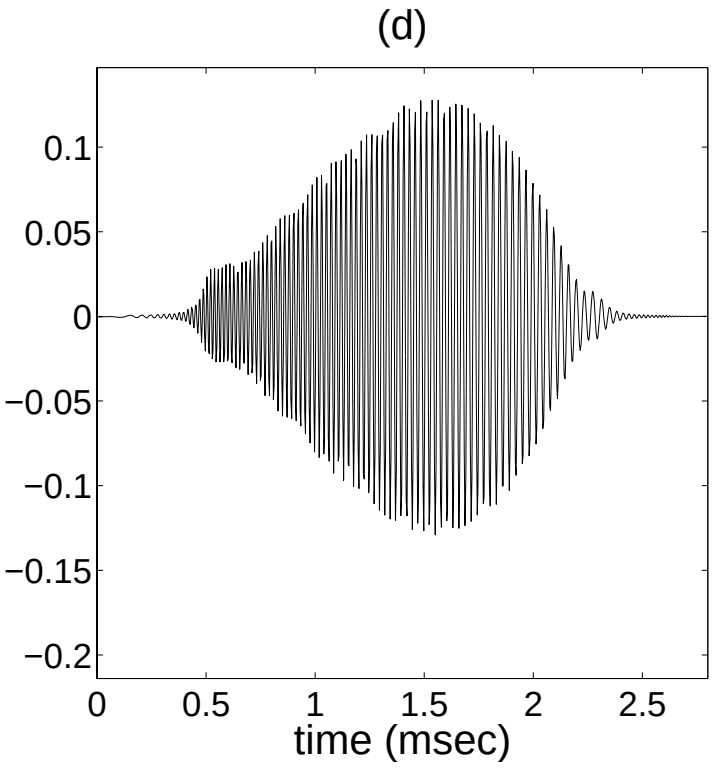

Figure 6.20: The TFCA estimate of chirping component located in the middle part of the t–f plane in Fig. 6.18(b).

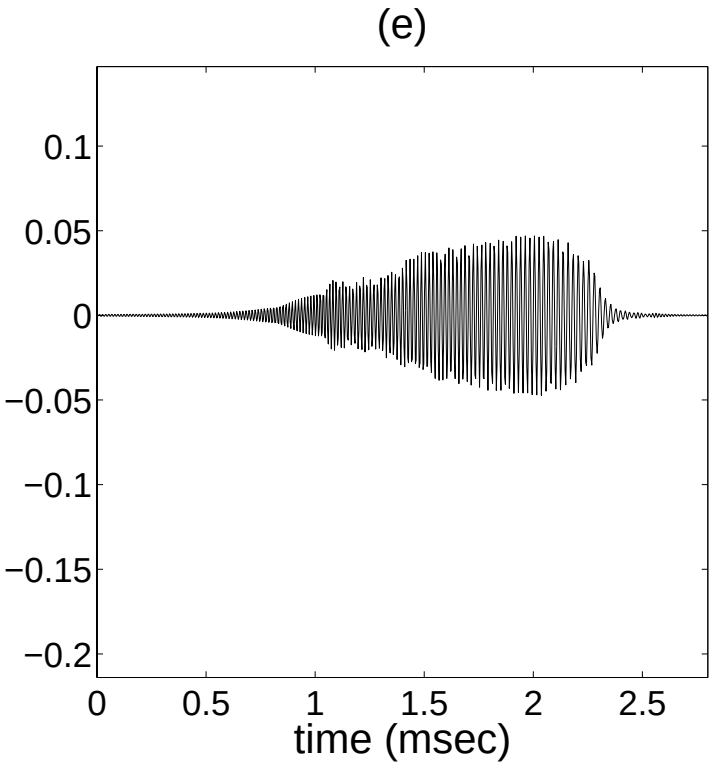

Figure 6.21: The TFCA estimate of chirping component located in the top part of the t–f plane in Fig. 6.18(b).

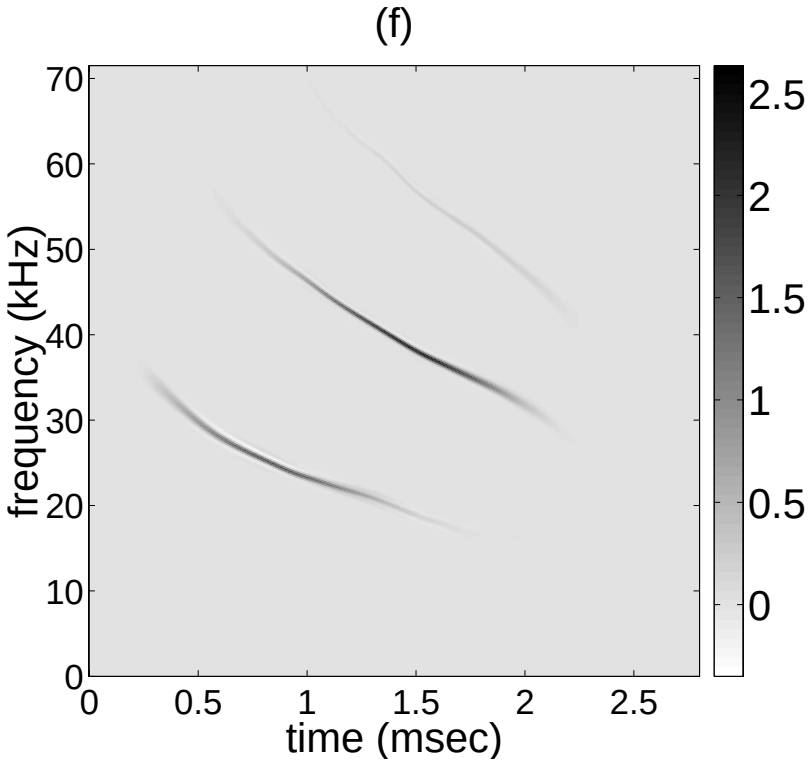

Figure 6.22: The TFD of the bat echo given in Fig. 6.18(a) provided by the TFCA.

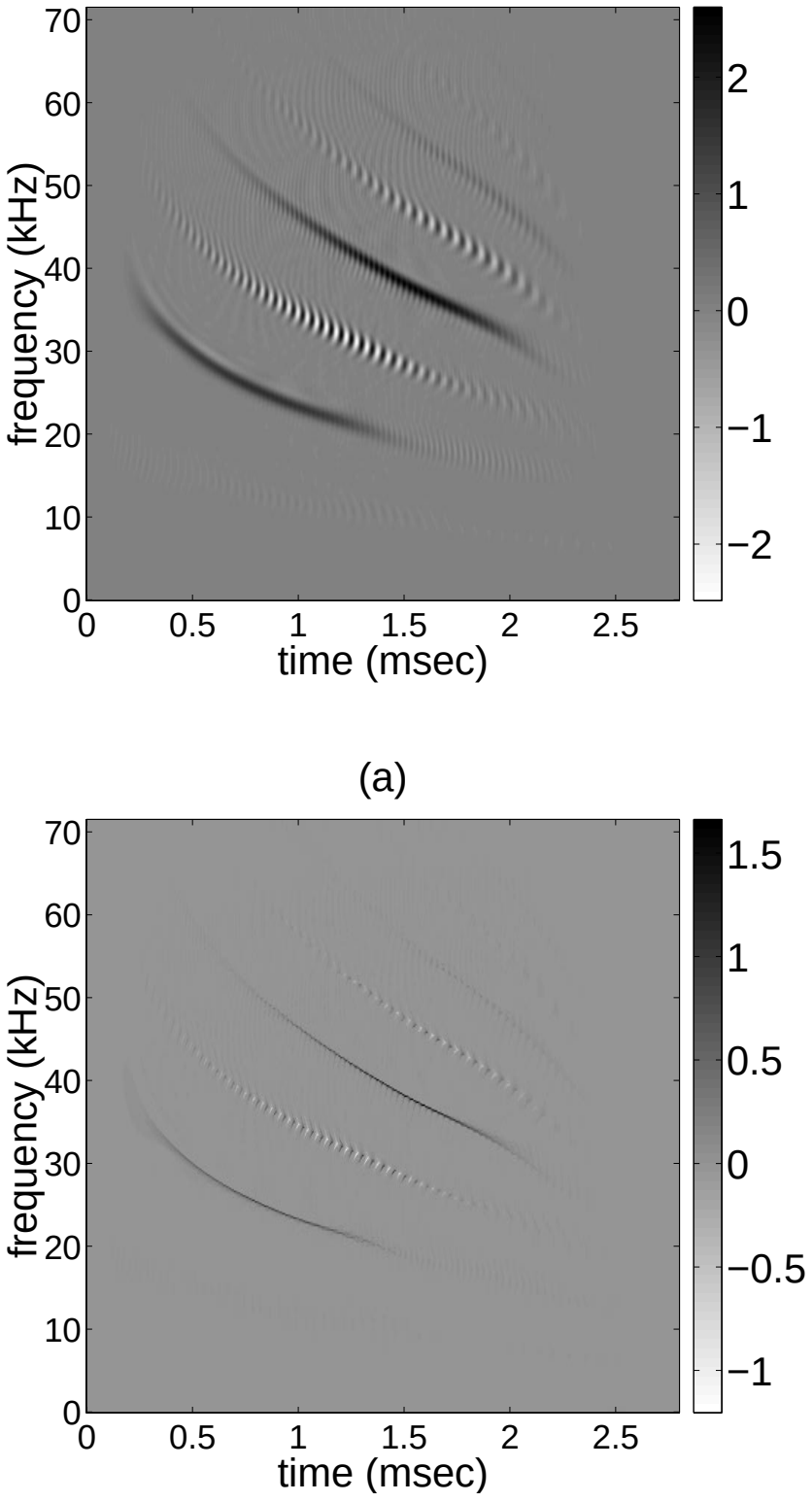

Figure 6.23: The TFDs of the bat signal shown in Fig. 6.18(a) computed by using (a) PWD and (b) reassigned PWD techniques, respectively.

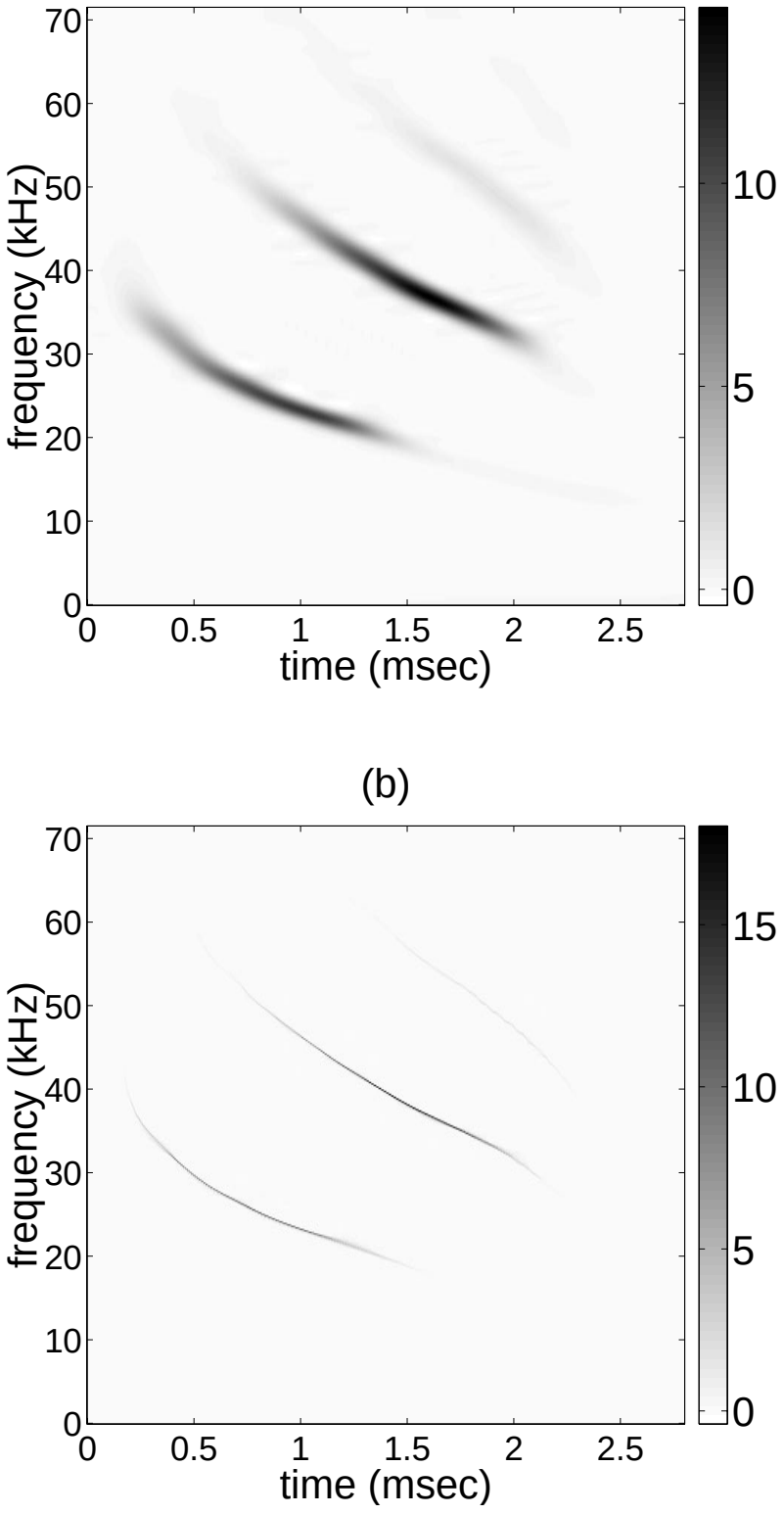

Figure 6.24: The TFDs of the bat signal shown in Fig. 6.18(a) computed by using (a) SPWD and (b) reassigned SPWD techniques, respectively.

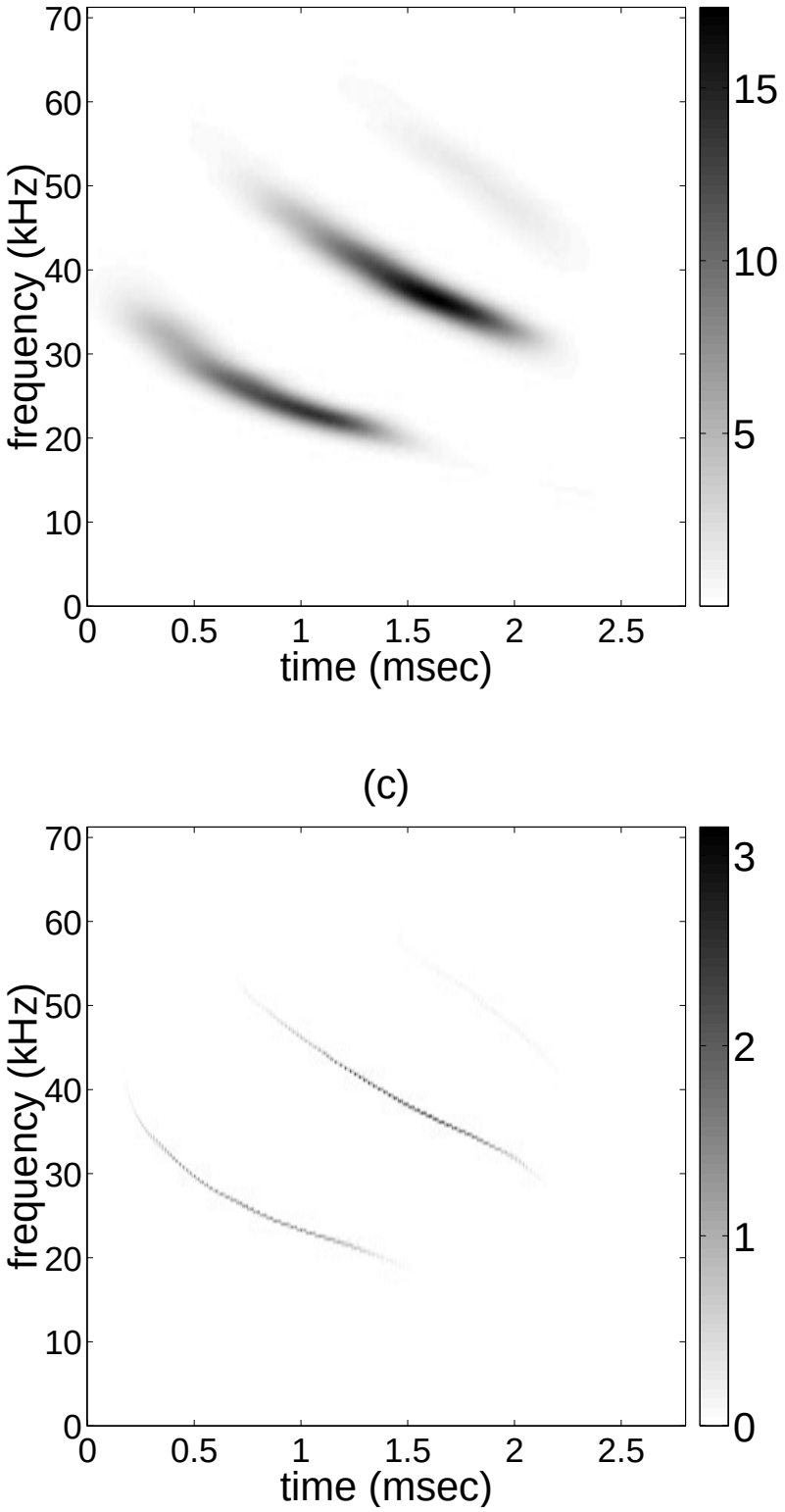

Figure 6.25: The TFDs of the bat signal shown in Fig. 6.18 (a) computed by using (a) spectrogram and (b) reassigned spectrogram techniques, respectively.

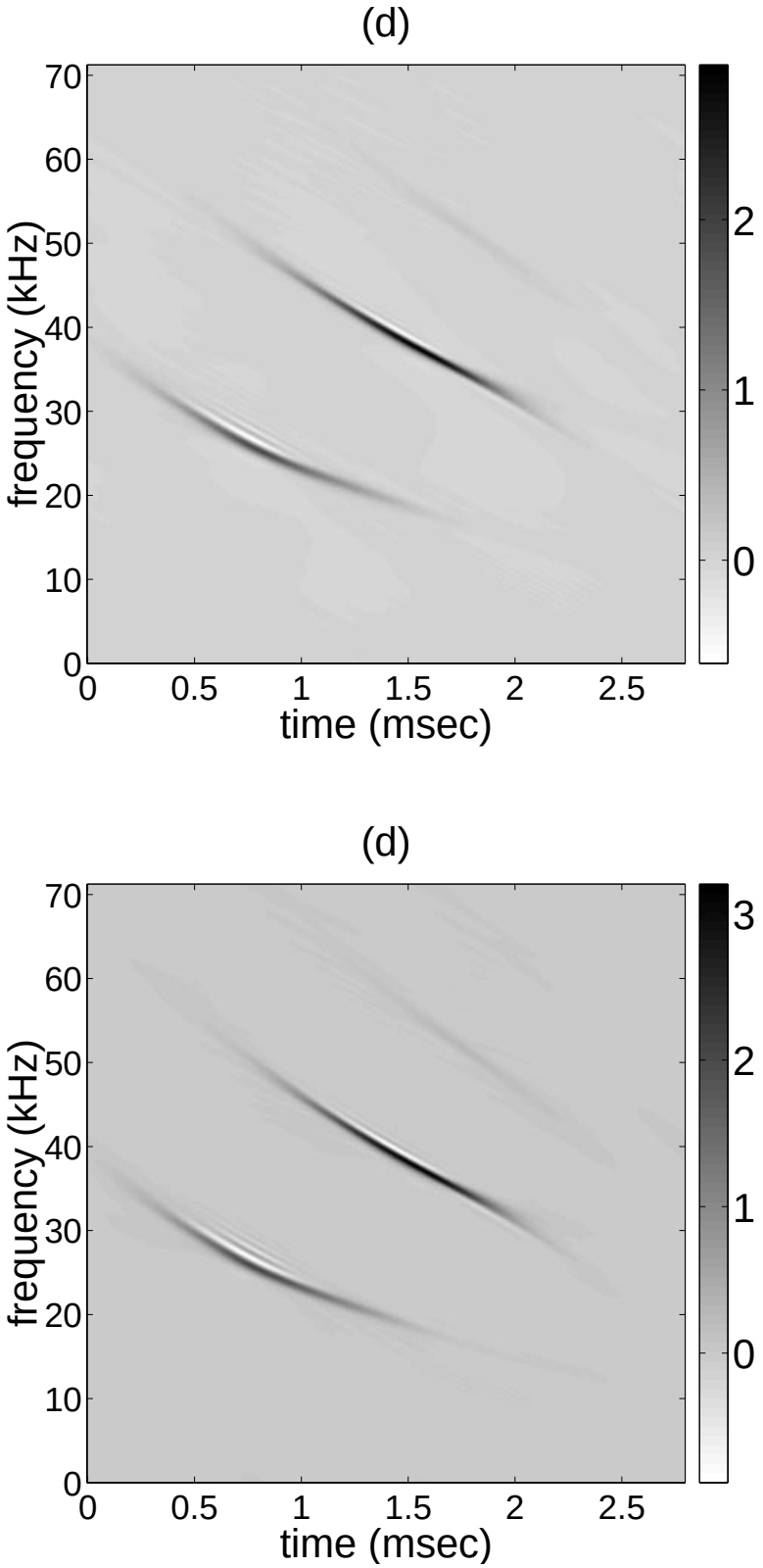

Figure 6.26: The TFDs of the bat signal shown in Fig. 6.18(a) computed by using the optimal radially Gaussian kernel technique. In (a) and (b) the volume parameter used in ORGK was chosen as $\alpha = 3$ and $\alpha = 5$, respectively.

6.3.2 Analysis of a recorded ERP signal by TFCA

In this section we investigate the performance of the proposed algorithm on the real data set shown in Fig. 6.27(a). This 2–sec long data is the average of 28 measurements recorded at a sampling rate of 512 Hz in the Laboratory of Hacettepe Üniversitesi Uygulamalı Psikoloji Anabilim Dalı headed by Prof. Sirel Karakaş. Each recording is generated by the same human brain in response to an excitation given at the mid point of the observation interval ($t = 0$ in Fig. 6.27(a)). The prestimulus response is called as the electroencephalogram (EEG), and the poststimulus response as the Event Related Potential (ERP). EEG and ERP, together are called as recorded frame in this study [5]. The Wigner distribution of this signal given in Fig. 6.27(b) is very much contaminated with cross–terms and noise. Thus, the WD does not provide very useful results, in this example. The results of TFCA on this signal are given in Fig. 6.28 – 6.30, where Fig. 6.28 and Fig. 6.29 show the estimates of the signal components provided by TFCA and their corresponding high resolution time–frequency distributions. Since, TFCA based analysis enables the extraction of the identified components from the composite signals, it allows detailed post processing of the extracted signal components and their corresponding time–frequency distributions, as well. For instance, TFCA enables computation of the time and frequency centers and the corresponding time and frequency spreads of the identified components, which may have potential application in classification of data recorded under different experiments and from different subjects. The potential advantages of using TFCA in analysis of ERP signals is under investigation at Hacettepe Üniversitesi Uygulamalı Psikoloji Anabilim Dalı.

The results of PWD, SPWD, spectrogram, the corresponding reassignment methods and ORGK technique on the same recorded frame are given in Fig. 6.31 – 6.24, respectively. Although these methods are very well known and widely used in time–frequency signal processing, the TFCA provides significantly better distribution for the analyzed signal, in this simulation example.

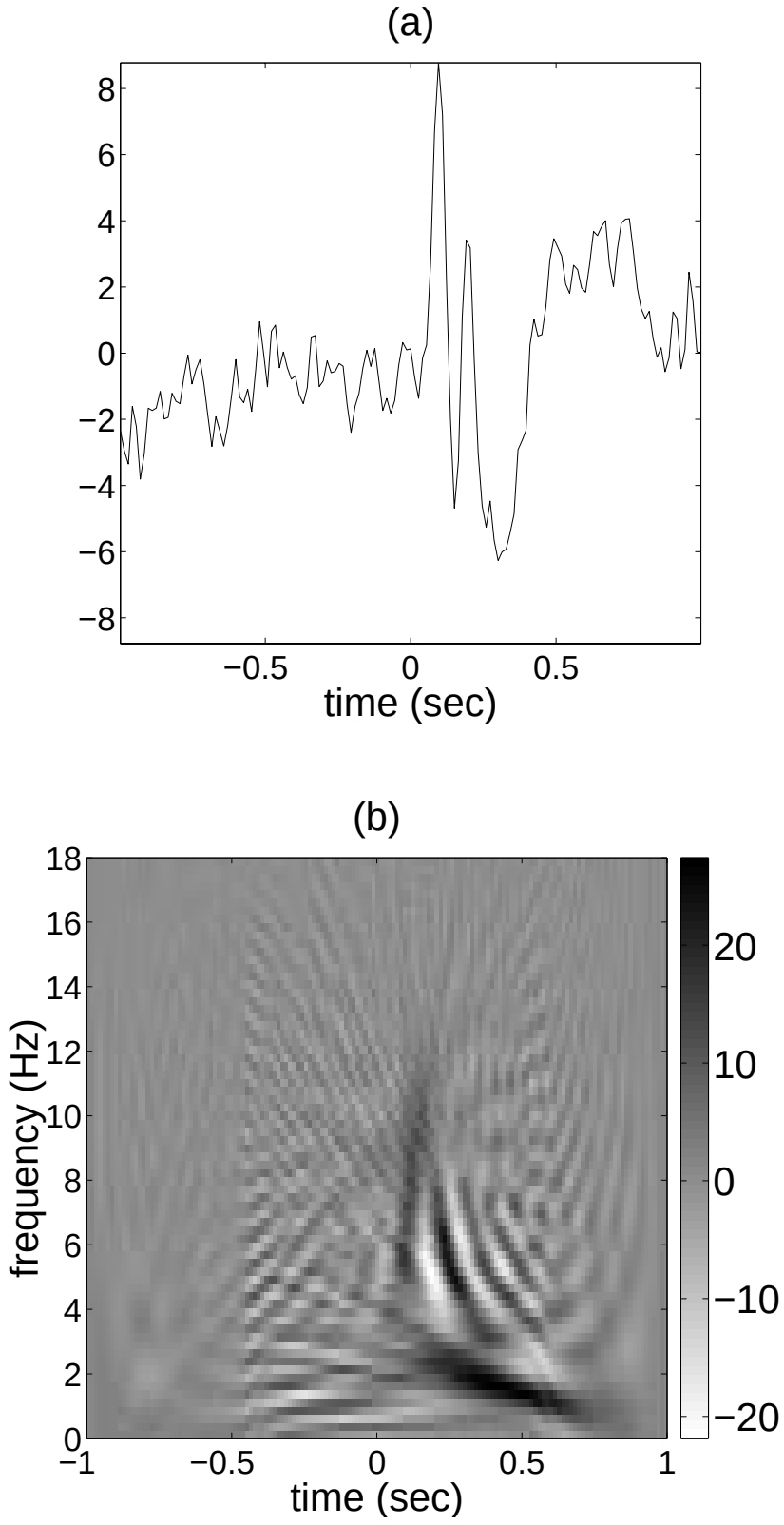

Figure 6.27: (a) The average of 28 measurements recorded from a human brain in response to a stimulus applied at $t = 0$ sec. The prestimulus response is called as the electroencephalogram (EEG), and the poststimulus response as the Event Related Potential (ERP). EEG and ERP, together are called as recorded frame [5]. The Wigner distribution of the averaged frame shown in (a) is contaminated by the existence of cross terms as seen in (b).

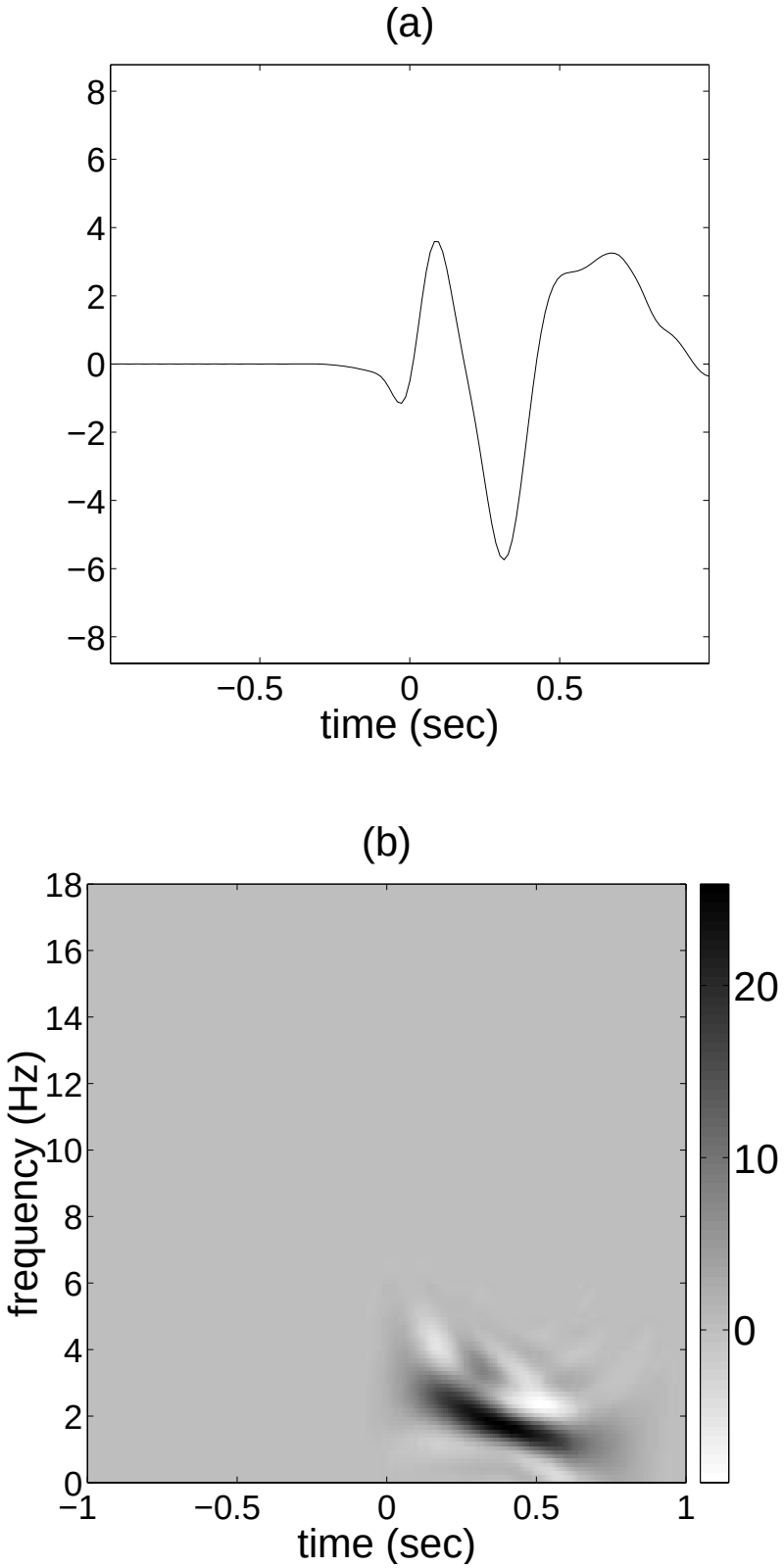

Figure 6.28: (a) The estimate of the first component in Fig. 6.27(a) and (b) its corresponding time-frequency distribution computed by TFCA. Time center of this component is 0.39 sec with a 0.22 msec spread, and its frequency center is 1.84 Hz with a 0.88 Hz spread.

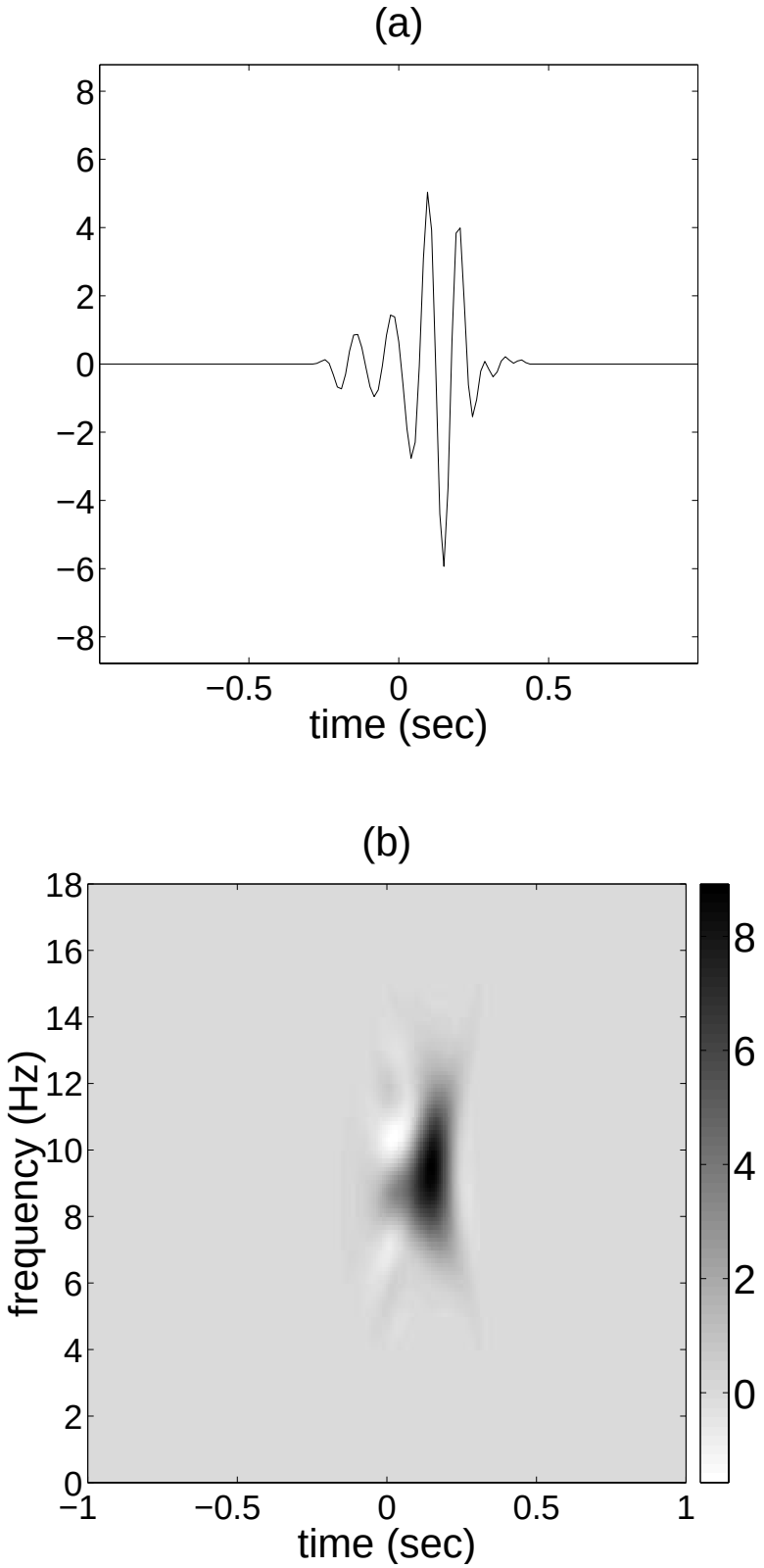

Figure 6.29: (a) The estimate of the second component in Fig. 6.27(a) and (b) its corresponding time–frequency distribution computed by TFCA. Time center of this component is 0.12 sec with a 0.074 sec spread, and its frequency center is 9.07 Hz with a 1.63 Hz spread.

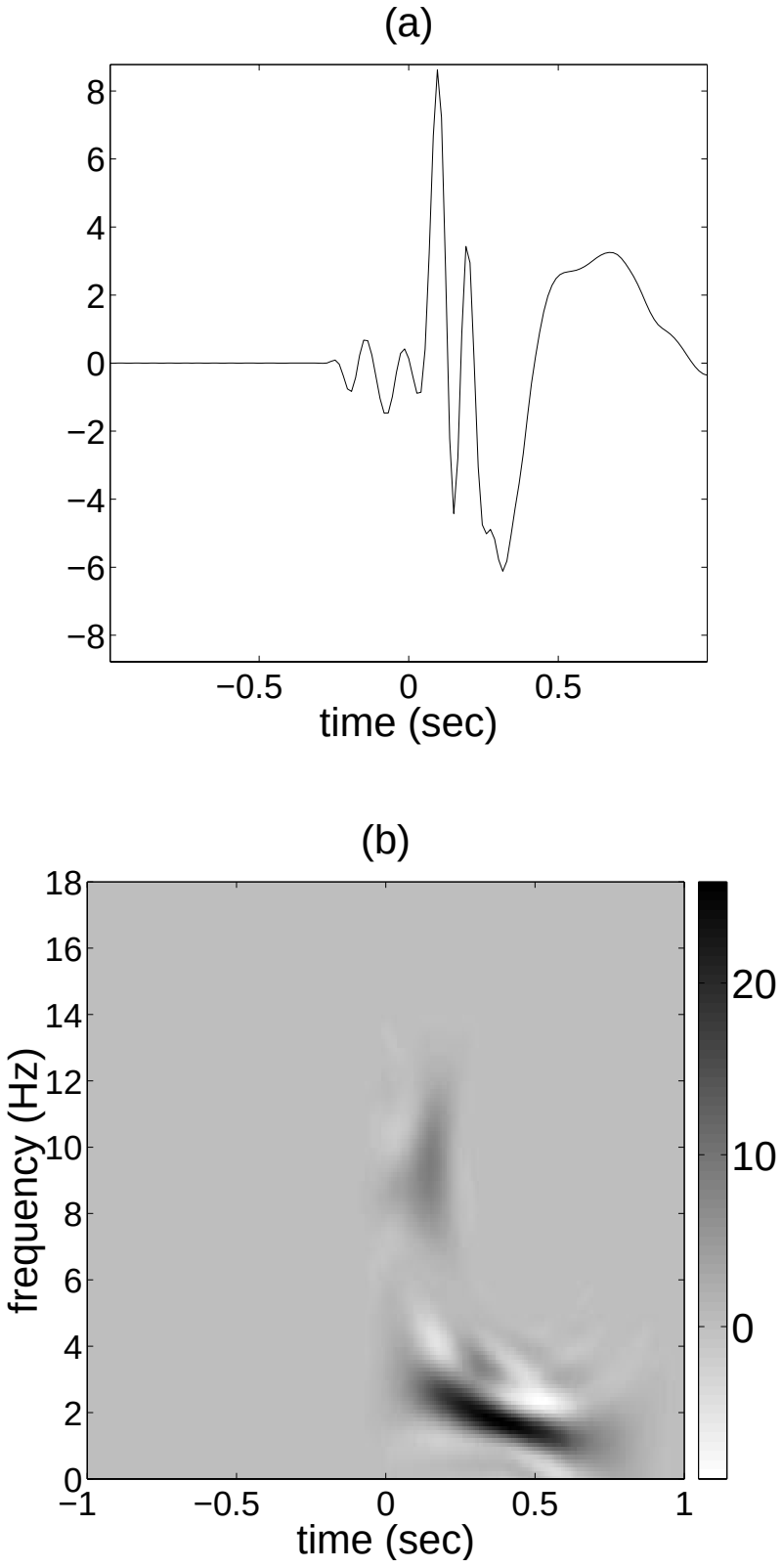

Figure 6.30: (a) The sum of the extracted components shown in Fig. 6.28(a) and Fig. 6.29(a) provides a very clear representation for the signal term in the recorded frame given in Fig. 6.27(a). The high resolution cross–term free time–frequency distribution of this signal computed by using TFCA is given in (b). The distribution of the composite signal is obtained by summing the distributions of the individual components given in Fig. 6.28(b) and Fig. 6.29(b).

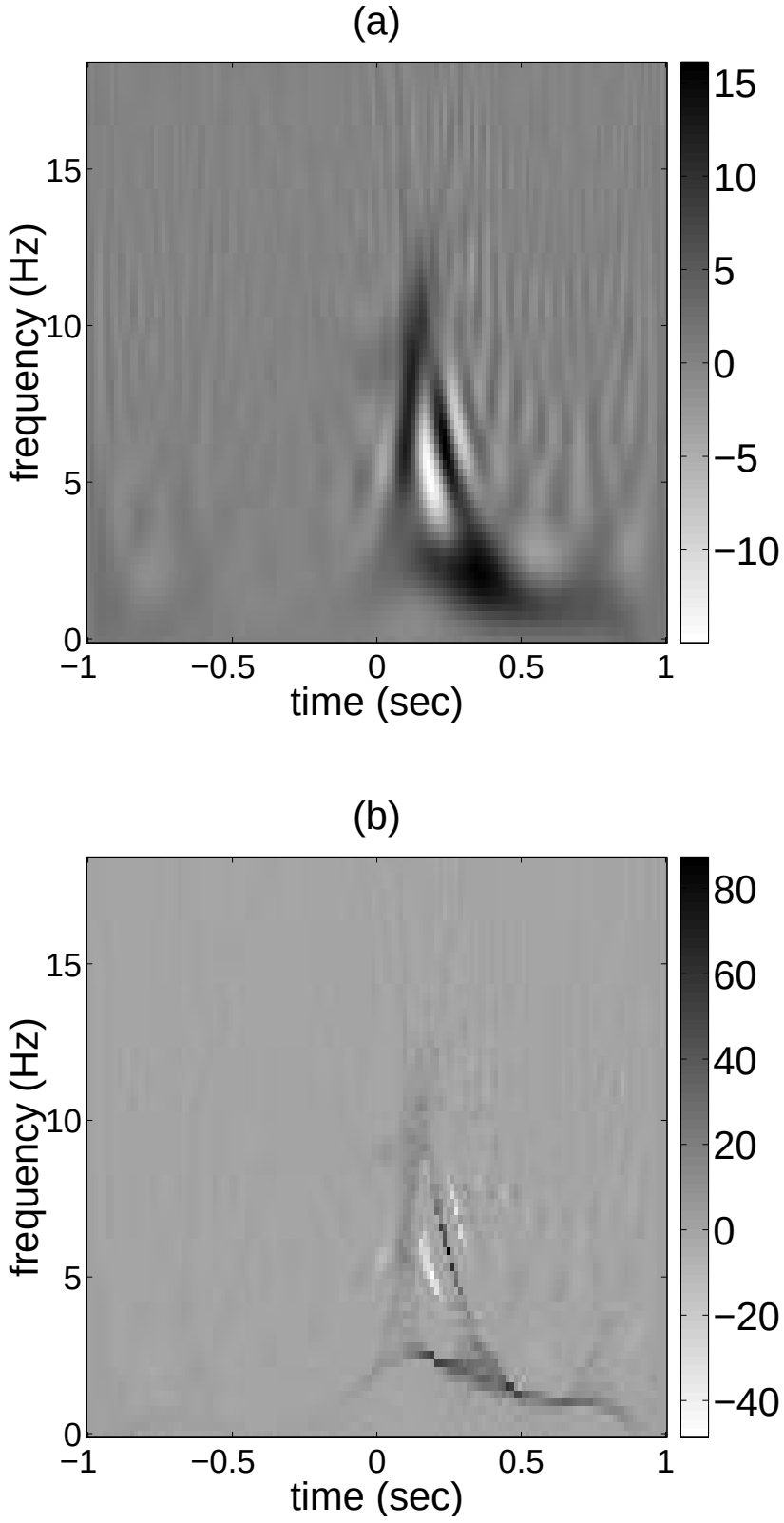

Figure 6.31: The TFDs of the recorded frame shown in Fig. 6.27(a) computed by using (a) PWD and (b) reassigned PWD techniques, respectively.

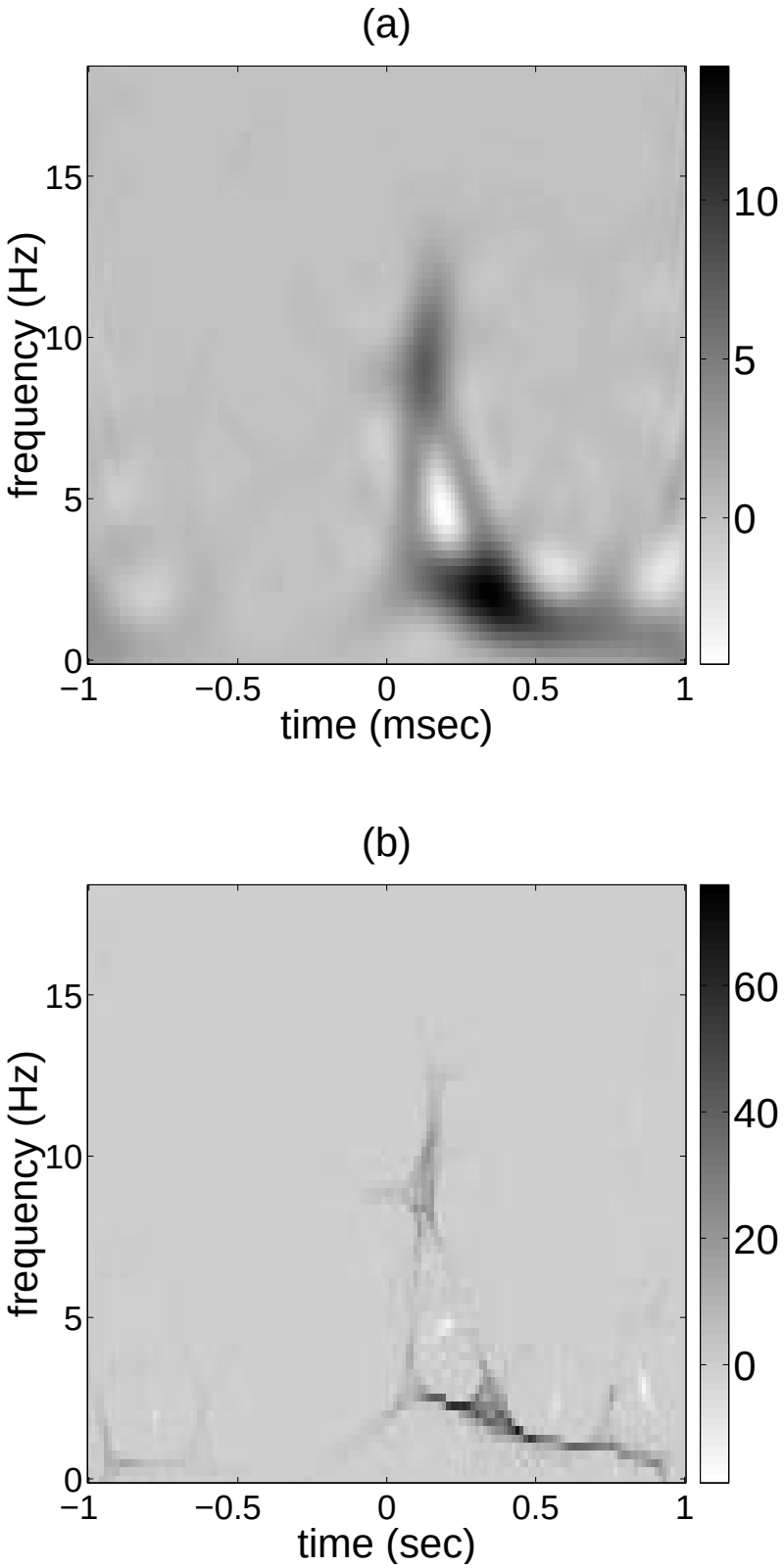

Figure 6.32: The TFDs of the recorded frame shown in Fig. 6.27(a) computed by using (a) SPWD and (b) reassigned SPWD techniques, respectively.

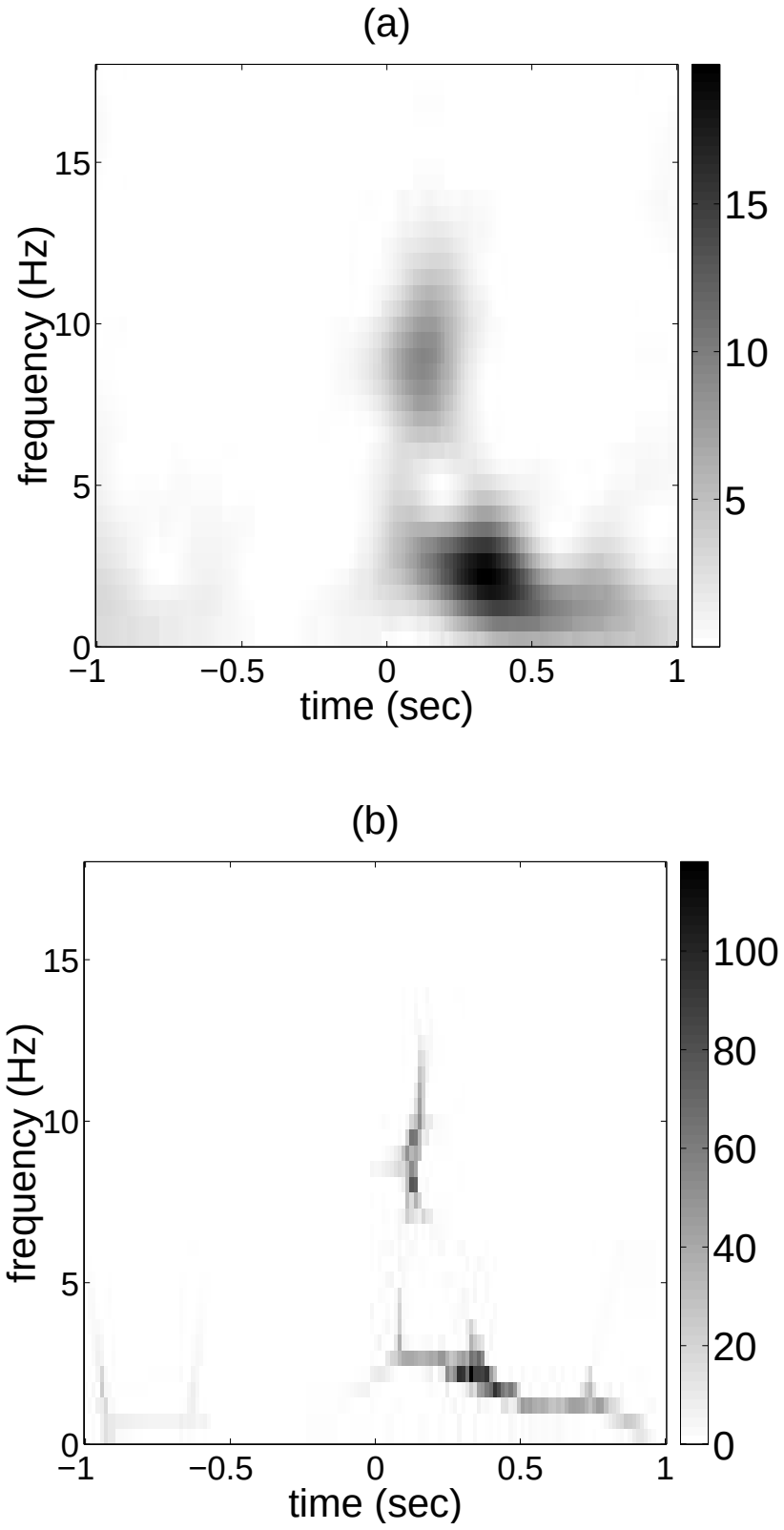

Figure 6.33: The TFDs of the recorded frame shown in Fig. 6.27(a) computed by using (a) spectrogram and (b) reassigned spectrogram techniques, respectively.

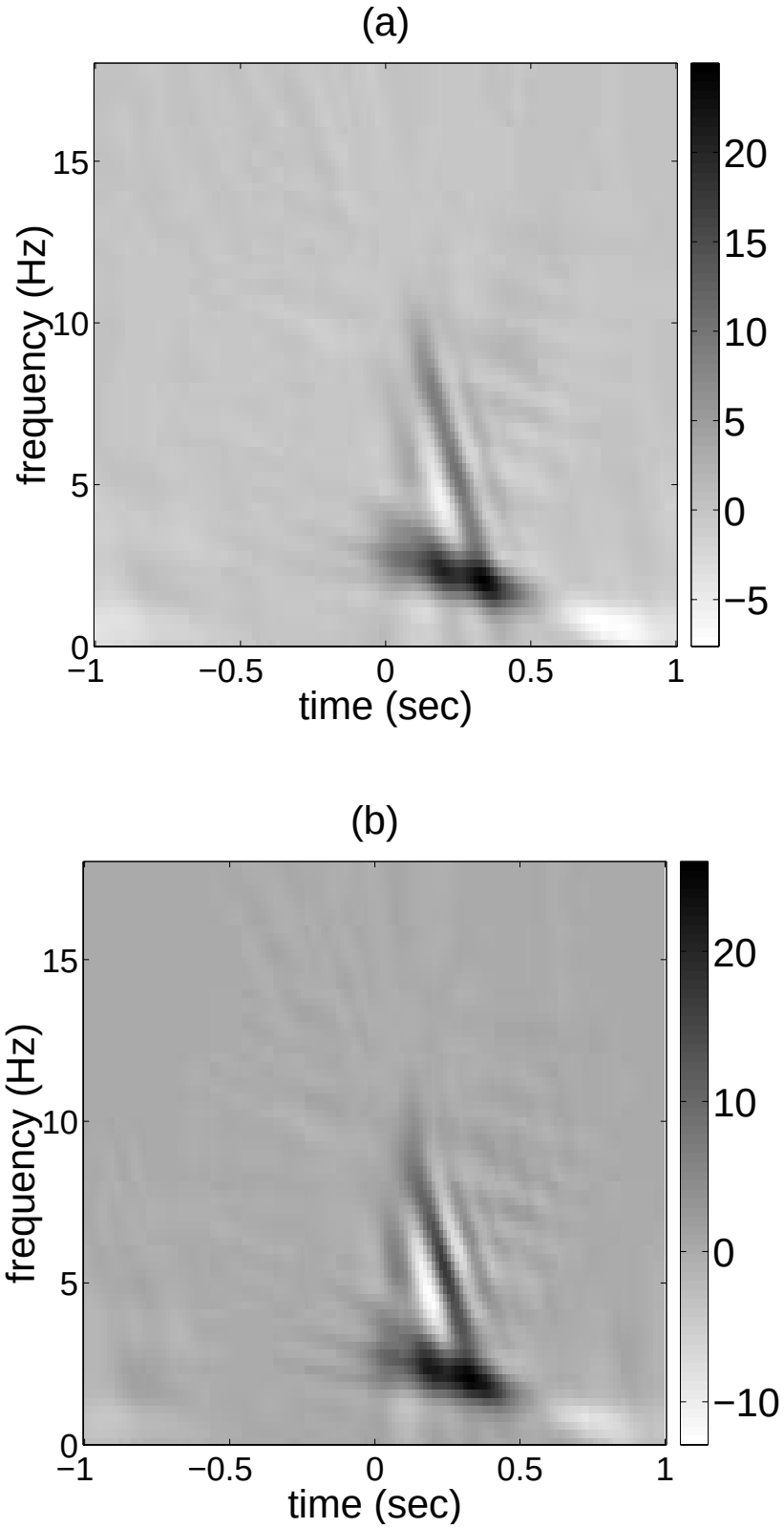

Figure 6.34: The TFDs of the recorded frame shown in Fig. 6.27(a) computed by using the optimal radially Gaussian kernel technique. In (a) and (b) the volume parameter used in ORGK was chosen as $\alpha = 3$ and $\alpha = 5$, respectively.

Chapter 7

Conclusions and Future Work

In this thesis, the TFCA is introduced to conduct the time–frequency analysis of multi–component signals with localized time–frequency supports. The TFCA is an almost automated algorithm and it provides signal–dependent time–frequency representation of the individual signal components of a composite signal. In addition, it performs the extraction of the identified components from the composite signal, as well. The TFCA is based on important theoretical results which are derived in this thesis and partially published in a series of papers [47–52]. The fast Wigner slice and ambiguity slice computation algorithms derived in Chapter 3, the fast directional filtering algorithm derived in Chapter 4, the fast warping based analysis algorithm derived in Chapter 5 and the fast fractional domain incision algorithm presented in Chapter 6 play key roles in the success of the TFCA. Based on a synthetic data simulation, the superiority of the proposed method to some well known and widely used techniques is shown both qualitatively and quantitatively. Based on real data simulations, it is shown that the proposed iterative algorithm provides significantly better estimates of the time–frequency representations for the individual signal components and the composite signal, compared to some well–known techniques. In conclusion, the TFCA is a powerful and flexible new time–frequency analysis technique which is very useful in the analysis of multi–component signals.

Future work on the TFCA can be focused on analyzing multi–component signals with overlapping components in the time–frequency plane.

Appendix A

Relation Between the Radon–Ambiguity Function Transformation and the Fractional Fourier Transformation

The relationship of the RWT to the FrFT is well known in the literature. In this section, we show that a similar relationship exists between the RAFT and FrFT. We start with the substitution of (2.4b) into (3.18) resulting in the following expression for the radial slice of the RAFT:

$$\begin{aligned} \mathcal{RDN}\,[A_y](r,\phi) &= \iint y(t+\tau/2)y^*(t-\tau/2)e^{\jmath 2\pi\nu t}\Big|_{\substack{\nu=r\cos\phi-s\sin\phi\\ \tau=r\sin\phi+s\cos\phi}}\,\mathrm{d}t\,\mathrm{d}s \quad \text{(A.1a)}\\ &= \iint y(t+\frac{r\sin\phi+s\cos\phi}{2})y^*(t-\frac{r\sin\phi+s\cos\phi}{2})\\ &\qquad \times e^{\jmath 2\pi(r\cos\phi-s\sin\phi)t}\,\mathrm{d}t\,\mathrm{d}s\ . \quad \text{(A.1b)} \end{aligned}$$

By making the following change in the integration variables:

$$\begin{bmatrix} t_1\\ t_2 \end{bmatrix} = \begin{bmatrix} 1 & +\frac{1}{2}\cos\phi\\ 1 & -\frac{1}{2}\cos\phi \end{bmatrix}\begin{bmatrix} t\\ s \end{bmatrix} + \frac{1}{2}r\sin\phi\begin{bmatrix} 1\\ -1 \end{bmatrix} \quad \text{(A.2)}$$

$$\mathrm{d}t_1\,\mathrm{d}t_2 = |\cos\phi|\,\mathrm{d}t\,\mathrm{d}s\ , \quad \text{(A.3)}$$

the integral in (A.1b) can be written as in the following separable form:

$$\mathcal{RDN}\,[A_y](r,\phi) = \iint y(t_1)y^*(t_2)e^{\jmath\pi[-(t_1^2-t_2^2)\tan\phi+(t_1+t_2)r\sec\phi]}\frac{1}{|\cos\phi|}\,\mathrm{d}t_1\,\mathrm{d}t_2\ . \quad \text{(A.4)}$$

By using the definition of A_ϕ given in (2.9), it follows that $1/|\cos\phi| = |A_{\phi-\pi/2}e^{-\jmath\pi(r/2)^2\tan\phi}|^2$. After substituting this identity into (A.4), the separated terms can be written in the form of FrFT:

$$\begin{aligned}
\mathcal{R}DN\ [A]_y(r,\phi) &= \left[\int A_{\phi-\pi/2}e^{\jmath\pi(-(r/2)^2\tan\phi+rt_1\sec\phi-t_1^2\tan\phi)}y(t_1)\,\mathrm{d}t_1\right] \\
&\quad \left[\int A_{\phi-\pi/2}e^{-\jmath\pi((r/2)^2\tan\phi+rt_2\sec\phi+t_2^2\tan\phi)}y(t_2)\,\mathrm{d}t_2\right]^* \qquad \text{(A.5a)} \\
&= \left[\{\mathcal{F}^{(a-1)}\ y\}(r/2)\right]\left[\{\mathcal{F}^{(a-1)}\ y\}(-r/2)\right]^* \qquad \text{(A.5b)} \\
&= y_{(a-1)}(r/2)y^*_{(a-1)}(-r/2)\ , \qquad \text{(A.5c)}
\end{aligned}$$

where $(a-1) = (2/\pi)\phi - 1$ is the FrFT order.

Thus we have found a simple closed form expression for the Radon transformation of the ambiguity function $A_y(\nu,\tau)$ in terms of the FrFT of the signal $y(t)$. When the signal $y(t)$ given in (A.5) is the translated version of a signal $x(t)$ in time and frequency as in (4.2), the RAFT of $y(t)$ can be also expressed in terms of the input signal $x(t)$. To derive this result, first we obtain the FrFT of $y(t)$ by using the basic properties of the FrFT [99]:

$$y_{(a-1)}(t) = Ce^{\jmath\varphi(t)}x_{(a-1)}(t + t_o\sin\phi - f_o\cos\phi)\ , \qquad \text{(A.6)}$$

where $\varphi(t) = -2\pi t(f_o\sin\phi + t_o\cos\phi)$ is the linear phase factor and $C = exp(\jmath\pi\cos\phi(f_o^2\sin\phi + t_o^2\cos\phi + f_o t_o\sin\phi))$ is a unit magnitude complex constant. Since we have the freedom to choose (t_o, f_o) as any point which lies on the line L_{W_x} shown in Fig. 4.2, we use this freedom to simplify the expression for the FrFT of $y(t)$. By choosing $(t_o, f_o) \triangleq (d\sin\phi, -d\cos\phi)$ as the closest point on L_{W_x} to the origin (see Fig. 4.2) we simplify (A.6) as

$$y_{(a-1)}(t) = Cx_{(a-1)}(t+d)\ . \qquad \text{(A.7)}$$

Finally by substituting this relation into (A.5), we obtain the desired expression for the RAFT of $y(t)$:

$$\mathcal{R}DN\ [A_y](r,\phi) = x_{(a-1)}(\frac{r}{2}+d)\,x^*_{(a-1)}(-\frac{r}{2}+d)\ . \qquad \text{(A.8)}$$

Appendix B

Fast Algorithms

In this appendix, the tabulated steps of the algorithms used or developed in this proposal are given for ease in their implementation. In Appendix B.1 the fast fractional Fourier transform algorithm given in [85], in Appendix B.2 and Appendix B.3 the algorithms used for fast computation of the cross–ambiguity function and the cross Wigner distribution on arbitrary line segments developed in [49], [50] and Chapter 3, in Appendix B.4 a modified version of the algorithm given in [85] and finally in Appendix B.5 the full version of the Time–Frequency Component Analyzer algorithm developed in this thesis and in [47], [48] are summarized.

B.1 The Fast Fractional Fourier Transform Algorithm

Algorithm 2 The Fast Fractional Fourier Transform Algorithm proposed in [85]

Object of the algorithm:

Given $f(n/\Delta_x)$, $-N/2 \leq n \leq N/2-1$, to compute $f_a(m/2\Delta_x)$, $-N \leq m \leq N-1$, under the assumption that the WD of $f(t)$ is confined into a circle with diameter $\Delta_x \leq \sqrt{N}$.

Steps of the algorithm:

Interpolate the input samples by 2: $f(n/\Delta_x) \rightarrow f(n/2\Delta_x)$

$a' := (a+2 \mod 4) - 2$ % After the modulo operation, $a' \in [-2,\ 2)$

% The cases of $|a'| \in [0.5,\ 1.5]$ and $a' \in \{[-2,\ -0.5)U(0.5,\ 2)\}$ have to be treated separately.

if $|a'| \in [0.5,\ 1.5]$ **then**

$a'' := a'$

else

$a'' := (a'+1 \mod 4) - 2$ % After the modulo operation, $a'' \in (0.5,\ 1.5)$

end if

$\phi'' := \frac{\pi}{2} a''$

$\alpha'' := \cot \phi''$

$\beta'' := \csc \phi''$

$A_{\phi''} := \frac{\exp(-j\pi\, \mathrm{sgn}(\sin\phi'')/4 + j\phi''/2)}{|\sin\phi''|^{1/2}}$

% Compute the following sequences:

$c_1[m] := e^{\jmath\pi\frac{1}{4}(\alpha''/\Delta_x^2 - \beta''/N)m^2}$ for $-N \leq m \leq N-1$

$c_2[m] := e^{\jmath\pi\beta''(m/2\sqrt{N})^2}$ for $-2N \leq m \leq 2N-1$

$c_3[m] := e^{\jmath\pi\frac{\Delta_x^2}{4N}(\alpha''/N - \beta''/\Delta_x^2)m^2}$ for $-N \leq m \leq N-1$

$g[m] := c_1[m] f(m/2\Delta_x)$ for $-N \leq m \leq N-1$

$h_{a''}(m/2\Delta_x) := \frac{A_{\phi''}}{2\Delta_x} c_3[m](c_2 * g)[m]$ for $-N \leq m \leq N-1$

%In the last step FFT is used to compute the convolution in $O(N \log N)$ flops.

if $|a'| \in [0.5,\ 1.5]$ **then**

$f_a(m/2\Delta_x) := h_{a''}(m/2\Delta_x)$

else

% Compute samples of the ordinary FT using FFT.

$f_a(m/2\Delta_x) := \{\mathcal{F}^1\, h_{a''}\}(m/2\Delta_x)$

end if

B.2 The Fast Computation of the Cross–Ambiguity Function on Arbitrary Line Segments

Algorithm 3 The Fast Ambiguity–slice Computation Algorithm

Object of the algorithm:

Given $y(n/\Delta_x)$ and $z(n/\Delta_x)$, $-N/2 \leq n \leq N/2-1$, to compute N' samples of the cross AF of $y(t)$ and $z(t)$ along the line segment L_A as shown in Fig. 3.3.

Steps of the algorithm:

if a radial slice **then**

$y_a[n] := \{\mathcal{F}^a\, y\}(n/2\Delta_x)$ for $-N \leq n \leq N-1$ by using Algorithm 2.

$z_a[n] := \{\mathcal{F}^a\, z\}(n/2\Delta_x)$ for $-N \leq n \leq N-1$ by using Algorithm 2.

$p_a[n] := y_a[n]z_a^*[n]$ for $-N \leq n \leq N-1$

else

$\tilde{y}[n] := y(n/\Delta_x + \tau_o/2)e^{\jmath\pi\nu_o(n/\Delta_x)}$ for $-N/2 \leq n \leq N/2-1$

$\tilde{z}[n] := z(n/\Delta_x - \tau_o/2)e^{-\jmath\pi\nu_o(n/\Delta_x)}$ for $-N/2 \leq n \leq N/2-1$

$\tilde{y}_a[n] := \{\mathcal{F}^a\, \tilde{y}\}(n/2\Delta_x)$ for $-N \leq n \leq N-1$ by using Algorithm 2.

$\tilde{z}_a[n] := \{\mathcal{F}^a\, \tilde{z}\}(n/2\Delta_x)$ for $-N \leq n \leq N-1$ by using Algorithm 2.

$p_a[n] := y_a[n]z_a^*[n]$ for $-N \leq n \leq N-1$

end if

$$A_{yz}(\nu_k, \tau_k) := \frac{1}{2\Delta_x} \sum_{n=-N}^{N-1} p_a[n] e^{\jmath \frac{\pi}{\Delta_x}\lambda_k n} \quad \text{for } 0 \leq k \leq N'-1 \quad \text{by using the CZT Algorithm.}$$

where $(\nu_k, \tau_k) \triangleq (\nu_o + \lambda_k \cos\phi, \tau_o + \lambda_k \sin\phi)$ and $\lambda_k \triangleq \lambda_i + k\frac{\lambda_f - \lambda_i}{N'-1}$.

B.3 The Fast Computation of the Cross–Wigner Distribution on Arbitrary Line Segments

Algorithm 4 The Fast Wigner–Slice Computation Algorithm

Object of the algorithm:

Given $y(n/\Delta_x)$ and $z(n/\Delta_x)$, $-N/2 \leq n \leq N/2-1$, to compute N' samples of the cross WD of $y(t)$ and $z(t)$ along the line segment L_W as parameterized in (3.21).

Steps of the algorithm:

if a radial slice **then**

$y_{(a-1)}[n] := \{\mathcal{F}^{(a-1)}\, y\}(n/2\Delta_x)$ for $-N \leq n \leq N-1$ by using Algorithm 2.

$z_{(a-1)}[n] := \{\mathcal{F}^{(a-1)}\, z\}(n/2\Delta_x)$ for $-N \leq n \leq N-1$ by using Algorithm 2.

$q_{(a-1)}[n] := y_{(a-1)}[n] z^*_{(a-1)}[-n]$ for $-N \leq n \leq N-1$

else

$\tilde{y}[n] := y(n/\Delta_x + t_o) e^{-\jmath 2\pi f_o (n/\Delta_x)}$

$\tilde{z}[n] := z(n/\Delta_x + t_o) e^{-\jmath 2\pi f_o (n/\Delta_x)}$

$\tilde{y}_{(a-1)}[n] := \{\mathcal{F}^{(a-1)}\, \tilde{y}\}(n/2\Delta_x)$ for $-N \leq n \leq N-1$ by using Algorithm 2.

$\tilde{z}_{(a-1)}[n] := \{\mathcal{F}^{(a-1)}\, \tilde{z}\}(n/2\Delta_x)$ for $-N \leq n \leq N-1$ by using Algorithm 2.

$q_{(a-1)}[n] := \tilde{y}_{(a-1)}[n] \tilde{z}^*_{(a-1)}[-n]$ for $-N \leq n \leq N-1$

end if

$$W_{yz}(t_k, f_k) := \frac{1}{\Delta_x} \sum_{n=-N}^{N-1} q_{a-1}[n] e^{-\jmath \frac{2\pi}{\Delta_x} \lambda_k n}$$ for $0 \leq k \leq N'-1$ by using the CZT Algorithm.

where $(t_k, f_k) \triangleq (t_o + \lambda_k \cos\phi, f_o + \lambda_k \sin\phi)$ and $\lambda_k \triangleq \lambda_i + k\frac{\lambda_f - \lambda_i}{N'-1}$.

B.4 The Modified Fast Fractional Fourier Transform Algorithm

Algorithm 5 The Modified Fast Fractional Fourier Transform Algorithm

Object of the algorithm:

Given $x(n/\Delta_x)$, $-N/2 \le n \le N/2-1$, to compute $x_a(m\Delta_x/(2N)+d)$, $-N \le m \le N-1$. It is assumed that $x(t)$ is scaled before obtaining its samples so that its WD is confined into a circle with diameter $\Delta_x \le \sqrt{N}$ [85]. This algorithm is obtained by modifying the algorithm in [85] to incorporate the delay term d, and removing the condition that the time–bandwidth product of $x(t)$ be integer.

Steps of the algorithm:

Interpolate the input samples by 2:

$a' := (a+2 \mod 4) - 2$ % After the modulo operation, $a' \in [-2,\ 2)$

if $|a'| \in [0.5,\ 1.5]$ **then**

$a'' := a'$

else

$a'' := (a'+1 \mod 4) - 2$ % After the modulo operation, $a' \in (0.5,\ 1.5)$

end if

$\phi'' := \frac{\pi}{2} a''$

$\alpha'' := \cot \phi''$

$\beta'' := \csc \phi''$

$A_{\phi''} := \frac{\exp(-j\pi \operatorname{sgn}(\sin\phi'')/4 + j\phi''/2)}{|\sin\phi''|^{1/2}}$

% Compute the following sequences:

$c_1[m] := e^{\jmath\pi[(\frac{\alpha}{4\Delta_x^2} - \frac{\beta}{4N})m^2 - \frac{\beta d}{\Delta_x} m]}$ for $-N \le m \le N-1$

$c_2[m] := e^{\jmath\pi \frac{\beta}{4N} m^2}$ for $-2N \le m \le 2N-1$

$c_3[m] := e^{\jmath\pi[\alpha(\frac{\Delta_x}{2N} m + d)^2 - \frac{\beta}{4N} m^2]}$ for $-N \le m \le N-1$

$g[m] := c_1[m]\, x(m/2\Delta_x)$ for $-N \le m \le N-1$

$h_{a''}(m\Delta_x/(2N)) := \frac{A_\phi}{2\Delta_x} c_3[m]\, (c_2 * g)[m]$ for $-N \le m \le N-1$

%In the last step FFT is used to compute the convolution in $O(N \log N)$ flops.

if $|a'| \in [0.5,\ 1.5]$ **then**

$x_a(m\Delta_x/(2N) + d) := h_{a''}(m\Delta_x/(2N))$

else

% Compute samples of the ordinary FT using FFT.

$x_a(m\Delta_x/2N + d) := \{\mathcal{F}^1\, h_{a''}\}(m\Delta_x/(2N) + d)$

end if

B.5 The Time–Frequency Component Analyzer

Algorithm 6 The Time–Frequency Component Analyzer

Object of the algorithm:

Given a multi–component $x(n/\Delta_x)$, $-N/2 \leq n \leq N/2-1$, to extract its components and compute its time–frequency distribution. It is assumed that $x(t)$ is scaled before obtaining its samples so that its WD is confined into a circle with diameter $\Delta_x \leq \sqrt{N}$ [85].

Steps of the algorithm:

1. Initialize the residual signal and iteration number as $r^0(t) := x(t)$, $i := 1$, respectively.
2. Identify the time–frequency support of the component $s_i(t)$ by using the watershed segmentation algorithm [3], appropriate rotation angle ϕ_i, fractional domain $a_i = 2\phi_i/\pi$, the spine $\psi_{i,a_i}(t)$ of the fractional Fourier transformed signal $x_{a_i}(t)$ by using an instantaneous frequency estimation algorithm, and the amount of required frequency shift δ_{f_i} on the spine $\psi_{i,a_i}(t)$.
3. Compute FrFT samples $r_{a_i}^{i-1}(kT)$, $a_i = 2\phi_i/\pi$, from the samples of $r^{i-1}(kT)$ by using the Algorithm 2.
4. Define the warping function $\zeta_i(t) = \Gamma_i^{-1}(f_{\psi_i}(t-t_1))$, where $\Gamma_i(t) = \int_{t_1}^{t}[\psi_{a_i}(t') + \delta_{f_i}]\,\mathrm{d}t'$ and $f_{\psi_i} = \Gamma_i(t_N)/(t_N - t_1)$. Compute the time samples $\zeta_i(kT)$ of the warping function.
5. Compute the samples $r_{a_i,\zeta_i}^{i-1}(kT)$ of the warped signal as

$$\begin{aligned} r_{a_i}^{i-1,\delta_{f_i}}(kT) &:= e^{\jmath 2\pi\delta_{f_i}kT} r_{a_i}^{i-1}(kT) \\ r_{a_i,\zeta_i}^{i-1,\delta_{f_i}}(kT) &:= e^{-\jmath 2\pi\delta_{f_i}kT} \;\; r_{a_i}^{i-1,\delta_{f_i}}(\zeta_i(kT)) \;\; . \end{aligned}$$

6. Estimate the i^{th} component by time–frequency domain incision as

$$\hat{s}_{a_i,\zeta}^{i,\delta_{f_i}}(t) = h_2(t)[h_1(t) * r_{a_i,\zeta_i}^{i-1,\delta_{f_i}}(t)] \;\; ,$$

where $h_2(t)$ is a time–domain mask and $h_1(t)$ is the inverse Fourier transform of a frequency domain mask $H_1(f)$.

for Each TFD slice of $s^i(t)$ to be computed, after choosing the slice offset Δ_ψ **do**

7. Compute $y_{a_i,\zeta_i}(kT) = \hat{s}^{i,\delta_{f_i}}_{a_i,\zeta_i}(kT)e^{\jmath 2\pi\Delta_\psi\zeta(kT)}$.

8. Compute the samples of the TFD $\mathcal{H}_{y_{a_i,\zeta_i}}(m\bar{T}, f_{\psi_i})$, $t_1/\bar{T} \leq m \leq t_N/\bar{T}$ of $y_{a_i,\zeta_i}(t)$ by using the directional smoothing algorithm fully presented in [51] and summarized in Algorithm 1, where $\bar{T}$ is the sampling interval of the TFD slice.

9. The TFD slice of $s^i(t)$ is given by

$$\mathcal{H}_{s^i}(t_r(m\bar{T}), f_r(m\bar{T})) = \mathcal{H}_{y_{a,\zeta}}(m\bar{T}, f_\psi) \ ,$$

where $(t_r(m\bar{T}), f_r(m\bar{T}))$ defines a curve in the time–frequency plane parameterized with the variable $m\bar{T}$:

$$\begin{aligned} t_r(m\bar{T}) &= \zeta(m\bar{T})\cos(\frac{a\pi}{2}) - (\psi(\zeta(m\bar{T})) + \Delta_\psi)\sin(\frac{a\pi}{2}) \\ f_r(m\bar{T}) &= \zeta(m\bar{T})\sin(\frac{a\pi}{2}) + (\psi(\zeta(m\bar{T})) + \Delta_\psi)\cos(\frac{a\pi}{2}) \ , \end{aligned}$$

and $t_1/\bar{T} \leq m \leq t_N/\bar{T}$.

end for

10. Estimate samples $s^i(t)$ by inverting the warping, frequency modulation and the fractional Fourier transformation operations on samples of $\hat{s}^{\delta_f}_{a_i,\zeta}(t)$:

$$\begin{aligned} \hat{s}^{i,\delta_{f_i}}_a(kT) &:= e^{\jmath 2\pi\delta_{f_i}\zeta_i^{-1}(kT)} \ \hat{s}^{i,\delta_{f_i}}_{a_i,\zeta_i}(\zeta_i^{-1}(kT)) \\ \hat{s}^i_{a_i}(kT) &:= e^{-\jmath 2\pi\delta_{f_i}kT} \ \hat{s}^{1,\delta_{f_i}}_{a_i}(kT) \\ \hat{s}^i(kT) &:= \{\mathcal{F}^{(-a_i)} \ \hat{s}^i_{a_i}\}(kT) \ . \end{aligned}$$

11. Compute the residual signal $r^i(kT) = r^{i-1} - \hat{s}^i(t)$.

if any signal component is left in residual signal $r^i(kT)$ **then**

Set $i = i + 1$, and **GOTO** step 2,

else

Compute the t–f distribution of the composite signal by summing the t–f distributions of individual signal components.

end if

Bibliography

[1] S. M. Sussman, "Least–squares synthesis of radar ambiguity functions," *IRE Trans. Inform. Theory*, vol. IT–8, pp. 246–254, Apr. 1962.

[2] T. A. C. M. Claasen and W. F. G. Mecklenbräuker, "The Wigner distribution – A tool for time–time frequency signal analysis, Part II: Discrete–time signals," *Philips J. Res.*, vol. 35, no. 4/5, pp. 276–350, 1980.

[3] L. Vincent and P. Soille, "Watersheds in digital spaces: An efficient algorithm based on immersion simulations," *IEEE Trans. on Pattern Analysis and Machine Intelligence*, vol. 13, no. 6, pp. 583–598, June 1991.

[4] "http://www.dsp.rice.edu/software/TFA/RGK/BAT/batsig.bin.Z," .

[5] Sirel Karakaş, Emine D. Çakmak, D. İlhan Tüfekçi, Ahmet Kemal Özdemir, and Orhan Arıkan, "A new algorithm for demonstrating oscillatory responses of the brain: Time-frequency component analyzer," will be submitted to *Elsevier Journal of Neuroscience Methods*, 2003.

[6] L. Cohen, "Time–frequency distributions – A review," *Proc. IEEE*, vol. 77, no. 7, pp. 941–981, July 1989.

[7] F. Hlawatsch and G. F. Boudreaux-Bartels, "Linear and quadratic time–frequency signal representations," *IEEE Signal Processing Magazine*, vol. 9, no. 4, pp. 21–67, Apr. 1992.

[8] S. Krishnan R. M. Rangayyan, "Comparative analysis of the performance of the time–frequency distributions with knee joint vibroart hrographic signals," *IEEE-SP Int. Sym. Time-Fre. Time–Scale Anal.*, pp. 273–276, Oct. 1998.

[9] O. A. Ahmed and M. M. Fahmy, "Nmr signal enhancement via a new time–frequency transform," *IEEE Trans. Med. Imag*, vol. 20, pp. 1018–1025, Oct. 1998.

[10] B. Boashash and P. 'Shea, "Time-frequency analysis applied to signaturing of underwater acoustic signals," *Proc. IEEE Int. Conf. Acoust. Speech Signal Process.*, pp. 2817 – 2820, Apr. 1988.

[11] S. B. Suppappola S. Pon Varma, A. Papandreou-Suppappola, "Detecting faults in structures using time–frequency techniques," *Proc. IEEE Int. Conf. Acoust. Speech Signal Process.*, pp. 3593 – 3596, May 2001.

[12] C. Rivero-Moreno and B. Escalante-Ramirez, "Seismic signal detection with time–frequency models," *IEEE-SP Int. Sym. Time-Fre. Time–Scale Anal.*, pp. 345–348, June 1996.

[13] R. G. Baraniuk, M. Coates, and P. Steeghs, "Hybrid linear/quadratic time–frequency attributes," *IEEE Trans. Signal Process.*, vol. 49, pp. 760–766, Apr. 2001.

[14] B. H. Juang J. W. Pitton, K. Wang, "Time–frequency analysis and auditory modeling for automatic recognition of speech," *Proc. IEEE*, vol. 84, pp. 1199–1214, Sept. 1996.

[15] A. Potamianos and P. Maragos, "Time-frequency distributions for automatic speech recognition," *IEEE Trans. Speech Audio Processing*, vol. 9, pp. 196–200, Mar. 2001.

[16] A. M. Sayeed and D. L. Jones, "Optimal detection using bilinear time-frequency and time-scale representations," *IEEE Trans. Signal Process.*, vol. 43, pp. 2872–2883, Dec. 1995.

[17] V. C. Chen and H. Ling, "Joint time–frequency analysis for radar signal and image processing," *IEEE Signal Processing Magazine*, vol. 16, pp. 81–93, Mar. 1999.

[18] Y. Shi and X. Zhang, "A gabor atom network for signal classification with application in radar target recognition," *IEEE Trans. Signal Process.*, vol. 49, pp. 2994–3004, Dec. 2001.

[19] N. Ma and D. Vray, "Bottom backscattering coefficient estimation from wideband chirp sonar echoes by chirp adapted time-frequency representation," *Proc. IEEE Int. Conf. Acoust. Speech Signal Process.*, pp. 2461–2464, May 1998.

[20] T. A. C. M. Claasen and W. F. G. Mecklenbräuker, "The Wigner distribution – A tool for time–time frequency signal analysis, Part I: Continuous–time signals," *Philips J. Res.*, vol. 35, no. 3, pp. 217–250, 1980.

[21] T. A. C. M. Claasen and W. F. G. Mecklenbräuker, "The Wigner distribution – A tool for time–time frequency signal analysis, Part III: Rrelations with other time–frequency signal transformations," *Philips J. Res.*, vol. 35, no. 6, pp. 372–389, 1980.

[22] D. L. Jones and T. W. Parks, "A resolution comparison of several time–frequency representations," *IEEE Trans. Signal Process.*, vol. 40, no. 2, pp. 413–420, Feb. 1992.

[23] F. Hlawatsch and P. Flandrin, "The interference structure of the Wigner distribution and related time-frequency signal representations," in *The Wigner Distribution — Theory and Applications in Signal Processing*, W. Mecklenbräuker and F. Hlawatsch, Eds., pp. 59–133. Elsevier, Amsterdam, The Netherlands, 1997.

[24] L. Cohen, *Time–frequency analysis*, Prentice Hall, 1995.

[25] P. M. Woodward, *Probability and Information Theory, with Applications to Radar*, New York: Pergamon Press Inc., 1953.

[26] C. H. Wilcox, "The synthesis problem for radar ambiguity functions," MRC Technical Summary Report 157, Apr. 1960.

[27] R. E. Blahut, W. Miller, and Jr. C. H. Wilcox, *Radar and Sonar*, vol. 32, Springer–Verlag, 1991.

[28] C. H. Page, "Instantaneous power spectra," *J. Appl. Phys.*, vol. 23, pp. 103–106, 1952.

[29] H. Mergenau and R. N. Hill, "Correlation between measurements in quantum theory," *Prog. Theor. Phys.*, vol. 26, pp. 722–738, 1961.

[30] W. Rihaczek, "Signal energy distribution in time and frequency," *IEEE Trans. Information Theory*, vol. IT-14, pp. 369–374, 1968.

[31] H. I. Choi and W. J. Williams, "Improved time–frequency representation of multicomponent signals using exponential kernels," *IEEE Trans. Acoust., Speech, and Signal Process.*, vol. ASSP–37, pp. 862–871, June 1989.

[32] A. Papandreou and G. F. Boudreaux-Bartels, "Distributions for time frequency analysis: A generalization of Choi–Williams and the Butterworth distributions," *IEEE Trans. Signal Process.*, vol. 5, pp. 181–184, 1992.

[33] B. Ristic and B. Boashash, "Kernel design for time–frequency signal analysis using the Radon transform," *IEEE Trans. Signal Process.*, vol. 41, no. 5, pp. 1996–2008, May 1993.

[34] R. G. Baraniuk and D. L. Jones, "A signal–dependent time–frequency representation: Optimal kernel design," *IEEE Trans. Signal Process.*, vol. 41, no. 4, pp. 1589–1601, Apr. 1993.

[35] R. G. Baraniuk and D. L. Jones, "Signal–dependent time–frequency analysis using a radially gaussian kernel," *Signal Process.*, vol. 32, no. 3, pp. 263–284, June 1993.

[36] R. G. Baraniuk and D. L. Jones, "A signal–dependent time–frequency representation: Fast algorithm for optimal kernel design," *IEEE Trans. Signal Process.*, vol. 42, no. 1, pp. 134–146, Jan. 1994.

[37] R. N. Czerwinski and D. L. Jones, "Adaptive cone–kernel time–frequency analysis," *IEEE Trans. Signal Process.*, vol. 43, no. 7, pp. 1715–1719, July 1995.

[38] M. G. Amin, "Minimum variance time-frequency distribution kernels for signals in additive noise," *IEEE Trans. Signal Process.*, vol. 44, pp. 2352–2356, Sept. 1996.

[39] D. L. Jones and R. G. Baraniuk, "An adaptive optimal–kernel time–frequency representation," *IEEE Trans. Signal Process.*, vol. 43, no. 10, pp. 2361–2371, Oct. 1995.

[40] S. G. Mallat and Z. Zhang, "Matching pursuits with time–frequency dictionaries," *IEEE Trans. Signal Process.*, vol. 41, pp. 3397–3415, Dec. 1993.

[41] Aykut Bultan, "A four–parameter atomic decomposition of chirplets," *IEEE Trans. Signal Process.*, vol. 47, pp. 731–745, Mar. 1999.

[42] H. Zou, Q. Dai, R. Wang, and Y. Li, "Parametric TFR via windowed exponential frequency modulated atoms," *IEEE Signal Processing Lett.*, vol. 8, pp. 140–142, May 2001.

[43] P. R. White and D. M. Lopes, "Time–frequency methods for analyzing structural response data," in *Proc. IEEE Int. Conf. Acoust. Speech Signal Process.*, June 2000, pp. 3878–3881.

[44] K. Kodera, C. de Villedary, and R. Gendrin, "Method for the numerical analysis of time-varying signals," *Phys. Earth Plan. Int.*, pp. 142–150, 1976.

[45] K. Kodera, R. Gendrin, and C. de Villedary, "Time–varying signals with small BT values," *IEEE Trans. Acoust., Speech, and Signal Process.*, vol. 26, pp. 64–76, Feb. 1978.

[46] F. Auger and P. Flandrin, "Improving the readability of time–frequency and time–scale representations by the reassignment method," *IEEE Trans. Signal Process.*, vol. 43, pp. 1068–1089, May 1995.

[47] A. Kemal Özdemir and O. Arıkan, "Time–Frequency Component Analyzer," *IEEE Trans. Signal Process.*, submitted to *IEEE Trans. Signal Process.*, July 2002.

[48] A. Kemal Özdemir, L. Durak, and O. Arıkan, "High resolution time–frequency analysis based on fractional domain warping," *Proc. IEEE Int. Conf. Acoust. Speech Signal Process.*, vol. VI, pp. 3553–3556, May 2001.

[49] A. Kemal Özdemir and O. Arıkan, "Efficient computation of the ambiguity function and the Wigner distribution on arbitrary line segments," *IEEE Trans. Signal Process.*, vol. 49, pp. 381–393, Feb. 2001.

[50] A. Kemal Özdemir and O. Arıkan, "Efficient computation of the ambiguity function and the Wigner distribution on arbitrary line segments," *Proc. IEEE Int. Symp. Circuits and Systems*, vol. IV, pp. 171–174, May 1999.

[51] A. Kemal Özdemir and O. Arıkan, "A high resolution time frequency representation with significantly reduced cross–terms," *Proc. IEEE Int. Conf. Acoust. Speech Signal Process.*, vol. II, pp. 693–696, June 2000.

[52] O. Arıkan and A. Kemal Özdemir, "An efficient algorithm to extract components of a composite signal," *Proc. IEEE Int. Conf. Acoust. Speech Signal Process.*, vol. II, pp. 697–700, June 2000.

[53] H. M. Ozaktas and O. Aytur, "Fractional Fourier domains," *Signal Process.*, vol. 46, pp. 119–124, 1995.

[54] G. S. Cunningham and W. J. Williams, "Fast implementations of generalized discrete time–frequency distributions," *IEEE Trans. Signal Process.*, vol. 42, no. 6, pp. 1496–1508, June 1994.

[55] F. Hlawatsch, G. Matz, H. Kirchauer, and W. Kozek, "Time–frequency formulation, design, and implementation of time-varying optimal filters for signal estimation," *IEEE Trans. Signal Process.*, vol. 48, pp. 1417–1432, May 2000.

[56] M. F. Erden, M. A. Kutay, and H. M. Ozaktas, "Repeated filtering in consecutive fractional Fourier domains and its application to signal restoration," *IEEE Trans. Signal Process.*, vol. 47, pp. 1458–1462, May 1999.

[57] M. A. Kutay, H. M. Ozaktas, O. Arikan, and L. Onural, "Optimal filtering in fractional Fourier domains," *IEEE Trans. Signal Process.*, vol. 45, pp. 1129–1143, May 1997.

[58] F. Hlawatsch and W. Kozek, "Time-frequency projection filters and time-frequency signal expansions," *IEEE Trans. Signal Process.*, vol. 42, pp. 3321–3334, May 1994.

[59] F. Hlawatsch, A. H. Costa, and W. Krattenthaler, "Time-frequency signal synthesis with time-frequency extrapolation and don't-care regions," *IEEE Trans. Signal Process.*, vol. 42, pp. 2513–2520, Sept. 1994.

[60] T. J. McHale and G. F. Boudreaux-Bartels, "An algorithm for synthesizing signals from partial time–frequency models using the cross Wigner distribution," *IEEE Trans. Signal Process.*, vol. 41, no. 5, pp. 1986–1990, May 1993.

[61] G. F. Boudreaux-Bartels and T. W. Parks, "Time-varying filtering and signal estimation using wigner distribution synthesis techniques," *IEEE Trans. Acoust., Speech, and Signal Process.*, vol. 34, pp. 442–451, June 1986.

[62] P. Flandrin, "Some features of time–frequency representations of multicomponent signals," *Proc. IEEE Int. Conf. Acoust. Speech Signal Process.*, vol. 3, pp. 41B.4.1–41B.4.4, 1984.

[63] T. A. C. Claasen and W. F. G. Mecklenbräuker, "The aliasing problem in discrete–time Wigner distributions," *IEEE Trans. Acoust., Speech, and Signal Process.*, vol. 31, pp. 1067–1072, Oct. 1983.

[64] V. Namias, "The fractional order Fourier transform and its application to quantum mechanics," *J. Inst. Math. Appl.*, vol. 25, pp. 241–265, 1980.

[65] Haldun M. Ozaktas, Zeev Zalevsky, and M. Alper Kutay, *The Fractional Fourier transform with applications in optics and signal processing*, John Wiley & Sons, 2000.

[66] G. F. Boudreaux-Bartels and T. W. Parks, "Time–varying filtering and signal estimation using Wigner distribution synthesis techniques," *IEEE Trans. Acoust., Speech, and Signal Process.*, vol. ASSP–34, no. 3, pp. 442–451, June 1986.

[67] ed W. F. G. Mecklenbräuker, *The Wigner distribution–theory and applications in signal processing*, Elsevier Science Publishers, 1992.

[68] L. R. Dragonette, D. M. Drumheller, C. F. Gaumond, D. H. Hughes, B. T. O'connor, N. Yen, and T. J. Yoder, "The application of two–dimensional signal transformations to the analysis and synthesis of structural excitations observed in acoustical scattering," *Proc. IEEE*, vol. 84, no. 9, pp. 1249–1263, Sept. 1996.

[69] P. K. Kumar and K. M. M. Prabhu, "Simulation studies of moving–target detection: a new approach with Wigner–Ville distribution," *IEE Proc. Radar. Sonar Navig.*, vol. 144, no. 5, pp. 259–265, Oct. 1997.

[70] S. Haykin and D. J. Thomson, "Signal detection in nonstationary environment reformulated as an adaptive pattern classification problem," *Proc. IEEE*, vol. 86, no. 11, pp. 2325–2344, Nov. 1998.

[71] V. Katkovnik and L. Stankovic, "Instantaneous frequency estimation using the Wigner distribution with varying data–driven window length," *IEEE Trans. Signal Process.*, vol. 46, no. 9, pp. 3215–2325, Sept. 1998.

[72] A. Destefano P. Bonato and R. Ceravolo, "Time–frequency and ambiguity function approaches in structural identification," *J. Engineering Mechanics–Asce*, vol. 123, no. 12, pp. 1260–1267, 1997.

[73] S. Parsons, C. W. Thorpe, and S. M. Dawson, "Echolocation calls of the long–tailed bat - a quantitative analysis of types of calls," *J. Mammology*, vol. 78, no. 3, pp. 946–976, 1997.

[74] G. C. Gaunaurd and H. C. Strifors, "Signal analysis by means of time–frequency (Wigner–type) distributions–applications to sonar and radar echos," *Proc. IEEE*, vol. 84, no. 9, pp. 1231–1248, Sept. 1996.

[75] I. Raveh and D. Mendlovic, "New properties of the Radon transform of the cross Wigner/ambiguity distribution function," *IEEE Trans. Signal Process.*, vol. 47, no. 5, pp. 2077–2080, July 1999.

[76] A. W. Lohmann and B. H. Soffer, "Relationships between the Radon–Wigner and fractional Fourier transforms," *J. Opt. Soc. Am. A*, vol. 11, pp. 1798–1801, 1994.

[77] S. Barbarossa, "Analysis of multicomponent LFM signals by a combined Wigner–Hough transform," *IEEE Trans. Signal Process.*, vol. 43, no. 6, pp. 1511–1515, June 1995.

[78] M. Wang, A. K. Chan, and C. K. Chui, "Linear frequency–modulated signal detection using Radon–ambiguity transform," *IEEE Trans. Signal Process.*, vol. 46, no. 3, pp. 571–586, Mar. 1998.

[79] M. T. Ozgen and K. Demirbas, "Cohen's bilinear class of shift–invariant space/spatial–frequency signal representations for particle–location analysis of in–line Fresnel holograms," *J. Opt. Soc. Am. A*, vol. 15, no. 8, pp. 2117–2137, Aug. 1998.

[80] J. C. Wood and D. T. Barry, "Tomographic time–frequency analysis and its application toward time–varying filtering and adaptive kernel desing for multicomponent linear–FM signals," *IEEE Trans. Signal Process.*, vol. 42, no. 8, pp. 2094–2104, Aug. 1994.

[81] J. C. Wood and D. T. Barry, "Linear sinal synthesis using the Radon–Wigner transform," *IEEE Trans. Signal Process.*, vol. 42, no. 8, pp. 2105–2111, Aug. 1994.

[82] J. C. Wood and D. T. Barry, "Radon transformation of time–frequency distributions for analysis of multicomponent signals," *IEEE Trans. Signal Process.*, vol. 42, no. 8, pp. 3166–3177, Nov. 1994.

[83] Z. Bao, G. Wang, and L. Luo, "Inverse synthetic aperture radar imaging of maneuvering targets," *Opt. Eng.*, vol. 37, no. 5, pp. 1582–1588, May 1998.

[84] R. N. Bracewell, *Two–dimensional imaging*, Prentice–Hall, 1995.

[85] H. M. Ozaktas, O. Arıkan, M. A. Kutay, and G. Bozdagi, "Digital computation of the fractional Fourier transform," *IEEE Trans. Signal Process.*, vol. 44, no. 9, pp. 2141–2150, Sept. 1996.

[86] L. R. Rabiner, R. W. Schafer, and C. M. Rader, "The chirp z–transform algorithm and its applications," *Bell Syst. Tech. J.*, vol. 48, pp. 1249–1292, May 1969.

[87] S. Kay and G. F. Boudreaux-Bartels, "On the optimality of the Wigner distribution for detection," *Proc. IEEE Int. Conf. Acoust. Speech Signal Process.*, vol. 3, pp. 1017–1020, Mar. 1985.

[88] Haldun M. Ozaktas, M. Alper Kutay, and David Mendlovic, *Introduction to the fractional Fourier transform and its applications*, vol. 106, pp. 239–291, Academic Press, San Diego, California, 1999.

[89] M. K. Brown and L. R. Rabiner, "An adaptive, ordered, graph search technique for dynamic time warping for isolated word recognition," *IEEE Trans. Acoust., Speech, and Signal Process.*, vol. ASSP–30, pp. 535–544, 1982.

[90] N. Meda, "Transversal filters with nonuniform tap spacing," *IEEE Trans. Circuits and Syst.*, vol. CAS–27, pp. 1–11, 1980.

[91] D. Wulich, E. I. Plotkin, and M. N. S. Swamy, "Synthesis of discrete time–varying null filters for frequency–varying singals using the time–warping technique," *IEEE Trans. Circuits and Syst.*, vol. 37, no. 8, pp. 977–990, Aug. 1990.

[92] M. Coates and W. Fitzgerald, "Time–frequency signal decomposition using energy mixture models," *Proc. IEEE Int. Conf. Acoust. Speech Signal Process.*, vol. II, pp. 633–636, June 2000.

[93] Ahmet Kemal Özdemir, Zafer Aydın, and Orhan Arıkan, "A new approach to time–frequency localized signal design," *Proc. IEEE Int. Conf. Acoust. Speech Signal Process.*, vol. II, pp. 1229–1232, May 2002.

[94] H. K. Kwok and D. L. Jones, "Improved instantaneous frequency estimation using an adaptive short–time Fourier transform," *IEEE Trans. Signal Process.*, vol. 48, pp. 2964–2972, Oct. 2000.

[95] L. Durak and O. Arıkan, "Short–time Fourier transform: two fundamental properties and an optimal implementation," *IEEE Trans. Signal Process.*, vol. 51, no. 5, pp. 1231–1242, May 2003.

[96] B. Boashash and P. O'Shea, "Use of the cross Wigner-Ville distribution for estimation of instantaneous frequency," *IEEE Trans. Signal Process.*, vol. 41, pp. 1439–1445, Mar. 1993.

[97] R. Baraniuk, M. Coates, and P. Steeghs, "Hybrid linear/quadratic time–frequency attributes," *IEEE Trans. Signal Process.*, vol. 49, pp. 760–766, Apr. 2001.

[98] M. Unser, "Splines a perfect fit for signal and image processing," *IEEE Signal Processing Magazine*, vol. 16, no. 6, pp. 22–38, Nov. 1999.

[99] L. B. Almeida, "The fractional Fourier transform and time–frequency representations," *IEEE Trans. Signal Process.*, vol. 42, no. 11, pp. 3084–3091, Nov. 1994.

[100] M. F. Erden and H. M. Ozaktas, "Synthesis of general linear systems with repeated filtering in consecutive fractional Fourier domains," *J. Opt. Soc. Am. A*, vol. 15, no. 1647–1657, 1998.

[101] M. A. Kutay, M. F. Erden, H. M. Ozaktas, Orhan Arıkan, Ö. Güleryüz, and Ç. Candan, "Space–bandwidth–efficient realizations of linear systems," *Optics letters*, vol. 23, pp. 1069–1071, 1998.

Vita

Ahmet Kemal Özdemir was born in Ankara, Turkey, on March 23, 1974. He received his B.Sc. and M.S. degrees from the Department of Electrical and Electronics Engineering at Bilkent University, Ankara, Turkey in 1996 and 1998, respectively. He then pursued his Ph.D studies at the Department of Electrical and Electronics Engineering, Bilkent University.

His research interests include digital signal processing and its applications to time–frequency analysis, radar signal processing, communications and array signal processing.